Imperfect Buckling of Pressurized Launch Vehicle Propellant Tank Segments

Reliability Study

Marcel Kwapien

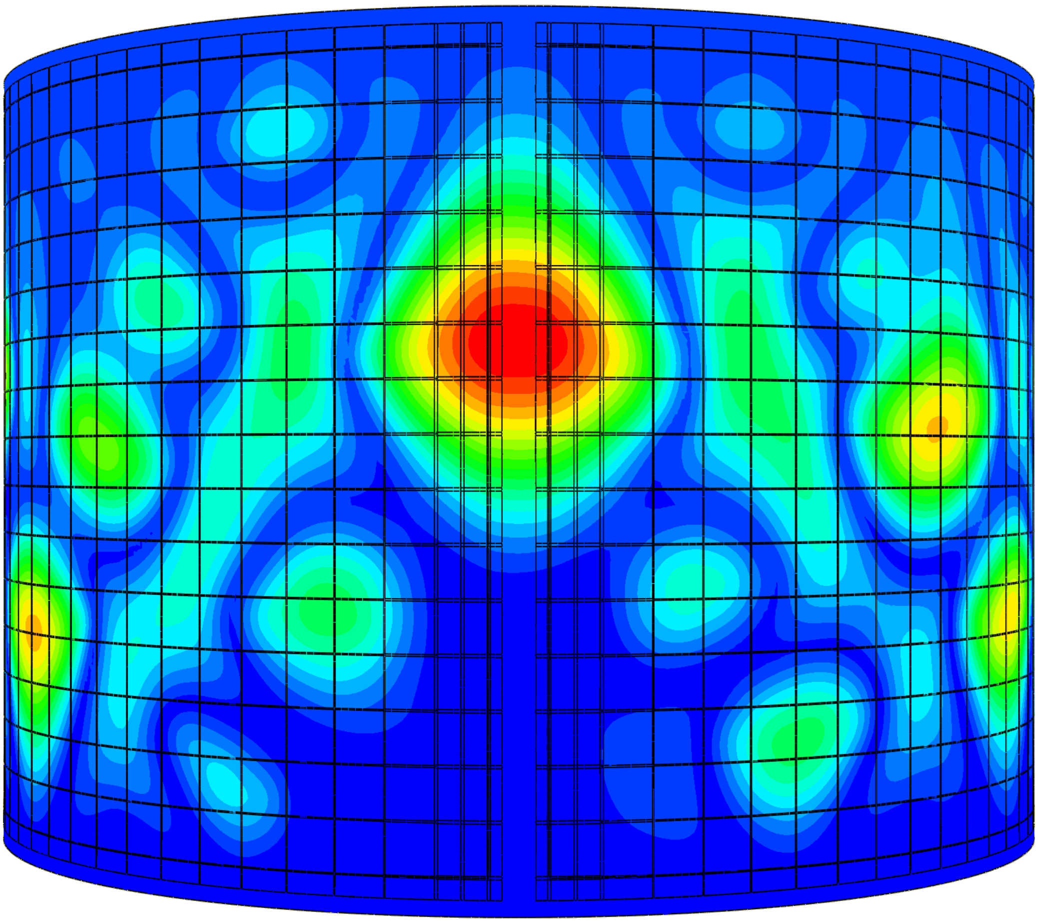

TU Delft

Imperfect Buckling of Pressurized Launch Vehicle Propellant Tank Segments

Reliability Study

by

Marcel Kwapien

to obtain the degree of Master of Science
at the Delft University of Technology,
to be defended publicly on Monday, January 19, 2026 at 14:00.

Student number:	5063744	
Project duration:	March, 2025 – January, 2026	
Supervisors:	Dr. ir. Saullo G.P. Castro	TU Delft
	Ir. Dominique Deloison	ArianeGroup
Thesis Committee:	Dr. Jian Guo	TU Delft
	Dr. ir. Otto Bergsma	TU Delft

*Cover: Postbuckling mode of NASA's TA*01 *shell.*

Preface

This work marks the end of my chapter at TU Delft. My six years at the university were full of ups and downs, yet rich in experiences throughout. If someone had told me at the beginning of this journey in 2019 that I would live through a global pandemic, work on multiple rocket projects, collaborate with ArianeGroup and Airbus, participate in the ESA Academy, and meet engineers shaping the European space industry, I would not have believed them. And yet, here I am.

This thesis is the culmination of what I have been passionately doing for the past four years, a journey that began at Delft Aerospace Rocket Engineering with the design of rocket structures. What initially started as a side activity gradually became my greatest motivation and passion. I would like to thank everyone at DARE with whom I had the pleasure to work with and learn from. Without that experience, this thesis would never have been written.

I would like to sincerely thank my supervisor, Saullo Castro, for agreeing to supervise this thesis despite the initial difficulties and for his continuous support, motivation, and guidance throughout its duration. It was a pleasure to work with you and learn from you.

I am also grateful to Dominique Deloison from ArianeGroup, who advised me on this topic and provided invaluable technical insight into launcher structural design. His extensive industry background made this thesis far more relevant to real-world challenges than I could have achieved otherwise. Every meeting with him offered more than any article or report I could have read.

Finally, I would like to thank my family and friends for their constant support and encouragement. My parents, for enabling me to pursue this dream, my girlfriend, for believing in me when I struggled to believe in myself, and my friends, for always making me laugh—especially when I was feeling down. Without all of you, this journey would not have been possible.

Marcel Kwapien
Delft, January 2026

Summary

Growing competitiveness in the launch market will intensify the pressure to optimize structural efficiency. Large thin-walled components—most notably metallic propellant tanks—will need to be pushed toward their feasible mass limits without compromising performance. These cylinders are inherently imperfection-sensitive, and their buckling behavior under combined axial loading and internal pressurization remains difficult to predict with confidence. Current design practices still rely on empirical knockdown factors derived from unpressurized tests or legacy structures, resulting in overly conservative margins. This work, therefore, investigates viable alternatives based on modern nonlinear imperfection-modeling approaches applied to pressurized metallic launcher tank segments.

Weld-induced geometric imperfections are known to dominate the behavior of metallic shells, forming a characteristic long half-waves at the weld land — the so-called imperfection signature. The literature shows that existing modeling strategies fall into two categories: (i) approaches that attempt to replicate this manufacturing signature by perturbing the geometry (measured or synthetic), and (ii) non-traditional methods that induce collapse through controlled boundary or loading imperfections. From this landscape, five representative strategies were selected and evaluated on a set of structures adopted from NASA's Shell Buckling Knockdown Factor Project: the 8-ft shells TA01, TA03, TA07, TA09, and the 27.5-ft external tank article ETTA1, analyzed at 3 loading cases of 0, 2, and 4 bar.

The methods considered include single and multiple perturbation approaches (SPLA/MPLA), the eigenmode imperfection approach (EIA), measured (radial) geometrical imperfections (MGI), and a newly introduced distributed force perturbation approach (DFPA) that locally amplifies the load to trigger collapse. Given the absence of validated high-pressure test data, this study focused on assessing the behavior of these approaches under different structure–pressure interactions and quantifying their reliability. Three statistical metrics were used: the coefficient of variation (relative variability), Kendall's W (agreement in ranking), and the intraclass correlation coefficient (relative reliability).

The results showed that internal pressurization alters the buckling behavior of stiffened metallic shells, with the extent varying with their design and imperfection strategy. In principle, it suppressed imperfection sensitivity by increasing the geometric stiffness through longitudinal and hoop stabilization and progressively shifting the response toward a pressure-dominated regime. Methods based on distributed or multiple perturbations (DFPA, MPLA) demonstrated the highest reliability across pressures, but resulting in conservative buckling load estimates. Approaches relying on localized, geometry-driven, or manufactured imperfections (SPLA, MSI, EIA) were considerably more pressure-sensitive. They exhibited poor consistency as the imposed shapes became subordinate to the stabilizing hoop and axial stresses. At higher pressures, the buckling modes of nearly all approaches started converging, indicating an upper bound on the stabilizing effect of internal pressure.

This study demonstrates that reliable prediction of pressurized buckling cannot be achieved by simply reproducing geometric imperfections or relying on stiffness-dependent modes. The consistency of a modeling approach depends on how its imperfection mechanism interacts with pressure-induced stiffening and the structure's geometry. Methods strongly tied to shell stiffness or to manufacturing-driven imperfections lose reliability as pressure increases, since their influence becomes highly configuration-dependent and is progressively suppressed. Signature-based approaches show mixed behavior depending on the magnitude of the induced imperfection and the degree of resemblance to the signature imperfection. Methods that do not rely on traditional imperfections (DFPA) benefit least from pressure stiffening and therefore provide the most stable predictions across pressure levels, albeit remaining conservative. Collectively, the results highlight that accurate modeling in the pressurized regime requires approaches whose imperfection mechanism remains stable under pressure and does not depend on structural details that become irrelevant as imperfection sensitivity diminishes. The results underscore the need for pressure-aware design strategies that go beyond traditional knockdown factors to achieve higher performance.

Contents

List of Figures

List of Tables

1

Introduction

The increasing demand for launch services - driven primarily by mega constellation-deployment has led to rapid growth of the global launch market. Today, approximately 150 launch systems are operational or under development [5], creating intense competition. To remain competitive, new launch vehicles must deliver high performance at reduced cost, driving designers to minimize structural mass wherever possible. Achieving such performance places significant demands on the vehicle's primary load-bearing structures—particularly the propellant tanks. These large, cylindrical, thin-walled and pressurized structures, which account for the majority of the structural weight, were found to be problematic in design.

Thin-walled circular cylinders are one of the fundamental geometrical shapes utilized for launch vehicle structures [50, 88], including tanks and interstages, as visible in Figure 1.1. Their favorable stiffness-to-weight ratio makes them ideal for axial load transfer [40]. However, this simultaneously positions them as stability-critical structures [32], with the buckling load being an essential consideration in their design [50].

In addition to stability-related issues, these structures are often exposed to extreme temperature gradients due to the storage of cryogenic propellants, such as liquid oxygen (LOx) at $-182°\mathrm{C}$ or liquid hydrogen (LH_2) at $-252°\mathrm{C}$ [23]. Temperature effects not only induce significant thermal stresses in the vessel walls, but also strongly affect the material properties [46]. Consequently, designers face a highly complex thermomechanical problem when assessing the structural integrity of launch vehicle tanks.

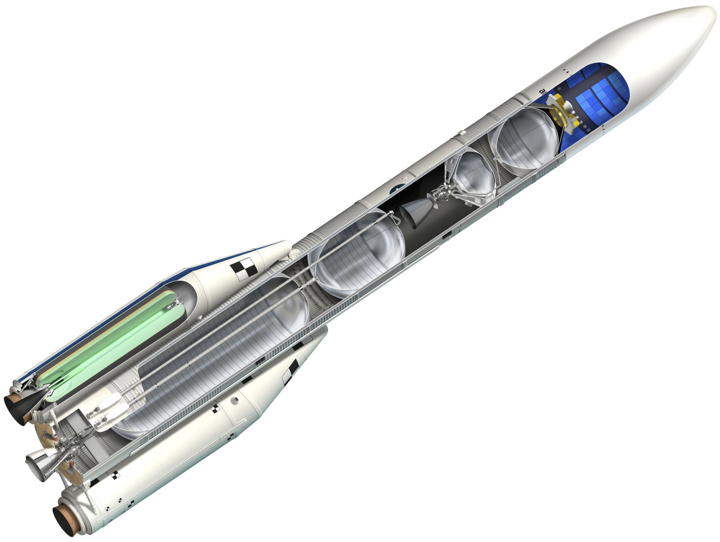

Figure 1.1: Ariane 62 structure overview [22].

Over the past decades, extensive efforts have been made to predict the collapse behavior of thin-walled cylinders and to match simulations with experimental results. The discrepancy between analysis and testing was attributed to geometric imperfections, which cause the shells to deviate from the theoretical behavior. To account for this effect, empirically derived knockdown factors (KDFs) were proposed [86]. However, these factors, today, are widely recognized as overly conservative, not reflecting modern manufacturing quality [88], and leading to suboptimal designs [41].

NASA's Shell Buckling Knockdown Factor (SBKF) Project addressed this shortcoming by testing state-of-the-art metallic cylinders and establishing a new generation of KDFs. These updated factors yielded 5–8% structural mass savings on the SLS Core Stage tanks and reduced material and machining costs by roughly $400k per tank, with an estimated return on investment of $5.45M per launch [36].

Yet one critical aspect remains largely unexplored - internal pressurization, necessary to provide sufficient propellant flow and operating conditions for the pumps. Only a single test article - the Space Shuttle External Tank- has ever been tested under pressure, and its collapse load significantly exceeded the analytical predictions, highlighting a major gap in current design tools. Without pressurized KDFs, engineers must rely on high-fidelity nonlinear analyses to more accurately estimate buckling performance.

While it has long been recognized that internal pressure increases shell stiffness and mitigates imperfection sensitivity, the combined effect of pressure and modern imperfection-modeling strategies across different metallic configurations is still poorly understood. The literature shows that welded aluminum tank segments exhibit characteristic imperfection signatures driven by manufacturing processes. Existing numerical approaches either attempt to reproduce these signatures or rely on artificial boundary or load imperfections to trigger collapse. The extent to which these imperfection fields must be represented under operational pressure is still unclear. This study investigates this gap by examining how representative each modeling strategy remains once the shell is internally pressurized and whether these imperfections continue to govern the collapse behavior.

In this work, several state-of-the-art imperfection modeling approaches were examined and summarized in Chapter 2, along with representative launcher-tank shell configurations. This review led to the formulation of the main research question and hypothesis, followed by the identification of the relevant test articles' geometry.

The adaptation of these approaches to pressurized buckling analysis, along with the shell modeling strategy and finite element setup, is detailed in Chapter 3. As no pressurized test data exist for these configurations, the shell models and analysis procedures were thoroughly verified against available unpressurized experiments and past numerical studies. The full verification workflow and the associated sensitivity checks are detailed in Chapter 4.

The resulting buckling predictions and reliability assessment are presented in Chapter 5, where the findings are interpreted in the context of imperfection signature behavior. Finally, key observations, answers to the research question, and recommended directions for future work are summarized in Chapter 6.

2

Literature Review

In this chapter, the relevant shell buckling literature is reviewed and presented in the context of launch-vehicle segments. First, a general overview of buckling behavior is provided together with currently employed analysis methods, with emphasis on imperfection modeling approaches. The chapter then outlines the design of launch-vehicle propellant tanks and identifies the primary sources of geometric imperfections. Subsequently, notable studies on the buckling of launch-vehicle structures are discussed, concluding with an overview of pressurized shell buckling behavior.

The review is followed by a dedicated discussion in which the identified limitations of existing approaches are synthesized to expose a clear research gap. Based on this assessment, the research questions are formulated together with the accompanying main hypothesis.

2.1. Buckling of Thin-Walled Cylinders

Numerous studies have been conducted in the past, trying to accurately predict the collapse load of thin-walled cylinders and align them with experimental data. The large discrepancy between the test results and the predictions was associated with different forms of cylinder imperfections, causing the shell to deviate from the perfect structure behavior [3, 39, 51].

The deviations from the ideal circular shape, or thickness variations, are known as geometric imperfections or traditional imperfections. They are embedded in the structure and result from manufacturing processes [39]. Through testing and further research, additional imperfection sources have been identified and linked to the testing setup. Known as non-traditional imperfections, they are affiliated with variations in boundary conditions and/or nonuniform end-loading during the test [53].

The most commonly used classification of imperfections was proposed by Winterstetter and Schmidt [101]. The authors differentiated 3 basic types of geometric imperfections, each with distinct effects on the shell's behavior. The 'realistic' imperfections are those measured from the build geometry using contact or non-contact optical measurement techniques [98]. These deviations degrade the structure's behavior to the as-built one. Second in the classification are the 'worst' imperfections, which are mathematically defined as "the worst possible imperfection pattern" [101]. Several authors concluded that they are conservative, as the pattern degrades structural performance to an extent rarely observed in reality. Lastly, Winterstetter and Schmidt [101] differentiated 'stimulating' geometric imperfections. This group refers to imperfections generating equivalent patterns to 'realistic' imperfections a priori to the structure's fabrication. The effect of these on the shell's behavior is uncertain, as it depends on the predicted pattern and its resemblance to manufactured imperfections, and/or its effect on the buckling pattern.

It is worth noting that the concept of non-traditional imperfections was introduced after the classification release. Hence, despite using the geometrically accurate 'realistic' measured imperfections, the discrepancy between the experimental results and simulations might persist [41, 98]. Altough today there are methods capable of considering both geometric and loading imperfections [88].

2.2. Knockdown Factor Approach

Initially, to align the test data with the results from linear bifurcation analysis, particularly for the design of launcher structures [3], empirical knockdown factors (KDFs) have been introduced [41]. It is defined by Equation 2.1, where N_{cr} is the predicted buckling load from an experimentally-validated, high-fidelity finite-element model representing the buckling load for a geometrically imperfect structure, and N_{cl} represents the linear buckling load [37].

$$\text{KDF} = \frac{N_{cr}}{N_{cl}} \tag{2.1}$$

These factors (statically lower-bound curves [89]) were derived from a series of shell-buckling experiments conducted on isotropic metallic shells between the 1920s and 1960s and compiled into a comprehensive guideline known as NASA SP-8007 [86]. However, these design guidelines have not been updated since, and did not take advantage of modern materials, precision manufacturing, and current structural concepts [37, 43], leading to ultraconservative designs [41] and resulting in increased structural mass for short and large diameter launch vehicle shells [94].

To address this issue, NASA started the Shell Buckling Knockdown Factor (SBKF) project, aiming to derive analysis-based KDFs together with new design recommendations for selected metallic and composite launcher cylindrical segments [37]. During the project, several integrally stiffened metallic cylinders were subjected to compression testing, including eight subscale 8 ft-diameter articles and two full-scale 27.5 ft-diameter cylinders based on the Space Shuttle external tank.

Based on the buckling results, a new series of KDFs for metallic orthogrid-stiffened shells was proposed [37]. These factors were differentiated into manufacturing classes: Class 1 for current-state-of-the-art production, Class 3 for legacy manufacturing, and Class 2 for intermediate quality. However, the knockdowns are valid only for shells with a slenderness ratio $R/L < 2$. Although the proposed KDFs set includes factors for pressurized cylinders, it does not cover the full range of operational pressures, nor does it clearly specify the imperfection-modeling strategies used during the derivation of the corresponding collapse loads [57].

2.3. Measured Geometric Imperfections Approach - MGI

Realistic imperfections can be introduced in the form of measured geometric imperfections (MGI), typically captured with respect to the shell's top or mid-surface - referred to as Mid-Surface Imperfections (MSI) [11]. After measurement, the data is implemented into finite element analysis by mapping the imperfections onto the finite element mesh [17], after which a nonlinear buckling analysis is conducted.

Many authors have studied this method and have reported accurate results when compared with experimental buckling results. However, its reliability varies significantly depending on the shell type and imperfection shape, as discussed later in the report. As noted by Haynie and Hilburger [31], such imperfections are typically not known a priori during the design and fabrication stages. As a result, engineers are often required to resort to alternative prediction methods—particularly analysis-based lower-bound approaches to ensure conservative design. Several 'stimulating' imperfection approaches have therefore been developed and investigated, aiming to approximate the buckling response without relying on direct measurements.

2.4. Eigenmode Approach - EIA

One of the most commonly used imperfection modeling techniques is the linear buckling mode-shaped imperfection approach [11], which introduces one or more eigenmodes from a linear buckling analysis (LBA) into an initially perfect shell model. Due to its simplicity, it remains widely used in the industry to estimate lower-bound buckling loads [11, 33, 89].

Several design standards incorporate this approach. NASA SP-8007 recommends the Eigenmode Imperfection Approach (EIA) for imperfection sensitivity studies when measured data is unavailable [86]. It suggests combining multiple modes, with amplitudes scaled to a root-mean-square value equal to half the shell thickness. Similarly, Eurocode 3, which applies to steel shell structures, advises using eigenmodes to define imperfection shapes, with amplitudes dependent on manufacturing quality [1].

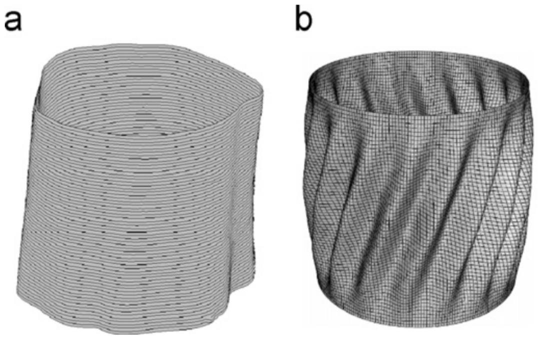

Figure 2.1: Comparison of measured imperfections (a) and eigenmode (b) of a cylinder [91].

Despite its practical appeal, EIA is not without drawbacks. The eigenmode-shaped imperfections used in this approach are not typically observed in real as-built structures - as showcased in Figure 2.1, and the selection of modes is often arbitrary. Furthermore, the significant membrane stiffness degradation caused by these imperfection shapes is rarely observed in experimental tests [33].

Orifici and Bisagni [66] pointed out that eigenmode-based imperfections can lead to nonphysical behavior due to excessive stiffness reduction. They recommended limiting imperfection amplitudes to no more than 0.5 times the shell thickness to avoid unrealistic responses.

Comparative studies highlight both the potential and the variability of EIA predictions. Castro et al. [11] demonstrated that circumferential eigenmodes reduce membrane stiffness more than axial ones, leading to higher knockdown factors, while axial modes can slightly improve buckling resistance. The study concluded that EIA can predict lower-bound collapse loads, but the results depend heavily on the selected mode and amplitude. Similarly, Arbocz and Williams [4] showed that both the combination and amplitude of modes are critical. Their multi-mode EIA analysis revealed convergence of predicted knockdowns toward experimental data as more modes were included, though with a consistent trend of decreasing collapse load as additional modes were added.

Li et al. [55] found that for curved panels with cutouts, the first eigenmode could closely match measured imperfection fields, although the accuracy was dependent on cutout size. In some cases, EIA was even shown to be more conservative than the empirical NASA SP-8007 knockdowns [99].

A persistent challenge is that compression-loaded circular cylinders often exhibit clustered eigenvalues, making it unclear which eigenmode should serve as the imperfection basis [70]. Sosa et al. [78] concluded that the critical load generally corresponds to the first eigenmode, and Speicher and Saal [79] recommended using it, with amplitude tied to manufacturing tolerances. However, this is not always valid — other studies have shown that the first mode is not necessarily the most detrimental or representative of as-built imperfections [31, 41].

2.5. Perturbation Induced Imperfection Approaches

Single Perturbation Load Approach - SPLA

The idea that a single dimple can represent the most detrimental imperfection originates from the work of Horák et al. [44] and Deml and Wunderlich [19], who showed that the worst-case imperfection shape differs significantly from classical eigenmodes and is often localized. This was further supported by experimental observations from Esslinger [25], who recorded single-buckle patterns initiating the buckling process. As such, a single-dimple imperfection can be considered realistic, stimulating, and conservative [47].

Hühne et al. [47] proposed the Single Perturbation Load Approach (SPLA) for unstiffened composite shells. It involves introducing a local dimple at the mid-height of a perfect shell using a transverse perturbation load applied before the main axial compression [55]. As the magnitude of the perturbation load increases, the buckling load drops until a threshold is reached, as shown in Figure 2.2, beyond which further increases in the perturbation have minimal effect [91]. This threshold is linked to local snap-through behavior, as confirmed by Castro et al. [10]. However, slight radial inward shifts beyond this point (caused by higher perturbation force) may still reduce the buckling load slightly, resulting in a decreased buckling load.

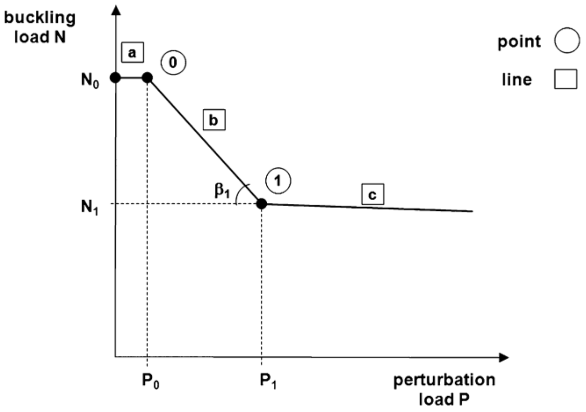

Figure 2.2: Idealized SPLA buckling convergence curve [47].

SPLA typically yields lower-bound estimates of buckling loads that are less conservative than those from NASA SP-8007, but still capture critical behavior [47]. For the same imperfection amplitude, SPLA showed higher knockdown factors (KDFs) compared to EIA and axisymmetric imperfections in the comparative study by Castro et al. [11]. The SPLA approach was thoroughly studied under the DESICOS project (Design Guidelines for Imperfection Sensitive Composite Launcher Structures) [27], which concluded that the original SPLA cannot always guarantee a lower-bound buckling load [93].

Several limitations and sensitivities have been reported. For metallic orthogrid-stiffened shells, Hao et al. [30] showed that the location and magnitude of the perturbation load strongly affect the collapse load. Conversely, Arbelo et al. [2] found that angular position has little influence on composite shells. Moreover, Wang et al. [98] highlighted the feasibility constraint on perturbation amplitude for launch vehicle structures, arguing that exceeding this threshold results in non-representative geometries and overestimates collapse loads by up to 27.8

SPLA Variants

Due to SPLA's load-controlled nature, it cannot reach metastable equilibrium points typical of real shell behavior. To overcome this, the Single Perturbation Displacement Approach (SPDA) was introduced. It introduces the dimple using displacement control, allowing the structure to settle into a metastable configuration more representative of as-built imperfections [90, 91].

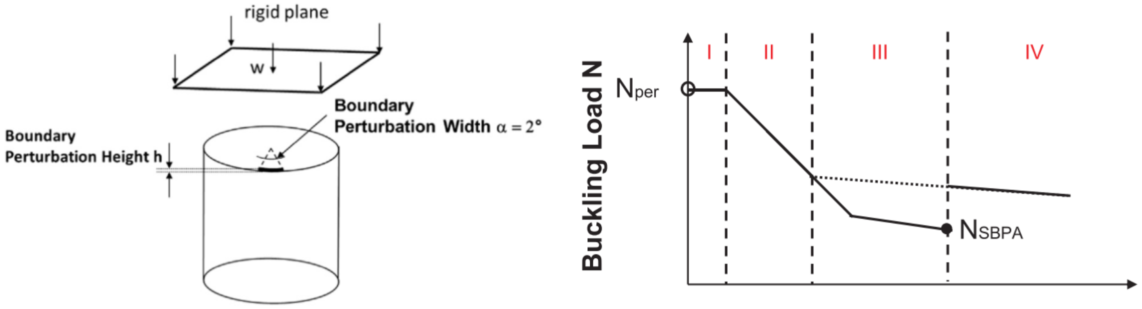

Figure 2.3: Overview of the SBPA method and its buckling convergence behavior [93].

Another evolution is the Single Boundary Perturbation Approach (SBPA), which combines geometric and load introduction effects. It induces a dimple (via a shim or equivalent) at the load introduction edge, which travels downward during compression [91, 92]. The overview of the method is shown in Figure 2.3. The angular width of the dimple is typically 2° for slender shells ($R/t > 200$) and 4° for thicker ones, based on convergence studies [93]. The height of the shim acts as a free variable, effectively serving as a perturbation load.

Degenhardt et al. [18] proposed integrating SPLA with stochastic modeling to account for both traditional and non-traditional imperfections, such as thickness variations, which Hilburger and Starnes [39] identified as especially relevant for composite structures.

Multiple Perturbation Load Approach (MPLA)

To capture more complex imperfection patterns, Arbelo et al. [2] extended SPLA into the Multiple Perturbation Load Approach (MPLA). Here, multiple dimples are introduced via perturbation loads at predefined locations and magnitudes to simulate worst-case imperfections. While more conservative than SPLA, it yields collapse loads closer to those predicted by NASA SP-8007. It also introduced complexity regarding optimal selection of dimple number, location, and intensity.

A further development was the Worst Multiple Perturbation Load Approach (WMPLA) proposed by Wang et al. [97]. This approach uses a surrogate-based optimization framework to determine the most detrimental combination of dimple positions and magnitudes, minimizing collapse load through iterative simulations [84, 98].

While WMPLA can provide highly accurate collapse predictions for isogrid metallic cylinders, it suffers from high computational cost, involving hundreds of finite element simulations [99]. Like SPLA, its accuracy depends on the perturbation load magnitude - too low a magnitude can lead to an overestimation of the buckling load [98].

Cutout Approach

Many launch vehicle structures include cutouts that serve as access points or assembly doors. Under compressive loading, these cutouts can initiate local buckling at loads lower than the general instability load of a perfect shell [40].

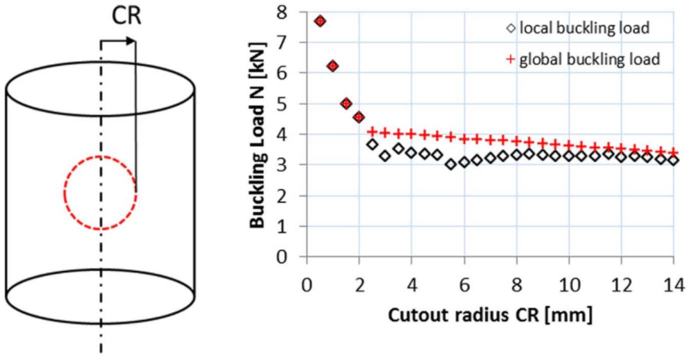

Figure 2.4: Cutout buckling convergence plot [93].

Wagner et al. [93] proposed using cutouts to induce imperfections by introducing a small circular cutout at the center of the shell and increasing its size until a diamond-shaped buckling pattern emerges. The authors demonstrated that even a small 2 mm cutout can reduce the global collapse load of a composite shell by 40%. In their analysis, the collapse load reached a lower-bound value at a cutout-to-radius ratio of 0.25. The knock-down factor obtained for the composite shell was similar to those predicted by WMPLA and SBPA. However, for stiffened metallic shells, the approach tended to overestimate the buckling load compared to the SBPA-derived lower bound. The authors concluded that the cutout approach is the fastest and most accurate imperfection strategy for cylindrical shells, although further investigation is necessary. Notably, the method may not be suitable for short and thick shells, as also observed by Miladi and Razzaghi [61].

Nevertheless, past studies summarized in [87] suggest that for cylinders with small unreinforced cutouts, the effect on buckling response is minimal, with other geometric imperfections often being the dominant factor.

2.6. Imperfection Signature of Metallic Tank Segments

Arbocz and Starnes Jr [3] were the first to propose that each shell manufacturing process can be associated with a unique imperfection pattern, also referred to as an imperfection signature. Based on observations from composite shell tests, the authors concluded that shells fabricated using the same method contained shell-wall ply gaps, resulting in characteristic geometric imperfections that were equally detrimental to buckling performance. The idea was further developed by Hilburger et al. [41], who argued that imperfection signatures from previous designs could serve as an early-stage tool for estimating the buckling load of as-built shells.

In contrast to the view presented by Arbocz and Starnes Jr [3] and Hilburger et al. [41], Wagner and Hühne [88] suggested that cylindrical shells, regardless of fabrication method, exhibit a common diamond-shaped buckling mode. This lower-bound worst-case mode becomes dominant if the imperfections are sufficiently large in both magnitude and shape. It was identified using SBPA on an isogrid-stiffened aluminum shell, without prior knowledge of the actual manufacturing imperfections. Although the predicted knockdown was less conservative than the SP-8007 value, this method, like other lower-bound approaches, does not reward high-quality manufacturing.

Tank Design Impact on Imperfections

Historically, several authors have studied the buckling behavior of metallic launch vehicle structures. Most work has focused on integrally stiffened aluminum cylinders, which offer improved knockdown factors [93] and reduced imperfection sensitivity compared to monocoque designs [45]. These segments are also cheaper and faster to produce, can be easily tailored to specific loading conditions, and achieve lower structural mass compared to riveted or fastened counterparts [65, 82]. Conventionally, internal stiffeners are favored over external ones, despite the latter offering higher buckling resistance [82].

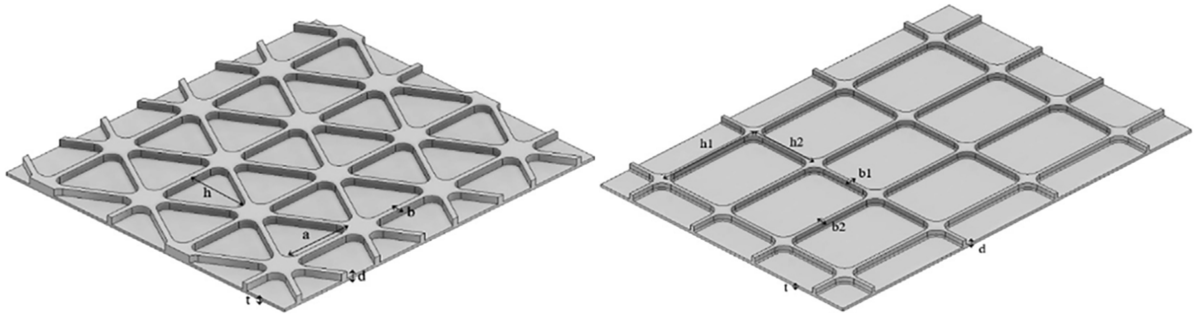

(a) Isogrid milled plate.

(b) Orthogrid milled plate.

Figure 2.5: Grid stiffened configurations [63].

Stiffeners are typically arranged in grid patterns (Figure 2.5) — either orthogrid, spanning axial and circumferential directions to form rectangular bays, or isogrid, with helically intersecting ribs forming equilateral triangles [21, 49, 82]. The shells are manufactured from machined plate segments, which are rolled and longitudinally welded to form barrel sections [30] - the overview of the manufacturing steps is presented in Figure 2.6. These barrels are then vertically stacked and circumstantially welded to create the final LV structure [64]. Thornburgh and Hilburger [82] classified such structures as segmented shells with weld land discontinuities rather than continuously stiffened shells. The number and height of the segments are typically limited by available plate stock size [82].

Panel edges are thickened to compensate for the strength loss introduced by the welding process [46]. These regions are referred to as weld lands [82]. A weld land is accompanied by the transition section. The weld-section thickness is dictated by the strength required to withstand internal pressure. In contrast, the transition thickness is selected to reduce local stress concentrations between the weld and the acreage skin [82].

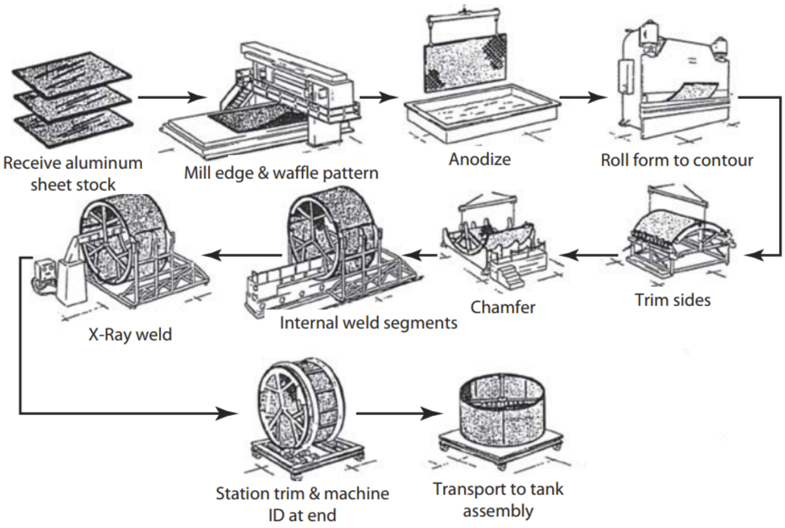

Figure 2.6: Barrel panel manufacturing overview for Saturn IV [23]

The panel grid pattern can transition into the weld land in two principal ways: by gradually tapering the stiffeners down into the transition region (tapered stiffener transition), or by terminating the orthogrid at an axial stiffener adjacent to the weld land (picture-frame design). The detailed geometry of both configurations is shown in Figure 2.7.

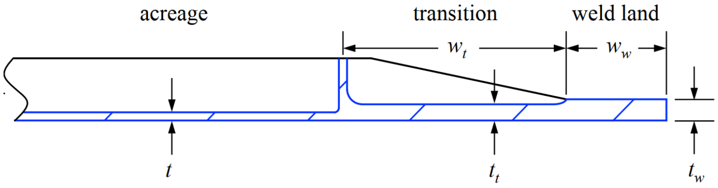

(a) Tapered stiffener transition geometry .

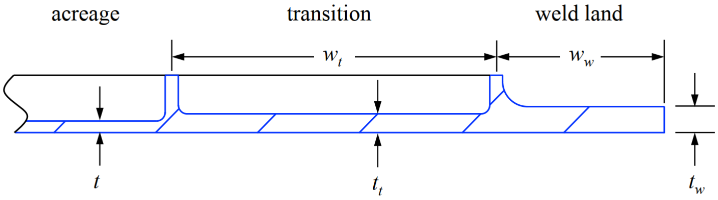

(b) Picture frame stiffener transition geometry.

Figure 2.7: Stiffener transition designs at weld lands adopted by NASA [37].

Early work by Arbocz and Williams [4] and Nemeth et al. [64] demonstrated that welded barrel segments exhibit significant imperfections near the welds, severely reducing buckling strength. A characteristic pattern was identified near the weld land, consisting of one axial half-wave and multiple circumferential full waves, with maximum inward deflection at the weld seam as visible in Figure 2.8. These imperfections were found across various welding techniques and were common in large-scale, liquid-propelled launch vehicle structures [64].

Thornburgh and Hilburger [82] studied the effect of longitudinal weld lands on the buckling of stiffened cylinders. It was shown that the weld lands possess higher in-plane stiffness due to their increased thickness but reduced bending stiffness. As a result, they attracted more load while being less able to resist inward deformations. Using a smeared-stiffness approach (where the structure's grid is represented with increased skin thickness as explained in Appendix B), this effect was found to be less severe for shells with thicker skins, where the thickness difference is smaller. Conversely, shells with taller stiffeners experienced amplified effects due to larger circumferential bending discrepancies. Axially stiffened shells were less affected by weld lands than hoop-stiffened ones. For the original (non-smeared) geometry, the collapse load reduction was even more pronounced. The authors recommended altering the stiffener layout—bringing stiffeners closer to the weld land or adding an extra pair—to locally increase bending stiffness and reduce inward deformation.

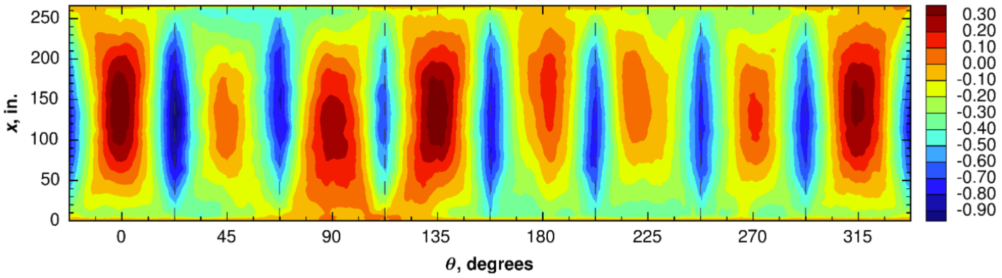

Figure 2.8: Imperfection signature of a metallic cylinder with eight longitudinal weld lands [37].

For the SKBF study, Hilburger et al. [35] built, tested, and analyzed three stiffened metallic shells with differing buckling behaviors: two sub-scale (8-ft diameter) and one full-scale (27.5-ft diameter) to validate that sub-scale results translated to full-scale hardware. The first specimen, TA01, was a lightly stiffened, integrally machined shell with an R/t ratio corresponding to lightly loaded upper-stage rocket segments. It was designed to fail in global buckling, and additional longitudinal stiffeners were placed along the axial welds to prevent weld buckling.

The second specimen was a scaled-down version of the Ares I liquid hydrogen tank barrel section, featuring a denser orthogrid pattern [93]. It was expected to experience weld land buckling first. The full-scale structure relied on internal pressure to provide axial relief and hoop stabilization, precluding other failure modes. Because the sub-scale model was not pressurized, the stiffener layout was modified to delay skin buckling in favor of global buckling. The full-scale test article, ETTA1, was a segment from the Space Shuttle's external liquid hydrogen tank. It was expected to undergo both skin-pocket and weld land buckling.

Both sub-scale specimens consisted of three 120° longitudinally welded segments. The full-scale ETTA1 structure was constructed from eight identical segments joined by longitudinal friction stir welds. Post-manufacturing, geometric imperfections were measured.

For TA01, the imperfection pattern did not exhibit the typical axial half-wave associated with welding (Figure 3.7). Instead, multiple low-amplitude, short-wavelength, delocalized imperfections occurred. No correlation between the weld lands and imperfection pattern was found [42]. This was attributed to the added longitudinal stiffeners adjacent to the welds, which reduced local buckling tendencies [93]. TA03 did show axial half-wave distortions at the welds, although one weld had much larger distortions than the others. The full-scale ETTA1 exhibited significant geometric variation near the weld lands, with eight distinct axial half-waves observed [35].

During the ETTA1 test, knockdown due to weld imperfections was so severe that it prevented achieving test objectives. Instead of proceeding through local skin buckling, weld land buckling, and finally global buckling, the structure entered a benign buckling mode prematurely. To proceed, it had to be pressurized to 1 psi (0.06895 bar) to bulge out the imperfections and "push the weld land back into circular geometry" [38].

In another SKBF study, a seamless cylinder was tested to demonstrate the benefit of eliminating weld lands [69]. A flow-formed, integrally machined orthogrid cylinder (Seamless Test Article - STA8.1) was compared with a three-segment welded counterpart (TA09). The latter exhibited typical axial half-wave imperfections due to weld shrinkage. In contrast, STA8.1 showed no localized inward deformations, and its overall imperfections were smaller. Nonlinear geometric buckling analysis showed that STA8.1 had a 28% higher collapse load than TA09. Further analysis revealed that in TA09, weld lands contributed more to the knockdown than the measured imperfections. A model of TA09 with only the weld land geometry (no imperfections) had a 21% lower collapse load than a model with just imperfections. Comparisons of only the geometrically imperfect shells showed a 3% load reduction for STA8.1 and 12% for TA09 compared to the perfect case.

In the study by Wang et al. [98], measured imperfections in an isogrid-stiffened shell composed of four welded aluminum segments did not show the typical axial half-wave pattern at the welds. Instead of tapering the stiffeners near welds, the panels were welded along adjacent stiffeners. The radial imperfection map did not clearly indicate the weld land location, nor could distortions be correlated to geometric features. The authors did not perform imperfection signature analysis, nor did they provide details about the weld geometry or process.

Hao et al. [30] investigated both axial and circumferential welds using SPLA and WMPLA. Sequential and staggered barrel configurations were examined. It was concluded that circumferential welds slightly reduced imperfection sensitivity, and staggered axial welds, while offering higher imperfection tolerance, resulted in lower collapse loads compared to sequential alignment.

NASA's SKBF work identified welding signature and weld land geometry as features with significant influence on analysis-based knockdown factors [37].

2.7. Notable Works on Buckling of Stiffened Metallic Shells

Several studies have addressed the imperfection sensitivity and buckling behavior of stiffened metallic shells in the context of launch vehicle structures. This section outlines key contributions focusing on imperfection characterization, perturbation-based analysis methods, and experimental benchmarking.

Imperfection characterization and prediction accuracy

Arbocz and Williams [4] investigated an orthogrid-stiffened welded cylinder using a multi-mode eigenvalue approach to approximate measured initial imperfections. The geometric distortions were expressed using two double Fourier series, enabling detailed analysis of axial and circumferential wave components. The study concluded that accurate buckling predictions require not only appropriate mode selection but also precise amplitude representation based on Fourier coefficients. Therefore, understanding imperfection patterns specific to a fabrication process can aid in a more reliable design.

Perturbation Load Methods: SPLA, MPLA, WMPLA

The same shell geometry analyzed by Arbocz and Williams [4] was reused by Hao et al. [30], who evaluated its collapse load using SPLA, MPLA, and WMPLA techniques. The model included orthogrid stiffeners but excluded weld lands. An initial validation using explicit nonlinear dynamic analysis confirmed the buckling load range reported in the earlier test.

In the SPLA study, convergence was evaluated using four axial positions, ranging from mid-weld to acreage, at mid-cylinder length. Sensitivity to perturbation load magnitude and position was observed: low-magnitude perturbations placed near the acreage yielded the lowest collapse loads, whereas higher-magnitude perturbations showed critical sensitivity at weld land locations. To replicate the characteristic half-wave pattern, three localized loads were applied at each longitudinal weld land in the middle bay. The most severe perturbation reproduced the experimental lower-bound collapse load.

WMPLA was applied using a Multi-Island Genetic Algorithm (MIGA), yielding a conservative estimate of 2990 kN, below the tested lower limit of 3047 kN. A Monte Carlo extension of MPLA showed a wider buckling load range than the test data, underlining the variability introduced by stochastic perturbation distributions. Additional simulations on cylinders with sequential and staggered circumferential welds showed reduced imperfection sensitivity when welds were present.

Non-traditional Perturbation Methods: SBPA, EBC

Wagner et al. [94] compared experimentally and numerically obtained knockdowns for several SBKF shells—including ETTA1, TA01, TA03, and STA8.1 —as well as TA01 derivatives used for L/R and R/t parametric studies. The study compared knockdown factors (KDFs) derived from SBPA and Energy Barrier Concept (EBC) against empirically proposed values by Hilburger [37] and Sim et al. [75]. SBPA yielded more conservative estimates for global buckling, while EBC predicted higher KDFs and better matched test data. Two stiffener modeling strategies (detailed and smeared) were evaluated, with recommendations for further investigation of EBC's applicability to various shell types.

In [93], TA01 and TA03 shells were evaluated using SBPA, cutout approach, and a threshold KDF from [89]. While SBPA provided less conservative estimates than NASA SP-8007, none of the methods accurately reproduced the knockdown observed in the TA01 test, likely due to the high fidelity of the experimental setup. The cutout method predicted the highest knockdown values among the methods tested.

Imperfection Sensitivity in Isogrid Cylinders

Wang et al. [98] performed a comprehensive comparison of numerical and experimental imperfection sensitivity on an isogrid-stiffened shell representative of the Changzheng-5 launch vehicle [88]. Imperfection modeling techniques included eigenmodes, measured imperfections, SPLA, and WMPLA. Measured imperfections overestimated the buckling load, likely due to unmodeled effects such as material or loading imperfections. EIA produced conservative estimates in line with previous findings by Haynie and Hilburger [31]. NASA SP-8007 (pre-2020 SKBF revision) yielded lower bounds unsuitable for lightweight design.

SPLA with a single perturbation load overestimated buckling by 28%, indicating the inadequacy of this method in capturing full-field imperfections. In contrast, SPLA with stochastic perturbation loads reduced this error to 2%, though accuracy was shown to depend on the fidelity of the input probability density function. WMPLA produced mode shapes closely resembling test results due to multiple perturbation origins, though its sensitivity to perturbation magnitude and location introduced uncertainty (predictions ranged from -0.19% to over 30% error). Following Wang et al. [97], three perturbation loads were considered adequate, though future studies were recommended to investigate the number and size of dimple imperfections. Notably, the authors noted that “WMPLA cannot guarantee the consistency of buckling mode with test results by different manufacturing processes” and should only be used to estimate lower-bound collapse loads.

Parametric Studies and Modeling Simplifications

Kim et al. [50] extended the work of [98] by conducting a parametric study of R/t ratios on the same baseline isogrid shell, applying SPLA exclusively. The study used a displacement-controlled scheme (modified from [47], [74]) instead of axial compressive loads, combined with artificial damping to stabilize post-buckling behavior [100]. Perturbation magnitudes exceeded those in [98], though no analysis of induced imperfection amplitude was provided (see 2.5).

Two modeling strategies were compared: an equivalent model with smeared stiffeners and a detailed geometry model. Both produced similar buckling responses with relative error below 5%. For the baseline case, both models overestimated the experimental buckling load by 5%—an improvement over the 28% overprediction in [98]. The authors recommended equivalent models due to their accuracy and reduced computational cost.

2.8. Buckling of Pressurized Shells

In liquid-propellant rocket engines, ensuring a steady and reliable flow of propellants into the combustion chamber is essential for sustained thrust and stable operation. Propellant delivery can be achieved via two main feed systems: pressure-fed and turbopump-fed. In both cases, the propellant must enter the engine at a specified pressure to ensure proper combustion and avoid issues such as cavitation, flow separation, or pump damage. This is especially critical for turbopump systems, where sufficient inlet pressure is required to meet the pumps’ net positive suction head criteria. To meet these requirements, the propellant tanks themselves must be pressurized. Depending on the feed system, the pressure magnitude ranges from 30-100 psia (2.06 - 6.89 bar) for a turbopump-fed system to 100 to 400 psia (6.89 - 27.58 bar) for a pressure-fed system [46].

Since it is known that the internal pressure increases the buckling load of the cylinder [86], by decreasing the sensitivity to initial imperfections and axial and hoop stabilization [35], the advantage is taken, leading to extremely thin-walled thickness [46].

Huzel and Huang [46] differentiated two tank configurations for booster stage systems: pressure-stabilized and self-supported. For the former, the tank pressure must be continuously maintained above the specified threshold to prevent the structure from collapsing. Such tanks, also known as balloon tanks, are usually monocoque structures and were applied for the Atlas Intercontinental Ballistic Missile (ICBM). The majority of current structures are self-supported and require reinforcement (such as stringers or grids). Compared to other stiffened shells on launch vehicles, to avoid leakages, stiffeners are either integrally machined (best suited) or welded [21].

Sim et al. [76] conducted a study to determine KDFs for pressurized orthogrid-stiffened shells used in launch vehicle propellant tanks. The study used the ETTA1 cylinder geometry from NASA's SKBF project as the analytical model. Two imperfection modeling techniques were applied, SPLA & SBPA, and the results were compared to empirical knockdowns from NASA SP-8007 (KDFs used were based on the pre-2020 revision). A smeared-stiffness model was adopted, including weld land and transition region details. The analysis considered internal pressures ranging from 0 to 30 kPa, including the ETTA1 test pressures of 4.137 and 5.985 kPa. The results confirmed a strong dependence of the buckling load on the magnitude of the pressure. However, the increase in predicted load was highly dependent on the imperfection modeling approach, and the discrepancy between methods grew with increasing pressure.

For pressures below 10 kPa, SPLA models — both perfect and disturbed- yielded similar buckling loads. At the same time, SBPA predicted a continuous increase in the collapse load, with values consistently higher than those of the other models. The behavior of SPLA-modeled cylinders was attributed to increased global buckling resistance under internal pressure rather than to improved resistance to imperfections. For SPLA, KDFs remained nearly constant below 10 kPa but increased rapidly beyond that threshold. SBPA KDFs also increased with pressure, and similarly exhibited a sharp rise after 10 kPa. At ETTA1 test pressures, both SPLA and SBPA produced knockdowns close to the experimental results. However, SPLA's prediction exactly matched the test-derived KDF, rendering it potentially unconservative. SBPA, with slightly lower KDFs, was deemed more appropriate for highly stiffened shells due to its increased conservatism. The authors concluded that SBPA is more suitable for predicting buckling in orthogrid-stiffened shells. Nevertheless, Sim et al. [76] noted that the pressures used in the study are not representative of actual pressurization levels required by operational propellant tanks.

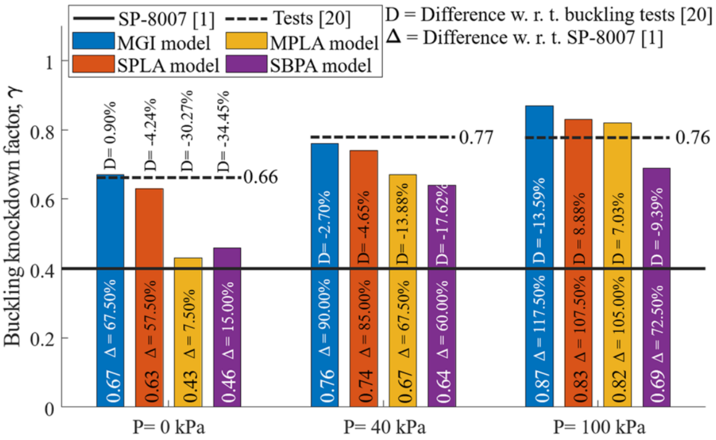

Figure 2.9: Comparison of KDFs obtained by [77].

The effect of imperfection modeling on the buckling response of unreinforced pressurized cylinders was investigated by Sim et al. [77]. Using a small-scale aluminum cylinder, the study compared the knockdown predictions of MGI, SPLA, MPLA, and SBPA across three pressurization levels: 0 kPa, 40 kPa, and 100 kPa. Results were validated against experimental data. The findings showed that internal pressure significantly increased the buckling load, with collapse loads rising by up to 117% depending on the imperfection modeling method as depicted in Figure 2.9. SPLA yielded accurate KDFs at lower pressures (0 and 40 kPa), while SBPA was more conservative and better aligned with test results at 100 kPa. MPLA consistently underestimated the buckling load, making it overly conservative. However, it was the only method that did not overestimate the knockdown factor at the highest pressure. This was attributed to the severe geometric imperfections modeled, which resulted in the largest reduction in the collapse load. Measured imperfections (MGI) produced results closest to experimental values but showed the greatest overshoot at 100 kPa. The study confirmed that both pressure level and imperfection modeling approach significantly influence the predicted collapse load. No single modeling technique was found to be optimal across all pressures: SPLA was more reliable at lower pressures, while SBPA offered more conservative results at higher pressures, where boundary-induced imperfections dominated. The authors recommend that future research focus on full-scale launch vehicle structures using pressurization levels representative of operational conditions.

2.9. Research Gap

It is evident from the literature that most work on metallic shell buckling focuses on deriving analytically more accurate knockdown factors than those in NASA SP-8007. These studies typically compute KDFs for specific launch vehicle shell geometries that have been built, measured, and tested. This approach limits the generality of the results, as only a few such structures are sufficiently documented in the open literature. Various imperfection modeling techniques are used to create realistic imperfection fields, followed by nonlinear geometric analysis to determine collapse loads. Authors usually compare predictions against experimental data and select one or more approaches deemed most suitable for generating conservative knockdown factors. However, few studies are truly comprehensive, analyzing a wide range of shells or evaluating the consistency and reliability of a method across multiple configurations.

In the pursuit of improved knockdowns, a critical issue is often overlooked: knockdowns are inherently configuration-dependent and not universal constants. The variation in imperfection patterns across configurations undermines the generality of any single KDF. Similarly, the accuracy of imperfection modeling methods strongly depends on the shell geometry and boundary conditions considered.

Despite this variability, there is evidence of recurring imperfection patterns—so-called imperfection signature, arising from specific manufacturing processes. When accurately reproduced, these signatures can yield more reliable predictions than generic knockdown factors. For metallic launcher shells, the dominant imperfection signature is widely attributed to the welding process, which generates long, inward-oriented half-waves along the weld lands. In some cases, the associated geometric features at the weld lands were shown to affect structural performance more significantly than the initial geometric imperfections. Yet, limited work has been devoted to identifying which modeling methods best replicate these signatures or to investigating whether matching the imperfection shape to the signature is necessary for reliable and accurate buckling predictions.

Another major shortcoming is the treatment of internal pressure in studies involving launch vehicle shell segments. While pressurization has a well-documented effect on buckling behavior—stiffening the shell, increasing collapse loads, and altering mode shapes—most studies either neglect it entirely or apply unrealistic pressure levels. The interaction between pressurization and imperfection modeling accuracy remains largely unexplored.

Finally, earlier work did not examine the reliability of these modeling approaches across multiple structural configurations, nor did it consider how the influence of imperfections evolves under the coupled effect of geometry and pressurization.

Main Objective and Research Question

The objective of this study is to determine whether the reliability of nonlinear buckling analysis for a pressurized metallic cylindrical tank segment depends on the imperfection pattern introduced. The main research question is defined as follows:

To what extent does the reliability of imperfection modeling approaches for pressurized metallic stiffened launch vehicle propellant tank segments depend on the recreation of the imperfection signature?

It is hypothesized that, among existing imperfection-modeling approaches, reliable predictions of collapse loads for pressurized shells can be achieved by inducing a distortion field that does not reproduce commonly observed imperfection signatures. Such an approach is expected to remain effective across different pressure levels and shell configurations, without requiring prior knowledge of the actual geometric imperfections present in the manufactured structure. If validated, this would reduce the reliance on extensive and costly geometric imperfection measurements and simplify the early-stage structural assessment of launch-vehicle tank segments.

To assess this hypothesis, buckling analyses will be performed on a set of realistic propellant-tank segments with welding-induced imperfections, subjected to varying levels of internal pressurization. The selected designs are adopted from the NASA SBKF project, as they represent current-generation launch vehicle structures. The study includes shells featuring both weld-land configurations—tapered stiffener transitions and picture-frame designs—to cover the relevant design space. The cylinders also span two diameter classes to capture variability associated with different vehicle scales. In total, five structures were analyzed: four 8-ft (2.4 m) test articles (TA01, TA03, TA07, TA09) and one 27.5-ft (8.4 m)full-scale segment (ETTA1).

To ensure that the selected shells could safely withstand the prescribed pressure range, their maximum proof pressure was calculated using Equation 2.2, following the recommendations of [57]. This expression estimates the highest internal pressure the cylinder can sustain without orthogrid-pocket yielding, typically verified during proof testing. It should be noted that, depending on the applicable standard and whether the vehicle is reusable or expendable, the resulting proof pressure may differ from the actual maximum expected operating pressure (MEOP).

$$p_{proof_{max}} = \frac{t \cdot \sigma_y}{R} \tag{2.2}$$

Based on the performance assessment, the selected pressure levels range from 0 bar (used to verify the models against existing analyses and test data) to 4 bar. While this does not span the full feasible domain, the upper limit is constrained by the designed yield margin of the structures. Applying higher pressures would require increasing the skin thickness, thereby altering the shell behavior and invalidating the comparison. Buckling analyses will therefore be performed in 2-bar increments. Unfortunately, the 4 bar pressure exceeds the yield pressure of the space shuttle tank (ETTA1). However, the shell, being the only structure with a large diameter and pressurized test results, was necessary in the study for completeness. To accommodate it, no analysis was conducted at this load magnitude. Instead, to enable verification under pressurized conditions, a pressure of 0.06895 bar (1 psi) was included specifically for this structure.

To address the role of imperfection signatures, the study considers both modeling strategies that explicitly replicate measured geometric deviations and approaches that induce representative buckling modes through simplified, non-physical imperfection fields. This dual treatment allows separating signature-driven responses from mode-driven responses and enables systematic assessment of how each method behaves under increasing internal pressure. The methods included are:

- **GNA (Geometric Non-linear Analysis)**: Baseline for perfect geometry performance under compression for non-linear analysis.
- **MGI (Measured Geometric Imperfections Approach)**: Where available, will serve as reference cases of the actual imperfection signature and for accuracy assessment.
- **EIA (Eigenmode Imperfection Approach)**: Industry standard method commonly used for nonlinear buckling analysis.
- **SPLA (Single Perturbation Load Approach)**: Cited as one of the most accurate, though sometimes considered conservative.
- **MPLA (Multi-Perturbation Load Approach)**: A simplified alternative that avoids optimization, capable of reproducing weld signatures; The influence of the number of perturbation loads on prediction quality will be studied.
- **SBPA (Single Boundary Perturbation Approach)**: Capable of capturing both traditional and non-traditional imperfection patterns, with improved accuracy under high pressure.

3

Methodology

In this chapter, the simulation set-up used for the shell buckling analyses is introduced and described in detail. Firstly, in section 3.1, the modelling of the structure segment in the CAD environment, followed by the import procedure into Abaqus CAE, is explained. Subsequently, the steps related to part generation, section partitioning, and material assignment are presented. In section 3.2, the FEA framework including: meshing strategies, boundary conditions, and loading definition, is discussed. Section 3.3 provides a detailed explanation of the implementation of the various imperfection fields considered in this study. The reliability assessment procedure, including the statistical measures employed, is deliberated upon in section 3.4.

3.1. Shell Modeling

The structures were modeled in Autodesk Fusion 360, enabling full parametrization of the shells and rapid generation of multiple geometries. The cylinders were created as surface bodies using the surface workbench - consequently, no thicknesses were assigned at the CAD stage. Several simplifications and modeling assumptions were introduced to accelerate the geometry creation process and streamline subsequent analyses.

For importing the measured imperfections, the Abaqus plugin developed within the DESICOS program was used. To ensure the measured fields are applied seamlessly, the CAD model's coordinate system followed the plugin's convention, with the vertical axis aligned with the positive z-direction. Each shell was modeled as an individual curved panel segment (consistent with the real manufacturing approach) and later patterned in Abaqus. The reference segment always started at the xz plane and was defined counter-clockwise around the z-axis, ensuring that the weld centerline consistently aligned with the global x-axis. This alignment was essential for matching the weld location with the measured imperfection data at the later stages. The small-diameter cylinders consisted of three segments (each $120°$), while the Space Shuttle external tank consisted of eight segments (each $45°$).

Compared to the originally manufactured SBKF test articles, the models were generated as idealized flight-hardware propellant tank segments. The design parameters used correspond to the as-designed geometry, all parameters are presented in Appendix A. The stiffened and extended ends required for the buckling jig were removed, and the segments were terminated with circumferential weld land geometry. The total height of each shell was reduced to exactly match the measurement window used in the structured-light/DIC setup described in Hilburger et al. [43], eliminating the later stretching of the measured imperfection field to the FEM mesh for the 8-ft cylinders. For ETTA1, the segment height was derived from Lovejoy et al. [58] based on Figure 11. Since the measurements were taken at the outer- mold-line (OML), the cylinder radius was set accordingly, requiring the stiffener height to be increased by the skin thickness to preserve the designed internal geometry - the impact of this assumption will be discussed by the end of this section.

Additionally, the stiffeners were modeled without tapering or fillets. This significantly reduced geometric complexity and modeling time, though, as discussed in section 4.5, it might have reduced the structure's effective stiffness. Each segment included two weld land regions -longitudinal and circumferential, with respective transition widths. The final CAD geometry was exported as a .STEP file to preserve the quality during import.

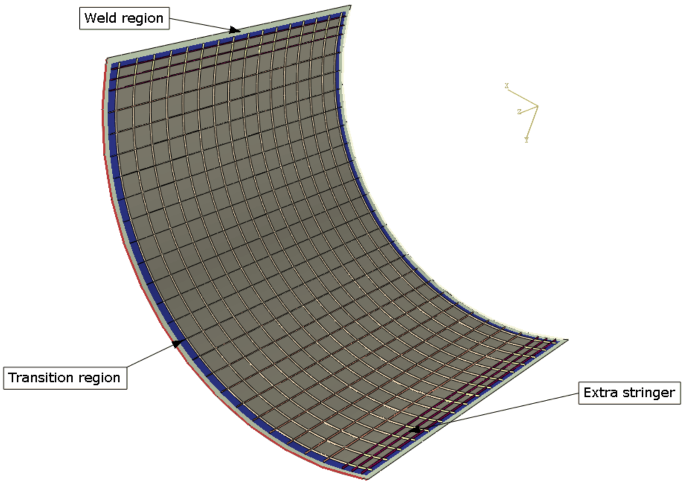

Figure 3.1: TA01 imported tank segment with indicated welds and transition regions.

In Abaqus, the import was performed using the 'combine into a single part' option with a stitching tolerance of 10^{-4}, resulting in a uniform surface body. This avoided the need for numerous constraints or contact definitions otherwise required to connect shell skins with stiffeners, thereby reducing computational cost.

After import, a Python script assigned all surface regions to predefined sets to facilitate later section assignments. A representative example of this stage is shown in Figure 3.1. The script grouped surface, faces, and edges into desired sets, which were used later for shell and boundary condition assignments. An independent instance of the segment was then created in the assembly module and patterned radially. This ensured that identical faces on each repeated segment were consistently assigned to the same set. After patterning, the copied instances were deleted, leaving the final assembled surface, shown in Figure 3.2.

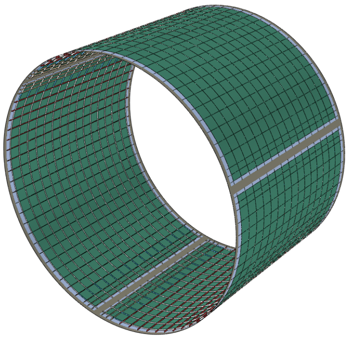

Figure 3.2: Full barrel of TA01 in ABAQUS.

The script automatically generated material properties and section assignments. In this study, the material was assumed isotropic and homogeneous. Although aluminum–lithium alloys exhibit slight orthotropy between longitudinal and transverse directions, this effect is evaluated in section 4.5. For weld lands, the material was assumed to be unaffected by friction-stir welding, consistent with previous studies [94].

The adopted material properties for Al–Li 2195 are listed in Table 3.1. The elastic modulus, density, and Poisson ratio for Al–Li 2195-T8M4 are taken from Hilburger et al. [43], while the yield strength for the T8R7 temper is taken from Lovejoy et al. [57]. It was noted that the small test articles were machined from 2195-T3 plate and subsequently heat-treated to the T83 condition after bump-forming [43].

Table 3.1: Material properties of Al–-Li 2195 alloy.

Material	E [GPa]	σ_y [MPa]	ν [-]	ρ [kg/m^3]
Al–Li 2195 – T8M4	75.8	503.0	0.3	2712.6

The shell sections were defined with constant thickness and the default five Simpson integration points. Hilburger [37] suggested using the inner-mold-line (IML) as the reference surface for the shell mesh to ensure that the external surface remained flush, as shown in Figure 3.3.

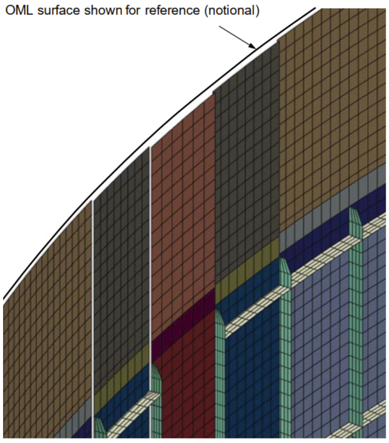

Figure 3.3: Typical test article isometric view showing weld land, transition, and stiffener details [43].

Since the present work used OML-based geometries to enable direct application of measured imperfections, the shell offset was set to the top, with the OML serving as the reference surface. For the orthogrid stiffeners, the default mid-surface definition was used, placing the reference surface at the center of the modeled stiffener height. The resulting offset strategy is illustrated in Figure 3.4, where the thick black lines indicate the CAD surfaces assigned as reference surfaces for the shell elements' thickness assignment. As discussed, because the OML was selected as the reference, the stiffener design height h_s was increased by the skin thickness, yielding a modeled stringer height H_s. The same modeling strategy was applied to the rings, whose width was similarly adjusted by the skin thickness.

This assumption introduces a small amount of artificial stiffness, as portions of the stiffeners' geometry and the shell skin effectively overlap. Nevertheless, it was assumed that this additional stiffness would not significantly influence the accuracy of the buckling simulations.

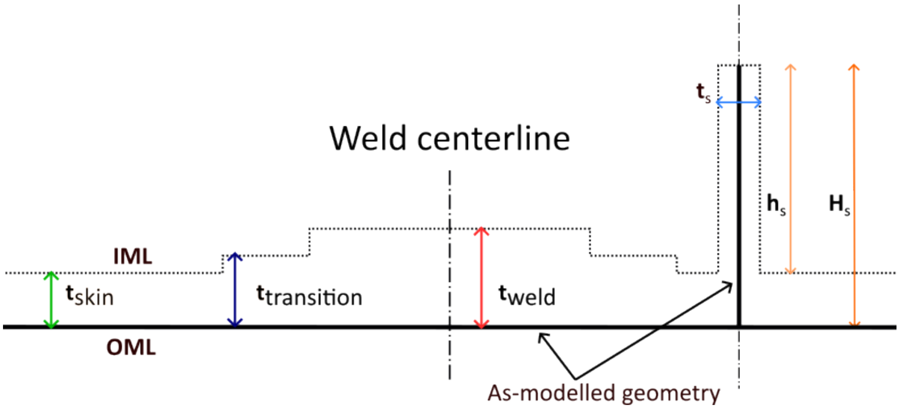

Figure 3.4: Shell modelling strategy overview.

3.1.1. Boundary Conditions

By default, the Python script automatically generated rigid-body tie constraints that coupled two remote points (RPs) with the upper and lower cylinder edges. Using the cylinder centerline as reference, these RPs were positioned on the top and bottom 'faces' of the cylinder and tied to the corresponding shell edges using rigid body tie constraints. The RPs were then constrained using appropriate displacement and encastre settings to replicate simply supported boundary conditions.

[26] argue that the boundary conditions of built-in flight hardware strongly depend on the stiffness of the adjacent structures. Fully clamped-clamped boundary conditions are only realistic when the cylinder is attached to axially stiff components, such as the y-rings located between the tank dome and skirts. The tank segment considered herein is intended to be welded above and below to neighboring segments. It is therefore not attached to a sufficiently stiff structure to justify fixed boundary conditions at both ends. Furthermore, [35] describes the simply supported boundary condition as conservative relative to the clamped-clamped condition used in physical testing.

A known drawback of simply supported boundaries is the potential for edge warpage, which is not representative for a mid-span tank segment [26]. However, Wagner [96] demonstrated that the difference in knockdown factor between a load-controlled dynamic analysis with warpage and a displacement-controlled dynamic analysis with fixed edges is on the order of 4.4%. Additionally, the author notes that warpage is not solely a consequence of the boundary condition itself, but also of how it is applied. When a rigid-body constraint is active, the edge cannot deform out of plane, effectively preventing warpage.

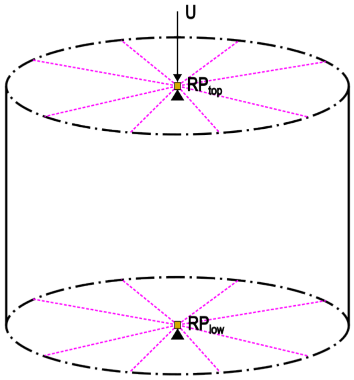

Figure 3.5: Overview of rigid body constraints and boundary conditions on a barrel segment.

Overall, the top remote point retained a single unconstrained degree of freedom in the vertical (z) direction, while the bottom remote point was fully fixed, allowing the upper edge to displace axially. The applied boundary conditions are shown in Figure 3.5. An identical setup with supported boundary conditions was used in [76] and [77].

3.1.2. Shell Meshing

The shell (including the stiffeners) was meshed with standard quadrilateral linear reduced-integration shell elements ($S4R$), consistent with past studies [43, 76, 94, 98]. The meshing process was performed manually to maintain full control over element distribution and mesh quality. For each shell, three meshing attributes were defined: a global part seed, local edge seeds, and sweep mesh control.

The element size was governed by the number of elements placed within each skin pocket. This number varied from 3 to 10 across the pocket width and from 7 to 9 in the vertical direction, consistent with the mesh-convergence findings of Hilburger et al. [43]. Such a mesh density was sufficiently fine to capture both local and global buckling behaviour. Further refinement resulted in less than a 5% change in collapse load, while achieving a 1% change would have required approximately doubling the total element count, significantly increasing simulation runtime.

At the weld land regions, Abaqus occasionally struggled to generate continuous level elements across the transition. As a result, elements near the weld centerline were more skewed compared to the average element in the skin pocket. To ensure that these elements did not adversely impact the analysis, a mesh-quality assessment was conducted. It was evaluated using Abaqus' in-built shape metrics: the aspect ratio (with an upper limit of 5) and the default element corner-angle criteria for quadrilateral faces.

3.2. Analysis Set-Up

The analysis set-up, independent of the imperfection modeling strategy, consisted of three distinct phases. First, the perturbation field was introduced to the geometrically perfect model. This was followed by a pressurization step, during which the structure was subjected to internal pressure. Finally, the segment was compressed axially during the buckling step. To capture the tank segment's nonlinear behavior, geometric nonlinearity was enabled for all steps.

In the pressurization step, the internal pressure was applied using an Abaqus pressure load in a static step. The load was assigned only to the internal surfaces of the cylindrical shell (including weld lands). It followed from the definition of the pressure load, which must act normal to the surface onto which it is applied. Consequently, applying pressure to the orthogrid stiffeners would result in sideways loading on the webs- not reflecting the actual physics of internal pressurization. It was assumed that the increase in stiffness due to pressure acting on the stiffener's thickness would be negligible relative to the overall shell response. Nevertheless, further investigation of this assumption is recommended.

For the compression step, two analysis procedures were considered: static and dynamic. Both have been used previously in buckling studies—static in [43, 50, 94], dynamic explicit in [26], and implicit in [29, 69]. [26] study revealed that displacement-controlled collapse loads obtained from nonlinear dynamic explicit analyses are lower compared to the nonlinear static analyses. On the other hand, the findings of [29] revealed that implicit buckling leads to higher collapse loads compared to the fully static arc-length approach, but on a conical structure. However, all the past findings were based solely on unpressurized shell structures. More recent studies involving internal pressure [76, 77] relied exclusively on static analysis. Therefore, a dedicated comparison was performed for TA01 to determine the preferred analysis type in terms of accuracy and runtime, as presented in section 4.2.

Similarly, force and displacement-controlled compression have been examined extensively and summarized by Friedrich and Schröder [26]. The authors reported that, for imperfect shells, the buckling loads obtained from these two approaches differ, with the magnitude of the difference depending on the perturbation method used. Bushnell [8] noted that displacement-controlled analysis permits stress redistribution around the perturbation and allows the structure to sustain load beyond the local snap-through event until global collapse is reached, later confirmed in [26]. Such characteristics are desirable when local buckling modes precede global instability, as they enable identification of all relevant buckling events. Consequently, a displacement-controlled buckling analysis was selected for this work.

3.3. Imperfection Modeling

Each perturbation was introduced differently depending on the corresponding approach, as outlined in this section. First, the traditional imperfection methods are presented, progressing from perturbation-dependent approaches through eigenmode-based and measured-imperfection techniques. Finally, the non-traditional imperfection approach is introduced.

3.3.1. SPLA & MPLA Set-Up

For SPLA and MPLA, a similar analysis procedure was applied. A nonlinear static step was defined in which one or multiple lateral perturbation loads (P) were introduced. A concentrated horizontal force was applied at a single node to generate an inward-facing dimple. The force components were calculated such that the resulting vector pointed towards the cylinder axis, depending on the x- and y-coordinates of the selected node.

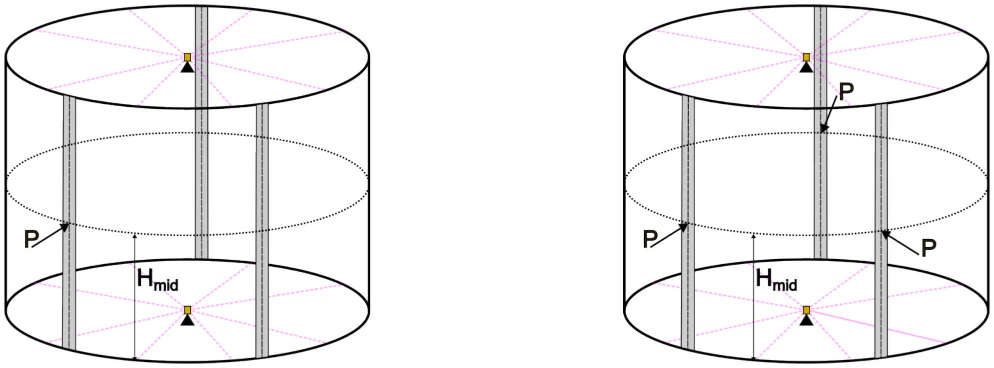

Figure 3.6: Shell models with indicated weld lands and perturbation force locations for SPLA (left) and MPLA (right).

The choice of perturbation location and its influence has been discussed extensively in previous studies and presented in section 2.5. In this work, the most suitable location was deemed to be the weld land centerline at the cylinder's mid-height (as presented in Figure 3.6), as this is the most likely region for inward dent formation caused by welding-induced imperfection signatures [82]. However, as noted in [30], this location often requires higher perturbation forces to achieve convergence and may yield slightly more conservative collapse loads than other positions on the segment. For MPLA, to avoid computationally intensive optimization of load locations, perturbation loads were placed at each weld land centerline, which may yield very conservative results.

Both SPLA and MPLA can, as demonstrated by Wang et al. [98], converge for perturbation loads that produce dimple amplitudes far exceeding any physically attainable manufacturing imperfection. To address this, the authors imposed a hard cap on perturbation loads that generated amplitudes exceeding three times the skin thickness. While this prevented unrealistic dimples, it rendered the method unconservative. In this work, a different convergence approach was adopted. Instead of monitoring the lateral perturbation load directly, the ratio of dimple amplitude to shell thickness was used. This provides a more direct indication of the perturbation's physical effect. To avoid overshoot, the maximum allowed amplitude-to-thickness ratio was limited to 10-14 (depending on the shell's skin thickness, as a constant range of perturbation loads between 100 and 7000 N was used). Although high, this limit ensures that convergence occurs within a more conservative buckling regime.

A key omission in previous studies concerns the definition of the convergence criterion. Earlier works appear to have selected convergence visually from the collapse-load–perturbation curve. However, as no explicit procedure was reported, a more robust mathematical criterion was developed. The simulation results were fitted using Python's SciPy optimize.curve_fit [71] routine with a modified stretched exponential function [24], defined in Equation 3.1, where N is the collapse load and P denotes the perturbation parameter.

$$N_P = N_\infty + A \cdot e^{-(\frac{P}{P_0})^n} \tag{3.1}$$

Once the fitted parameters were obtained, a perturbation range bounded by the minimum and maximum simulated values was generated and used to construct the trend line. Convergence was defined as the point where the collapse load reached the plateau region of this curve, evaluated using the parameter δ_P in Equation 3.2. Convergence was assumed when $\delta_P \leq 5\%$, ensuring that the identified perturbation lay within a stable and physically meaningful regime.

$$\delta_P = \frac{N_{fitted} - N_\infty}{N_{fitted_{max}} - N_\infty} \tag{3.2}$$

The corresponding perturbation load was then obtained using SciPy 's PCHIP interpolation, and the resulting load was subsequently reported and applied to verify the estimate.

In previous works, convergence was determined either at every considered pressure level [76] or only for the unpressurized case [77] (the latter remains unclear due to poor reporting). In this study, both approaches were evaluated to assess whether the difference is significant and whether the simplified approach (using a single convergence study) can serve as a viable option for future work. Thus, the methods *SPLAOG* and *MPLAOG* were introduced, with the perturbation load determined by convergence of the unpressurized baseline.

3.3.2. EIA Set-up

The eigenmode imperfection approach followed the classical definition from literature, using the procedure outlined by Castro et al. [11]. Unlike the other approaches, it required only two analysis steps: (i) applying the imperfection together with pressurization, and (ii) performing the compression step.

First, a separate model was generated for a linear buckling analysis to obtain the imperfection shape. The LBA used the same shell geometry and boundary conditions as the nonlinear model, but employed a force-controlled compression step. A single concentrated force of magnitude 1 N was applied to the upper remote point. The Lanczos eigensolver was used to extract a number of buckling modes. The number of retrieved modes depended on the size of the structure. For the 8-ft diameter shells, the first mode was used, as it corresponded to the global buckling shape. For the ETTA1, the first 100 modes were extracted to identify a global mode resembling the pattern reported in [35]. Unfortunately, the exact match could not be determined. Consequently, the closest-looking mode corresponding to mode 32 was selected instead.

In the nonlinear buckling model, the input file was modified to include the nodal displacement field of the selected eigenmode. The imperfection magnitude was set to half the shell's acreage thickness, following recommendations from literature (presented in section 2.4). The commands used to modify the input file were copied from [11]. Subsequently, for the pressurization analysis, the internal pressure was applied directly to the geometry perturbed step, followed by the vertical loading in the compression step

3.3.3. MGI Set-up

For the measured geometrical imperfection approach, the procedure involved altering the mesh node positions to match the outer mold line measurements recorded under NASA's SBKF programme. The mesh-alteration routine was executed using the DESICOS plugin, with detailed documentation available in [9]. The plugin requires a .txt file containing the vertical and circumferential coordinates of each node, together with the measured radial displacement. It then interpolates these values to the mesh node locations and applies the corresponding translations.

Because the measurement data in the required format were not publicly available, the imperfection fields were reconstructed from the published measurement plots in the SBKF reports, such as the example shown in Figure 3.7.

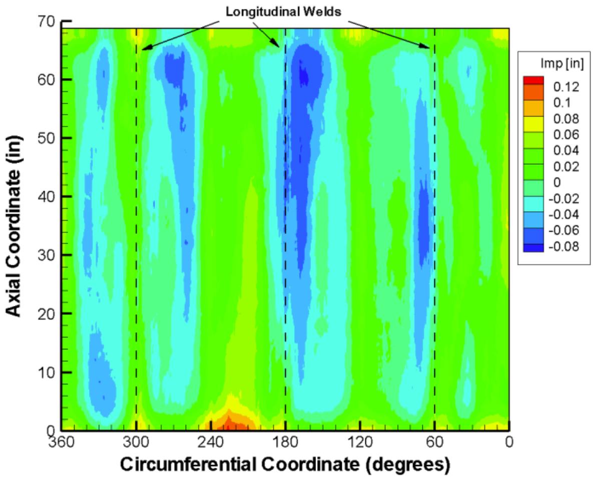

Figure 3.7: Outer mold line radial imperfections for TA01 [83].

The plots were first cropped and cleaned in Adobe Photoshop to remove axis labels and other artifacts, and to enhance color contrast for later processing. For TA03, no scale was provided on the published plot, and the maximum amplitudes were estimated based on the reported ranges of other 2.4 m diameter shells. The imperfection extrema were therefore set to ±0.10 inches for consistency.

The cleaned image was then processed in Python. The plot borders and any residual white regions were detected and removed. The remaining color field was then blurred to create a smoother transition between imperfections, as the original NASA plots were limited to a couple of levels, producing visibly stepped fields. Finally, each pixel's imperfection value was obtained by matching its RGB value to the nearest color in the processed scale. The values were then normalized between 0 and 1 and scaled to physical units using Equation 3.3, where δ_{max} and δ_{min} denote the extreme outward (positive) and inward (negative) measured imperfection amplitudes. This scaling is valid only when the image spans the full RGB range.

$$U_{scaled} = field_{scalar} \cdot (\delta_{max} - \delta_{min}) + \delta_{min}, \tag{3.3}$$

In cases where the processing steps compressed the color range, an additional scaling was applied Equation 3.4. It ensured that the extrema shown in the original plot are correctly reproduced in the final imperfection field. Although effective, this approach is not optimal, and future work should investigate faster, more accurate RGB-to-displacement conversion methods.

$$U^{*} = \frac{U_{scaled} - U_{scaled_{\mathrm{min}}}}{U_{scaled_{\mathrm{max}}} - U_{scaled_{\mathrm{min}}}} (\delta_{max} - \delta_{min}) + \delta_{min}. \tag{3.4}$$

The number of reconstructed grid points corresponded to the number of pixels in the processed image. The resulting continuous imperfection field is shown in Figure 3.8.

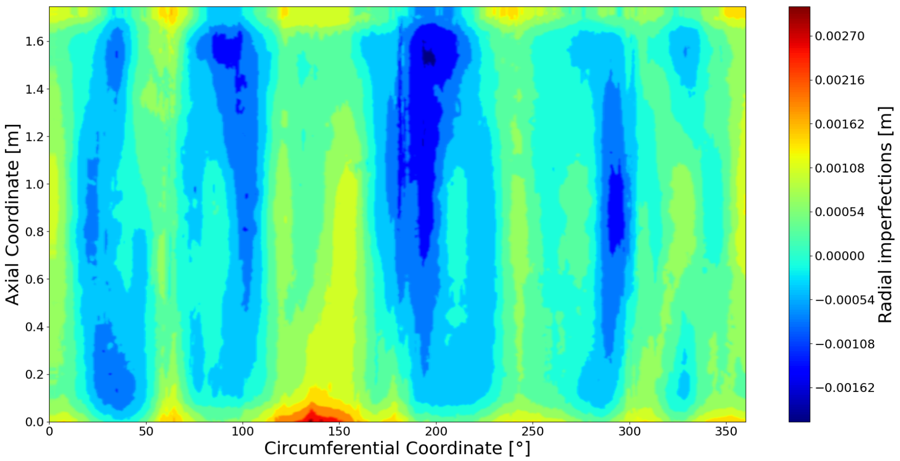

Figure 3.8: Reconstructed continuous radial imperfection map of TA01.

The extracted points were then written to the input .txt format required by the DESICOS plugin, the field was applied, and the mesh was regenerated. The final geometry resulting from the process is illustrated in Figure 3.9.

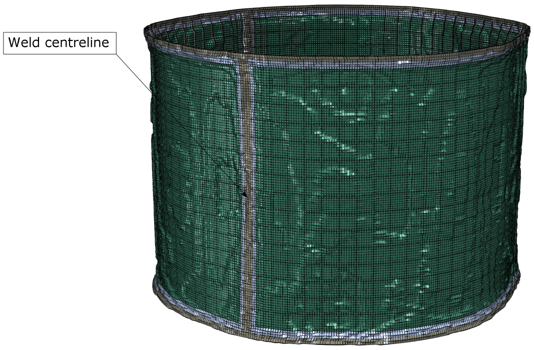

Figure 3.9: TA01 shell model in Abaqus with applied MGI field (magnified 50 times).

The resulting geometrically imperfect model was then analyzed directly in a nonlinear buckling step, without the need for an additional imperfection-application step. For pressurized analysis, the pressure load was applied directly to the disturbed mesh, followed by the non-linear buckling analysis.

3.3.4. Distributed Force Perturbation Approach

The Distributed Force Perturbation Approach (DFPA) was a method developed to replicate the behaviour of the Single Boundary Perturbation Approach (SBPA), while significantly simplifying the modeling process. SBPA requires modeling a variable-height shim on top of the cylinder and a rigid plate compressing the structure. The two must be connected through nonlinear contacts, which increases computational cost and modeling complexity.

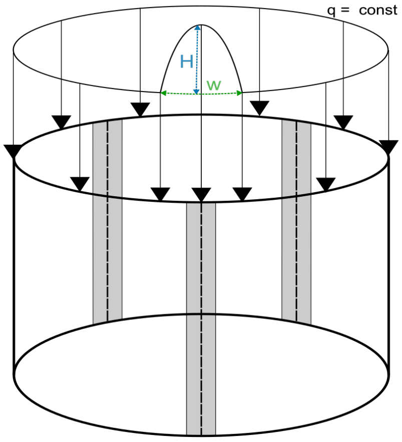

Figure 3.10: Schematic representation of DFPA.

Similar to SBPA, DFPA is a non-traditional imperfection method. Instead of introducing a geometric imperfection at the boundary, it induces buckling by varying the applied compression along the cylinder's edge. Locally increased compression triggers the formation of an inward-facing dimple, which subsequently propagates until global collapse is reached. The approach proved to represent the buckling load mode obtained in past studies, as demonstrated in Figure 3.11

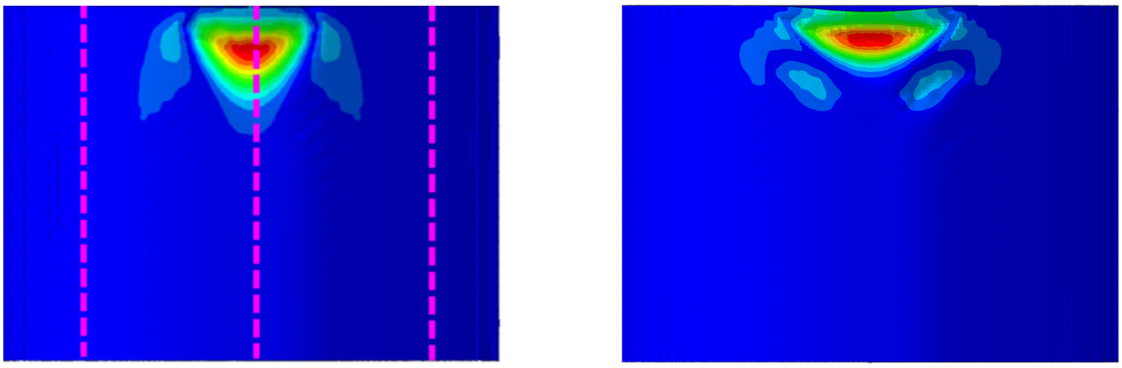

(a) SBPA global buckling mode for ETTA1 at 1 psi internal pressure, with indicated weld lands [76].

(b) DFPA global buckling mode for ETTA1 at 1 psi internal pressure.

Figure 3.11: Comparison of global buckling modes obtained using SBPA and DFPA.

A user-defined Fortran subroutine was written to define a shell edge load with a variable magnitude along the circumference. The perturbation is introduced as a cosine-shaped bump centered on one of the weld land centerlines (the one positioned over the x axis for easy visualization). At the same time, the remaining circumference is subjected to a constant compressive load. The load distribution magnitude α over the predefined angular width w is defined by Equation 3.5, where q - the constant shell edge load γ is the scaling factor and arg is the local angular coordinate within the selected width (ranging from 0 to 2, with $arg = 1$ at the bump center).

$$\begin{aligned} \alpha &= q \cdot (1 + \gamma \cdot \omega) \\ \omega &= 0.5\,(1 - \cos(\pi \cdot arg)) \end{aligned} \tag{3.5}$$

Both the angular width and the load magnitude were subjected to preliminary optimization, discussed in section 4.3. A visualization of the loading pattern is provided in Figure 3.10.

As DFPA was load-controlled, it required a modification of the upper boundary condition. Instead of using a remote point, the end nodes at the top of the barrel were constrained in the horizontal directions, while remaining free to move axially.

The weld land region was selected as the perturbation location, rather than the acreage, because it typically results in buckling at a lower load level and therefore represents the more critical condition. As discussed in [82], the increased local thickness combined with the reduced bending stiffness makes weld lands susceptible to forming inward dimples at lower compressive loads than the acreage. However, for SBPA, [94] reported that perturbing the weld land or the center of the acreage panel produced identical collapse loads.

For cases involving internal pressure, the analysis steps are ordered similarly to those applied for MGI and EIA. Following the SBPA procedure adopted in [76], the geometrically perfect shell was first pressurized, after which the unsymmetrical compressive load was applied. Similarly to SPLA/MPLA, a variant of the method with converged scaling factor at unpressurized baseline - *DFPAOG*, was tested with higher pressures to determine the possible discrepancy.

3.4. Reliability Analysis

To assess the reliability of the considered imperfect buckling approaches, several statistical reliability measures were employed. Although the study is comprehensive in scope, covering five structures, seven imperfection methods, and up to three pressure levels, the resulting dataset remains limited from a statistical standpoint. Reliability analyses typically rely on substantially larger sample sizes. Nevertheless, the available data are sufficient for the selected measures, while acknowledging that their robustness could be improved with additional data points.

Further complications arise from the data structure itself. Not all shells were evaluated at identical pressure levels. The ETTA1 shell could only sustain pressurization up to 2 bar, resulting in an imbalance across pressure levels that had to be addressed individually for each statistical measure. Despite these limitations, the analysis establishes a consistent framework for future extensions involving additional shells and pressure levels and already provides insights that would otherwise remain inaccessible.

Prior to applying the statistical measures, the buckling data were normalized to eliminate issues with the collapse load magnitude disparities. Conventionally, knockdown factors are defined by normalizing collapse loads with experimentally obtained buckling loads. However, since the true buckling loads of the considered shells under the selected pressure levels are unknown, an alternative normalization strategy was adopted. In this work, the collapse loads for each structure were normalized by the mean buckling load obtained across all applied methods. The mean, rather than the median, was selected to account for both the most and least conservative predictions, yielding a moderately conservative reference level.

3.4.1. Inter Quartile Range Analysis

The interquartile range (IQR) is a measure of data dispersion that can be easily visualized by a box plot. The IQR provides information on the data's central tendency (the data mean) and the overall dispersion [20].

IQR was the first step in the reliability analysis because it is easily visualized and interpreted. It allowed the identification of outliers and thus possible abnormal shell behaviors, serving simultaneously as a sanity check for the simulation runs. The IQR was interpreted using whisker/box plots and assessed visually on the normalized spread. Imperfection approaches resulting in a more consistent, tighter spread were deemed more reliable.

3.4.2. Coefficient of Variation

The coefficient of variation is a statistical measure of relative variability or dispersion of data [20]. It is calculated as the standard deviation of the data divided by its mean, as expressed by Equation 3.6.

$$CV = \frac{\sigma}{\mu} \tag{3.6}$$

Applied in the context of this work—per buckling method across the structures at each pressure level—it assessed the dispersion of the buckling approach overshoot. The higher the CV, the greater the dispersion in the variable, and the lower the relative (within-method) reliability.

However, the coefficient of variation is appropriate only for datasets that exhibit heteroscedasticity, where the residual variance increases with the mean [72]. Consequently, heteroscedasticity was first assessed using the Breusch–Pagan test [7], one of the most commonly applied diagnostics for variance non-constancy in empirical data [28]. Based on the test's p-value, the null hypothesis of homoscedasticity (constant variance across observations) is evaluated. For p-values below 0.05, the null hypothesis is rejected, and the data are considered heteroscedastic. Had the buckling data been confirmed as homoscedastic, the coefficient of variation would not have been applied.

The test was performed using statsmodels version 0.14.4 with the het_breuschpagan routine [81]. This implementation provides both the original Breusch–Pagan Lagrange Multiplier (LM) test and the Koenker–Bassett variant, which offers a more robust variance estimator - independent of normally distributed errors [28]. In this work, the robust Koenker version is used together with the associated F-statistic, which provides more reliable small-sample inference compared to the original LM statistic [28]. To apply the Breusch–Pagan test, a simple least-squares regression model was first fitted using statsmodels.api.OLS [80]. The buckling load was regressed against the combined effects of method and pressure, providing the residuals and fitted values required for the BP heteroscedasticity diagnostic.

3.4.3. Coefficient of Concordance

Kendall's coefficient of concordance, or Kendall's W, is a non-parametric technique that measures the agreement among several judges ranking a number of objects [54]. Kendall's W is an ideal method for this work because, as outlined by Legendre [54], the obtained data can be easily ranked in terms of its magnitude (for this technique the buckling normalization is not necessary), does not require a normal data distribution (which cannot be guaranteed with buckling data), and allows for more than two raters (structures or pressure levels) to be used simultaneously.

The calculation starts by ranking the objects per judge (in Python using the rank() command, which orders the values from lowest to highest). The ranks are then summed per object, denoted as R_i, and their mean across all raters is calculated as shown in Equation 3.7.

$$\begin{aligned} R_i &= \sum_{j=1}^{m} r_{ij} \\ \overline{R} &= \frac{1}{n}\sum_{i=1}^{n} R_i \end{aligned} \tag{3.7}$$

Lastly, the sum-of-squares statistic is obtained across all the objects, allowing the calculation of Kendall's coefficient as defined in Equation 3.8. A Kendall's W of 1 indicates perfect agreement among raters (identical rankings), whereas lower values indicate greater disagreement.

$$\begin{aligned} S &= \sum_{i=1}^{n} (R_i - \overline{R})^2 \\ W &= \frac{12S}{m^2(n^3 - n)} \end{aligned} \tag{3.8}$$

In this study, Kendall's W was used in two ways. Firstly, it served to assess the relative order of the imperfection modeling approaches across pressure levels per structure. It indicated how consistently the methods estimated the buckling loads across the pressures. In this context, the W values of all structures were compared. If the coefficients differed substantially between the structures, it implied that the pressure–structure interaction affected the buckling behavior more strongly than the imperfection modeling approach, indicating that the response of the method is structure or pressure-dependent.

Secondly, it was employed to check whether the structural responses across pressures remained consistent. This established the absolute reliability between methods and determined the ranking variability — indicating how constant the degrading effect of a given method remained across pressure levels. A higher W indicated higher reliability in ranking the methods, independent of whether they were more or less conservative.

In both approaches, the objects (n) were the methods, and the judges (m) were the three pressure levels. In the second approach, all buckling loads per pressure were ranked (a total of 9 objects), whereas in the first, only one load per structure (5 objects in total) was considered.

3.4.4. Intraclass Correlation Coefficient

The intraclass correlation coefficient (ICC) "assesses the reliability of ratings by comparing the variability of different ratings of the same subject to the total variation across all ratings and all subjects" [102].

It is widely used in reliability studies, particularly in medical and psychological research. The ICC values range from 0 to 1, with values closer to 1 indicating stronger reliability [52]. Although no universal thresholds exist, it is generally accepted that "ICC values less than 0.5 are indicative of poor reliability, values between 0.5 and 0.75 indicate moderate reliability, values between 0.75 and 0.9 indicate good reliability, and values greater than 0.90 indicate excellent reliability" [67].

In this work, ICC was applied in two principal ways. The first assessed the reliability of method performance across structures at constant pressure — indicating whether the structures rated the methods consistently. By comparing ICC values across pressures, it was possible to determine whether higher pressure led to greater overall method reliability. In this case, the coefficient was computed per pressure level, with methods set as targets and rated by the normalized buckling loads of the shells.

Secondly, ICC was used to evaluate whether methods estimated buckling consistently across different pressures, and whether the observed variance arose from structural behavior or pressure-related effects. This analysis revealed whether a method's reliability depended on pressure - that is, how likely its outcome was to change with increasing pressure. It therefore assessed the reliability of each method with respect to pressure, determining whether the imperfection introduction effect remained constant or pressure-dependent. Here, the coefficient was computed per method, using the cylinders' buckling loads as targets rated across all three pressure levels. Different ICC forms utilize separate models, rater types, and definitions. To select the most appropriate ICC form for the approaches outlined above, the guideline presented by Koo and Li [52] was followed.

Since all data obtained in the study had to be used, the raters could not be selected at random. Consequently, a two-way mixed-effects model was adopted. This limited the analysis to the statement that "the results only represent the reliability of the specific raters involved in the reliability experiment".

A single-measure ICC formulation was adopted. First, single-measure ICCs provide a more conservative [52] and therefore a more informative assessment of reliability. Second, averaging the pressure- or structure-dependent response would be physically unjustified, as each pressure level represents a distinct loading condition rather than interchangeable repeated measurements.

Lastly, the ICC definition was set to consistency setting, as each rater evaluated a group of subjects rather than repeatedly scoring the same one, which is required for absolute agreement.

In summary, based on the preliminary analysis, the ICC(3,1) form—following the convention of Shrout and Fleiss [73] was employed. ICC estimates and their 95% confidence intervals were calculated using Penguin package based on a single-rating, absolute-agreement, 2-way mixed-effects model [85]. Mathematically, the ICC is represented by Equation 3.9, where MS denotes the mean squares, with MS_{rows} referring to the variation between subjects and MS_{error} to the residual error, and k denotes the number of raters, corresponding either to the number of structures in the per-pressure analysis, or to the number of pressure levels in the per-method analysis.

$$ICC(3,1) = \frac{MS_{\text{rows}} - MS_{\text{error}}}{MS_{\text{rows}} + (k-1)MS_{\text{error}}} \tag{3.9}$$

However, ICC relies on two important data assumptions: normality (i.e., normally distributed data) and homoscedasticity (homogeneity of variance) [60, 73]. As the behavior and distribution of buckling data were not known a priori, both assumptions were verified.

To assess data normality, the Shapiro–Wilk numerical test was employed, as it is one of the most widely used methods. The test uses the null hypothesis that the data are normally distributed. A p-value greater than 0.05 would confirm the hypothesis [62]. To test for homoscedasticity, the Breusch–Pagan test was applied again. For ICC, unlike the coefficient of variation, the null hypothesis of equal variances had to be confirmed. Therefore, practically, only one of the methods could have been applied, depending on the data heteroskedasticity.

Nevertheless, [6] challenged the assumption of homogeneity of variance, arguing that these conditions are rarely met in practice. In their work, it was demonstrated that ICC could still be applied to assess reliability provided that potential heteroscedasticity was acknowledged or statistically adjusted for. Consequently, the final decision whether to include both ICC and CV in the reliability will be made post data generation and method assumptions verification.

Lastly, the ICC model implemented in the Python Pingouin package required balanced data [85]—that is, all targets had to be rated by the same number of raters. Since ETTA1 lacked the 2 bar pressure case, for the second ICC calculation, the shell either had to be excluded or its buckling loads duplicated from the 2 bar case. As the shell's performance was still unknown, the final approach was to be established after the simulation data were obtained.

4

Verification

In this chapter, the proposed analysis setup is verified against available literature data. Since no pressurized buckling results exist for the selected shells within the required pressure range, most cylinders were neither tested nor analyzed under pressure, a full validation is not feasible. Partial validation is, however, possible: ETTA1 provides a limited pressurized reference, albeit at pressure far below those considered in this work. Nevertheless, all shells can be verified in the unpressurized state, which primarily assesses the modeling of the segments rather than their pressurized behavior.

Section 4.1 presents the geometric verification using the effective thickness formulation. The final selection of the analysis procedure (static vs dynamic) is discussed in section 4.2. The optimization of the distributed-force perturbation approach is detailed in section 4.3. The numerical model verification and investigation of identified discrepancies are reported in section 4.4. Finally, a brief sensitivity assessment of the modeling assumptions is provided in section 4.5.

4.1. Effective Thickness Verification

The initial verification of the gathered geometrical data (and unit conversion, as most data were published in imperial units) was performed using the effective thickness-to-radius ratio (R/t_{eff}). The effective isotropic thickness t_{eff} provides a convenient means to represent the stiffness of a grid-stiffened cylinder in terms of an equivalent isotropic shell. The corresponding slenderness is then characterized by the ratio R/t_{eff}. For orthogrid-stiffened structures, it is defined by Equation 4.1 [37], where A_{11} and A_{22} correspond to the axial and circumferential membrane stiffness, and D_{11} and D_{22} to their bending stiffness counterparts. The detailed stiffness matrix calculations are presented in Appendix B.

$$t_{eff} = \sqrt[4]{\frac{144 \cdot D_{11} \cdot D_{22}}{A_{11} \cdot A_{22}}} \tag{4.1}$$

Table 4.1: Geometry verification based on slenderness ratios.

Structure	R/t_{eff}	**Reported** R/t_{eff}
TA01	226.1	230.9 [35], 226 [94]
TA03	80.1	84.1 [35], 80.1 [43], 81 [94]
TA07	172.9	172.9 [43]
TA09	125.7	125.7 [43]
ETTA1	309.3	326.4 [35], 309 [94]

The calculated R/t_{eff} ratios for the considered shells are presented in Table 4.1, the obtained thicknesses, in principle, show good agreement with those reported in the literature. The largest deviations occur for TA01 and ETTA1, with a smaller discrepancy for TA03 when comparing to the SBKF dataset compiled by Hilburger et al. [35]. Both TA01 and ETTA1 calculated thicknesses underestimates the shell's stiffness, reaching approximately 98% and 95% of the reported values, respectively. Both segments were also investigated by Wagner et al. [94], who reported R/t_{eff} ratios identical to those obtained in this work.

A plausible explanation for observed discrepancies is that one or more grid parameters were reported incorrectly or rounded inconsistently in past work. The effective thickness of ETTA1 was additionally published by [76], but when used, it yields $R/t_{eff} \approx 38639$, suggesting a reporting error.

For TA03, two values are listed in the SBKF dataset—one matching the ratio obtained here and another approximately 5% higher. Wagner et al. [94] reported a slightly elevated value as well, lying between these two. The ratios obtained for the remaining shells are identical to those presented in [43], likely because the grid parameters were taken directly from the same article. Interestingly, if the TA03 parameters had been adopted from that source, the resulting ratio would be 54.3 instead of 80.1.

In summary, the cylinder parameters used in this study are in close correspondence with those documented in the SBKF literature. Minor deviations in the effective stiffness of certain shells may, however, result in slightly lower buckling loads compared to the SBKF reference results. This effect is examined further later in this chapter.

4.2. Analysis Type

Dynamic and general static analysis methods have been proposed in past shell buckling studies, and in this section, the results of both are discussed to determine the preferred approach for this work. The effect of both analysis types was evaluated using the TA01 structure as reference, together with single and multiple perturbation loads, eigenmode imperfections, and measured imperfection mappings. A single shell was selected due to the project time constraints and because analyzing only a subset of methods would make it difficult to separate the shell–method behavior from the influence of the analysis type.

The general static analysis employed a nonlinear Newton–Raphson procedure. The maximum and minimum increment sizes were set to 10^{-1} and 10^{-15}, respectively. A constant damping factor of 10^{-6} was applied. Stabilization values have varied in past works from 5×10^{-2} [37, 77] to 10^{-7} and 10^{-6} [26, 94]. The applied stabilization introduces an artificial viscous damping force that dissipates residual energy during the Newton iterations [14]. While this improves convergence, an excessively large factor can artificially elevate the effective tangent stiffness at the bifurcation point, potentially increasing the predicted collapse load. The initial increment was set to 0.1, and the maximum number of increments was limited to 200–350 to ensure that the buckling event and part of the post-buckling response could be captured. The maximum number of iterations per increment was increased to 25. Solver parameters not explicitly discussed in past studies were left at default settings.

Dynamic implicit analysis was also considered, as it does not rely on user-specified artificial stabilization and therefore avoids the risk of selecting a damping value that could influence accuracy. It has been successfully applied in previous shell buckling studies [29, 69]. ABAQUS uses the Hilber–Hughes–Taylor (HHT-α) time integration scheme by default — an extension of the Newmark β-method, with a numerical damping parameter of $\alpha = -0.05$ [14]. This numerical damping is an artifact of the numerical method, and it is not related to the actual (physical) dissipation, i.e., viscous damping affecting the model's stiffness for non-linear analysis. In the HHT-α scheme, it suppresses high-frequency numerical oscillations (introduced by the variable time step) by using weighted equations of motion, with damping-based weights. The application type was kept as transient fidelity - indicating minimal energy dissipation, consistent with past work of Rudd et al. [69] and Guo et al. [29]. Following the recommendation, 10% of the step duration was used for the maximum time step (0.1), while the minimum was set to 10^{-10} [13]. The maximum number of iterations is set to 100-150. The load application was ramped in time to mimic quasi-static loading and improve convergence.

For DFPA, both analysis types were attempted. The static solver, however, failed to converge under the predefined stabilization value. Convergence required increasing the factor above 5%, which would significantly influence the predicted buckling load due to the artificial suppression of instability. Dynamic implicit analysis, therefore, remained the only viable approach for DFPA.

For both analysis types, the simulations were parallelized using 10 processor cores with GPU acceleration. The number of cores was selected based on an internal optimization study of the run-time behavior. The multiprocessing mode was set to MPI. To assess the analysis type, accuracy, CPU resource usage, and wall-clock time were considered. As noted in [29], static buckling analysis tends to yield lower collapse loads, making it more conservative, it was vital to inspect the values for this behavior. CPU usage and runtime are especially relevant for perturbation-based approaches, where many simulations are required for convergence. The comparison was performed at three pressure levels to assess whether internal pressure alters the relative behavior of the methods.

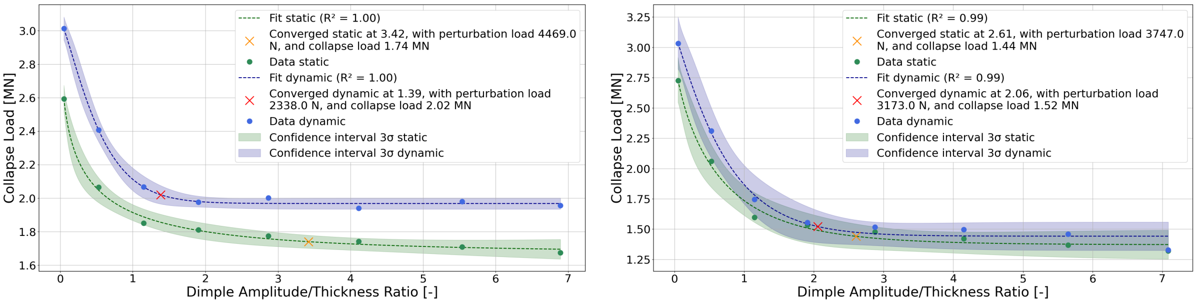

(a) SPLA 0 bar

(b) MPLA 0 bar

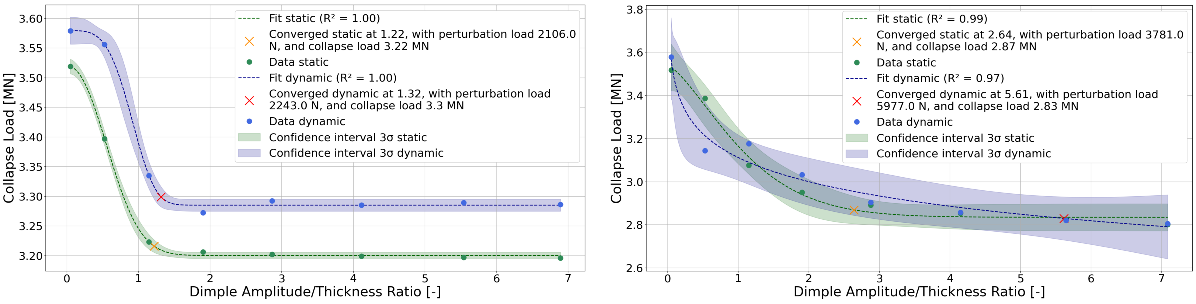

(c) SPLA 2 bar

(d) MPLA 2 bar

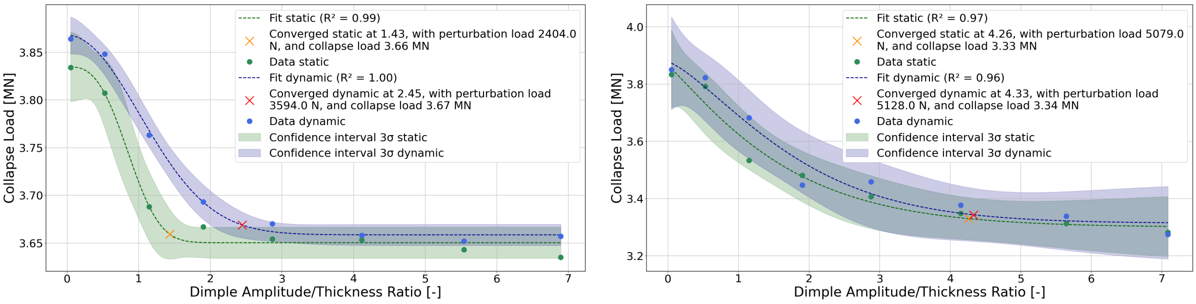

(e) SPLA 4 bar

(f) MPLA 4 bar

Figure 4.1: Convergence studies for MPLA and SPLA across pressure levels.

The collapse loads from both analysis types are of the same order of magnitude, as shown in Table 4.2. The most significant differences occur in the unpressurized case between the measured and single perturbation approaches, reaching up to 16%. With increasing pressure, the discrepancy decreases, yielding only a 2% difference for MPLA at 4 bar. Overall, the findings confirm the observations of Guo et al. [29] that static analysis yields lower collapse loads. To further assess convergence behavior, the convergence curves for both analysis types are presented in Figure 4.1 for the unpressurized, 2 bar, and 4 bar configurations.

Both analysis types exhibit similar convergence trends, consistent with observations from Friedrich and Schröder [26]. The largest differences occur for SPLA at 4 bar and MPLA at 2 bar. MPLA, however, converges to nearly identical buckling loads across all pressure levels, with similar perturbation loads for both the unpressurized and 4 bar cases.

Table 4.2: Comparison of static and dynamic buckling loads across pressure levels. Methods marked with * denote per-iteration loads (multiple iterations required).

	0 bar		
Method	**Static [N]**	**Dynamic [N]**	**Load Δ%**
MSI	2.24×10^{6}	2.53×10^{6}	13.2
EIA	1.59×10^{6}	1.63×10^{6}	2.5
SPLA*	1.75×10^{6}	2.02×10^{6}	15.7
MPLA*	1.44×10^{6}	1.52×10^{6}	5.6
	2 bar		
Method	**Static [N]**	**Dynamic [N]**	**Load Δ%**
GNA	3.52×10^{6}	3.58×10^{6}	1.7
MSI	3.45×10^{6}	3.58×10^{6}	3.9
EIA	3.00×10^{6}	3.00×10^{6}	-0.2
SPLA*	3.22×10^{6}	3.30×10^{6}	2.6
MPLA*	2.87×10^{6}	2.87×10^{6}	0.2
	4 bar		
Method	**Static [N]**	**Dynamic [N]**	**Load Δ%**
GNA	3.83×10^{6}	3.86×10^{6}	0.8
MSI	3.84×10^{6}	3.89×10^{6}	1.5
EIA	3.65×10^{6}	3.69×10^{6}	1.1
SPLA*	3.66×10^{6}	3.67×10^{6}	0.3
MPLA*	3.33×10^{6}	3.34×10^{6}	0.4

Overall, the differences in predicted collapse loads and convergence behavior between static and dynamic implicit analysis were sufficiently small that accuracy alone did not determine the choice. The CPU and wall-clock performance, however, differed more noticeably. Static analyses generally exhibited lower average CPU usage per increment, but identifying the peak reaction force required several post-buckling increments. In practice, this stage became more computationally intensive in the static procedure, requiring significantly more increments than the implicit dynamic scheme, resulting in longer run times. Based on the combined accuracy and run-time considerations, the dynamic implicit method was selected for this work.

4.3. DFPA Optimization

The introduction of the distributed load based imperfection modeling approach required preliminary optimization of the bump width and scaling factor before applying DFPA to all shells. The optimization was performed on ETTA01.

For the angular width, several values were considered, starting from 2°, which is reported as optimal for SBPA for cylinders with R/t_{eff} below 200 [93]. The sequence then continued through 5° and extended up to 120°. For the cosine-bump magnitude, scaling factors up to 14 were tested for widths up to 15°, and up to 10 for wider bumps. These limits were selected under the assumption that convergence would occur within this range. As described in subsection 3.3.4, the convergence behavior for each width was analyzed to evaluate the method's general characteristics. The results of this study are presented in Figure 4.2.

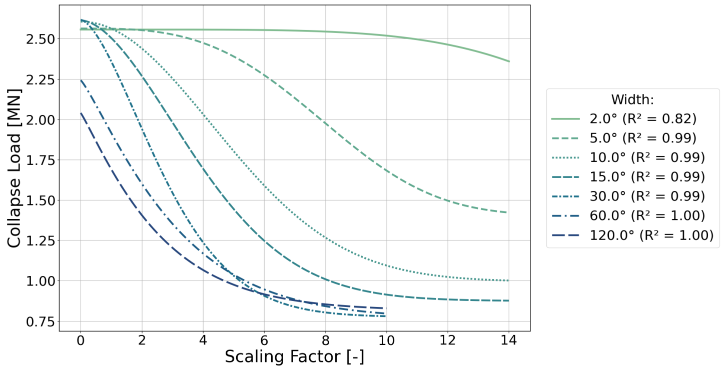

Figure 4.2: Convergence study with respect to DFPA angular width.

In practice, angular widths of 5° or more can be adequately modeled by a stretched-exponential function and exhibit clear convergence. At low scaling factors, however, both 2° and 5° widths show nearly linear, constant behavior. Inspection of the corresponding buckling modes reveals that, for scaling factors below 4 (for 5°) and below 8 (for 2°), the deformation patterns are nearly identical, featuring two dominant half-waves located away from the bump introduction at 0°, as shown in Figure 4.3. As the perturbation amplitude increases, these two waves migrate toward each other until they merge over the central weld, forming a single dominant dimple. Further increase of magnitude broadens this dimple to the point that additional perturbations have no measurable influence on the collapse load. The 2° width appears insufficient to capture this transition within the selected perturbation-magnitude range, preventing convergence and resulting in the low R^2 of the fitted trend line.

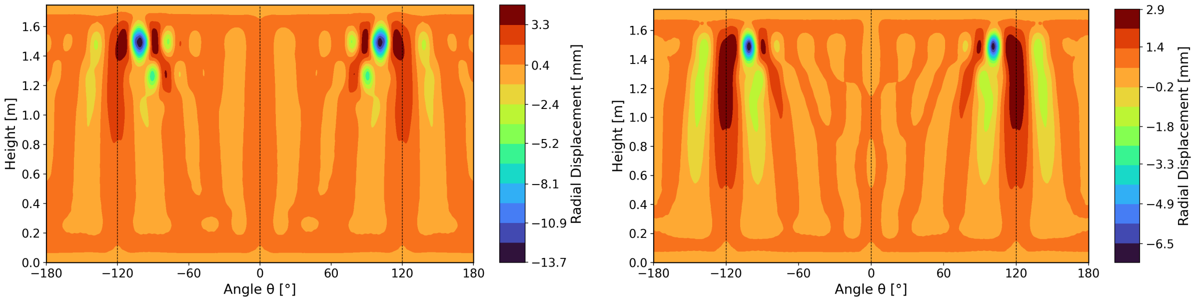

(a) 2.0 scaling factor

(b) 4.0 scaling factor

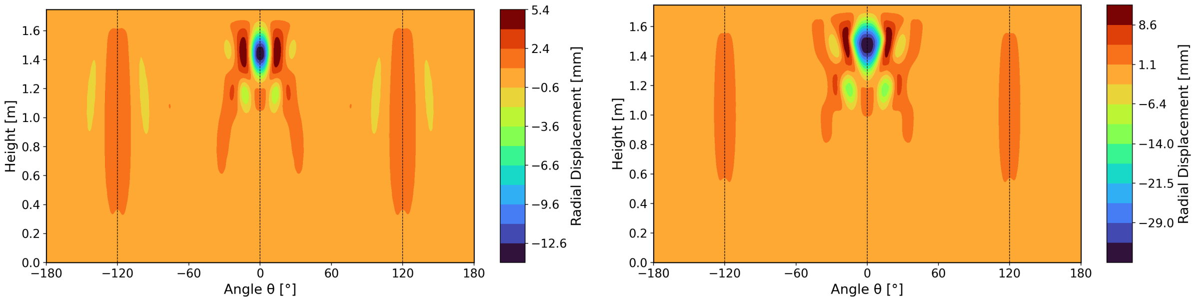

(c) 6.0 scaling factor

(d) 8.0 scaling factor

Figure 4.3: Buckling mode evolution for increasing DFPA scaling factor for TA01 with 5° angular width.

Wider bumps (30°–120°) generally produce better fits with the stretched-exponential function and converge at lower scaling factors compared to narrower bumps. Nevertheless, their converged collapse loads are overly conservative, typically dropping below 50% of the initial value. Intermediate widths (10° and 15°) also show convergent behavior and are less conservative, although the resulting collapse loads remain undesirably low compared to other modeling approaches.

Overall, a width of 5° provides the most balanced performance - convergence is achieved at a moderately high scaling factor, and the corresponding collapse loads are less conservative than for wider bumps. Nevertheless, DFPA remains more conservative than SBPA, despite producing a very similar buckling mode pattern. This discrepancy may arise from the different boundary-condition assumptions. In the SBPA, all edge nodes are tied together using a rigid loading plate, whereas in the DFPA, only local edge nodes experience increased compression. Alternatively, the difference may be attributable to the loading mechanism itself. In SBPA, the shim induces a bending moment at the edge, while DFPA relies solely on compressive loading.

4.4. Model Verification

For the FEM model verification, three buckling analysis methods were used: linear bifurcation buckling analysis, geometrically nonlinear analysis, and measured-imperfection buckling analysis.

These three analysis types were selected to enable direct comparison with collapse loads reported in the literature. Since data were not always available for every method, using multiple analysis routes ensured that at least one verifiable reference existed for each shell. The linear analysis additionally served to confirm that the model was representative in terms of geometry, material properties, and mesh. The MGI primarily assessed whether the DESICOS-based mesh modification, generated from the extracted imperfection plots, was adequate and served as a sanity check of the overall behavior by confirming consistency with the deformation patterns observed in the NASA study. The GNA served as an auxiliary verification method and was used in place of LBA whenever no linear results were reported.

The collapse loads obtained for all shells using these three analysis methods are presented in Table 4.3.

Table 4.3: Buckling load verification for selected test articles. Buckling loads obtained from the NASA SBKF project and corresponding sources are provided in Appendix A.

Structure	**LBA**			**GNA**			**MSI**		
	NASA [N]	This Work [N]	Δ [%]	NASA [N]	This Work [N]	Δ [%]	NASA [N]	This Work [N]	Δ [%]
TA01	3.22×10^6	2.78×10^6	-13.6	3.18×10^6	3.00×10^6	-5.6	2.71×10^6	2.53×10^6	-6.5
TA03	3.24×10^6	2.66×10^6	-17.8	3.51×10^6	2.92×10^6	-16.7	3.28×10^6	2.62×10^6	-20.1
TA07	–	–	–	2.36×10^6	2.83×10^6	20.1	2.46×10^6	2.32×10^6	-5.9
TA09	–	–	–	2.60×10^6	2.46×10^6	-5.4	2.26×10^6	1.99×10^6	-12.3
ETTA1	2.61×10^6	2.49×10^6	-4.5	3.41×10^6	3.43×10^6	0.4	2.37×10^6	2.11×10^6	-10.7

The linear buckling loads generally did not match the values reported in previous studies and, overall, yielded more conservative predictions. The collapse loads obtained from LBA underestimated the buckling capacity by approximately 14–18%, except for ETTA1, where the deviation remained within 5%. For GNA, the accuracy varied more widely, ranging from an underprediction of over 17% for TA03 to an overprediction of roughly 20% for TA07. For MGI, the collapse loads of all segments were underestimated, with deviations ranging from 20.1% to 5.9% for TA07. This behavior may indicate that extracting imperfection values from the published plots inadvertently increased the amplitude of the reconstructed imperfections.

Given these discrepancies, the input parameters used in the structural model—geometry, material properties, and shell section assignments were carefully re-examined. The design parameters were already verified in the previous section, and although some differences in stiffness relative to NASA's models were identified, they were relatively small and not expected to induce deviations of 20% or more in the collapse loads. More interestingly, the greatest deviations occurred for segments whose radius-to-effective-thickness ratios matched the reference data exactly. Furthermore, since the modeled segments were slightly shorter than the original test articles, the collapse loads should, in principle, have been marginally higher—or at least unaffected—across all analysis types, as shell length is known to have a significant influence on buckling behavior [91].

The model parameters matched the grid properties used for the shell verification study, and the weld land dimensions followed the values reported in the respective literature sources. The boundary conditions were reviewed and remained consistent with the definition provided in subsection 3.1.1, with only one unconstrained degree of freedom at the upper remote point. Although the influence of adjacent rig structures in the NASA tests may have been larger than anticipated - potentially contributing to slightly higher buckling loads, the magnitude and inconsistency of the discrepancies observed here are too large to be attributed solely to stiffer boundary regions. Lastly, the mesh was examined. If the meshes used in this work had been too coarse, the linear buckling loads would have been artificially high, not low, thereby eliminating mesh coarseness as a possible explanation.

It should also be noted that some collapse loads used for comparison were not explicitly reported in the SBKF documents and had to be extracted manually from published plots and converted to SI units (the full list of extracted values is provided in Appendix A). This may have introduced minor inaccuracies, but the expected impact is small.

All models were generated using the same script and served as a common baseline for all analysis types. No modifications to structural properties were required beyond mesh generation. The only differences across analyses were the approach-related procedures used. Given that the inconsistencies reached extreme values for some shells—for example, TA07, where deviations ranged from +20.1% to -5.9% — two explanations appear plausible: either the methods reported in the literature were not implemented exactly as described, or the geometric imperfection maps were significantly distorted by the plotting, digitizing, and reprocessing steps used to reconstruct them.

For the former, it was suspected that part of the disparity might be associated with the thickness assignment of the shell element section. As explained in [37, 43], the outer mold line was used to record the imperfections. They defined the reference surface at the inner mold line and offset the thickness outward to obtain the flush OML. Although this approach ensured a smooth external surface, it introduced geometric complexity: every region with a different thickness required a separate shell section, which had to be stitched together with rigid ties - if one looks carefully at Figure 3.3, small gaps between the sections are visible. Consequently, the procedure was computationally expensive due to the contact definitions required at transitions.

To simplify the process, and following the recommendations from [15] for varying-thickness models, the reference surface in this work was set directly on the CAD geometry, eliminating the need for contact-based stitching. Using the top offset definition, the mid-plane of the assigned shell thickness was shifted inward by half the thickness, aligning the mesh with the CAD-defined OML. This strategy was applied consistently across the model, except for the orthogrid stiffeners, which retained a mid-surface definition, as presented in Figure 3.4. However, in ABAQUS (and most commercial FEM software), the default shell section assignment defines the thickness symmetrically about the reference surface (Figure 4.4), effectively placing the reference surface at the mid-plane of the shell. When thickness varies discretely across adjacent regions—such as at the weld land, this produces a stair-step effect on both the internal and external surfaces. In this configuration, the OML is no longer flush and therefore deviates from the test articles' actual geometry.

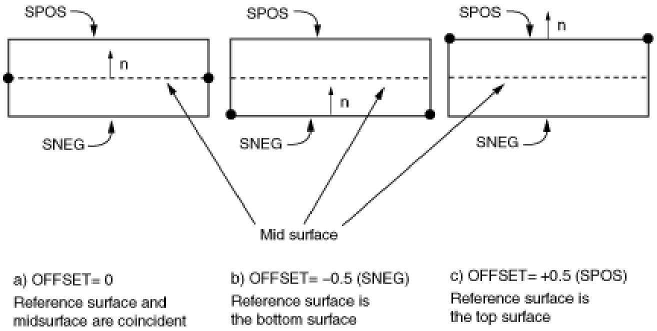

Figure 4.4: The shell thickness assignment offset strategies available in ABAQUS [14]

As explained in [15], all kinematic quantities in ABAQUS are computed with respect to the reference surface. It is further noted that when the reference surface is not coincident with the shell mid-surface, the resulting offset between these two creates a moment arm between the location where the load is applied and the midplane of the shell [16]. This artificial moment arm induces additional bending moments and membrane forces in the shell. As a result, in addition to the prescribed axial displacement (compression), the structure is inadvertently subjected to an outward edge moment, which in turn bends the cylinder further inwards and alters the buckling response. This issue is eliminated only when there is no offset between the reference surface and the midplane of the surface of interest.

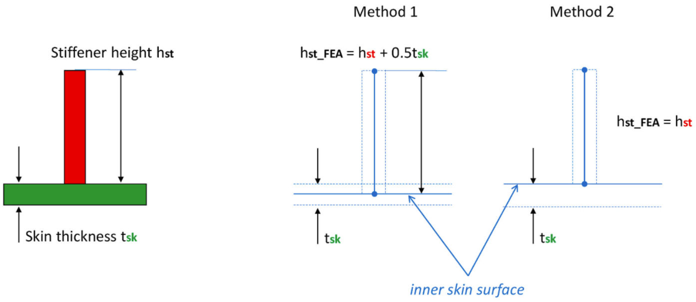

Figure 4.5: Shell modelling strategies employed by Wagner et al. [94].

To assess the influence of this alternative shell-assignment approach, the study by [94] was examined in detail, as it employed yet another modeling strategy based on the IML as the reference surface. The authors proposed two possible strategies for modeling shell thickness in orthogrid-stiffened cylinders. In both cases, the inner mold line radius was used, as illustrated in Figure 4.5. The first strategy adopts a mid-surface definition, extending the stiffeners by half of the acreage skin thickness. The second strategy uses the bottom definition, where the most internal surface serves as the reference surface while keeping the stiffener height unchanged relative to the design specification.

The authors argue that both modeling strategies yield comparable results, with the mid-surface definition being slightly faster to compute and therefore adopted in their study. Their reported buckling loads were very close to those presented in the SBKF reports, and the researchers provided input files upon request. The input file for TA01 was examined carefully to identify another potential source of inconsistency. The geometry in their model differed from that of the SBKF test articles in several respects: no circumferential weld lands were included, the cylinder was slightly longer, and the boundary conditions were set to clamped–clamped. However, the remaining modeling parameters (material properties, shell thicknesses, and mesh density) were similar or identical to those used in this work. Notably, the shell section assignment in their model used the middle offset definition rather than the bottom (IML-based) definition.

Thus, neither modeling strategy yielded a flush outer mold line, contradicting the recommendations of [37]. A second issue arose from the reported radius for TA01, listed as 1219 mm in [35]. In the original document, however, this value corresponds explicitly to the OML radius. Wagner et al. [94] did not specify which inner radius they adopted - this value depends directly on the location of the reference surface. Since the weld lands are significantly thicker than the acreage skin, their inner radii are closer to the cylinder centerline.

Assuming the acreage region was used, the IML radius should be defined as the OML radius minus the acreage thickness (reported as 2.54 mm), giving an IML radius of 1216.46 mm. However, in the provided input file, the measured distance between the central axis and the cylinder surface node was approximately 1219 mm. This indicates that the OML was treated as the IML and used as the reference surface for the middle-plane shell assignment. As a result, the model's outer radius was effectively increased, and the corresponding buckling load rose accordingly. A quick verification showed that adopting a top-offset strategy for GNA (ensuring a flush OML) reduced the collapse load by roughly 10% compared to the mid-surface definition. The baseline model exhibited a linear bifurcation buckling load of approximately 3.41 MN. When the shell assignment was switched to a top-offset definition, the collapse load dropped to 2.99 MN, a 14% reduction. In addition to the lower load, the first buckling mode shifted from a weld-focused pattern to a fully global mode, matching the behavior observed in the model developed in this work.

Based on this observation, an additional test was conducted using an alternative shell section assignment to evaluate the influence of the offset definition within the modeling framework of this work. To accelerate the study, the previous CAD geometry was reused—i.e., the stiffener height was defined initially relative to the OML radius. When the OML is instead treated as the mid-surface radius, this effectively increases the stiffener height and may artificially raise the buckling load. The results obtained using this modified configuration are presented in Table 4.4.

Table 4.4: Buckling load verification for the mid-surface shell offset configuration.

Structure	**LBA**			**GNA**			**MSI**		
	NASA [N]	This Work [N]	Δ [%]	NASA [N]	This Work [N]	Δ [%]	NASA [N]	This Work [N]	Δ [%]
TA01	3.22×10^6	3.29×10^6	0.6	3.18×10^6	3.52×10^6	10.8	2.71×10^6	3.07×10^6	13.6
TA03	3.24×10^6	3.24×10^6	0.0	3.51×10^6	3.21×10^6	−8.6	3.28×10^6	2.79×10^6	−14.9
TA07	-	-	-	2.36×10^6	3.56×10^6	50.9	2.46×10^6	2.96×10^6	20.2
TA09	-	-	-	2.60×10^6	3.22×10^6	23.6	2.26×10^6	2.45×10^6	8.1
ETTA1	2.61×10^6	2.50×10^6	−4.2	3.41×10^6	3.74×10^6	9.5	2.37×10^6	2.25×10^6	−4.8

The accuracy of the results was significantly affected by changes in the offset definition, although the extent of the effect was strongly method-dependent. For the linear buckling analysis, the accuracy improved markedly for the small-diameter shells, with collapse loads nearly matching the SBKF values. ETTA1 exhibited the smallest change among all shells, likely because the thickness offset is negligible relative to its diameter. For LBA, the collapse load became essentially identical to the reference value, whereas GNA overshot the SBKF load by roughly 10%. Interestingly, ETTA1 was also the only case where the MGI analysis improved in accuracy, reducing the deviation to 4.8% compared to SBKF results.

For GNA, all structures except TA03 buckled at higher loads than reported in the literature, and compared to the previous offset definition, the spread in deviations increased. The collapse load of TA07 increased by over 30%, while TA03 buckled at only about 8% below the reference value, compared to almost 17% under the top-offset configuration. The measured-imperfection approach showed behaviour that was equally volatile relative to the top offset definition. Three structures—TA01, TA07, and TA09—shifted from being overly conservative to unconservative, whereas the remaining two improved in accuracy. In particular, ETTA1 deviated by only 4.8%. Nevertheless, TA03 continued to show very conservative behaviour (−15%). Its response can be partially attributed to the estimated imperfection amplitude, as no measurement data were available and the extremities were assumed to lie within ± 0.1 inches.

The pressurized buckling verification was carried out only for ETTA1, as it is the sole structure tested and analyzed under internal pressure during the SBKF programme. However, as explained in [38], the pressurization in the experiment was applied primarily to suppress the influence of manufacturing-induced imperfections, thereby altering the specimen's natural behaviour. The internal pressure effectively pushed the weld land back toward a more circular geometry and constrained the structure to buckle in a specific mode order, aligning the test outcome with the intended objectives. During the campaign, the cylinder was subjected of 1.0 psi (later reduced to 0.6 psi due to the safety concerns [34]), which are not representative of the pressure levels considered in this study, and experienced during the tank operations of 34 psig (≈2.3 bar [12]).
In the available literature, from SBKF, only the measured-imperfection loading curve at 1.0 psi is reported. However, the buckling loads at 1 psi obtained by [76] for SPLA and GNA are available (using identical boundary conditions), together with GNA data obtained by [94]. The results of the verification are presented in Table 4.5.

Table 4.5: Buckling load comparison for ETTA1 at 1 psi.

Test* [N]	**MSI [58] [N]**	**GNA [94] [N]**	**GNA [76] [N]**	**SPLA [76] [N]**	**GNA [N]**	**MSI [N]**	**MSI** [N]**	**SPLAOG [N]**	**SPLA [N]**
3.56×10^6	3.51×10^6	4.12×10^6	4.59×10^6	3.79×10^6	3.81×10^6	3.01×10^6	3.15×10^6	3.67×10^6	3.69×10^6

* Conducted by NASA [34], buckling was not reached.
** Middle shell thickness assignment offset applied.

The obtained collapse load (here computed using the top-offset strategy) deviates substantially from the NASA reference value, with nearly a 15% difference. When the middle-surface definition is applied, the buckling load increases to 3.2 MN, reducing the discrepancy to approximately 10%. As discussed earlier, the source of this mismatch may be linked to incorrectly reported geometry - specifically, a lower actual R/t_{eff} than stated, or to inaccuracies in the extracted imperfection field. In fact, two imperfection maps were identified for this shell: one exhibiting a slightly higher radial disturbance [37], and another with a lower amplitude but more contour levels [58]. To remain conservative, the map with the largest recorded imperfections was used. However, combined with the uncertainty introduced during redigitization, this may have contributed to the overly conservative predictions. Similarly, compared to the values obtained by Wagner et al. [94] and Sim et al. [76], the collapse load obtained is substantially lower, corresponding to a discrepancy of 8% and 20%, respectively. Nevertheless, the two previous works don't agree on the collapse load either, which underlines the dependence on individual research setup - including boundary conditions, meshing, and shell assignment offset strategy. Based on the description of the analysis setup in both works, the former uses a clamped-clamped condition, whereas the latter uses a simply supported condition. This makes the results even more confusing, as the stiffer BC should lead to a higher collapse load, which is not the case. Interestingly, both SPLA variants obtained are nearly identical to the collapse load obtained by Sim et al. [76], despite the significant difference in GNA collapse loads.

Overall, based on the conducted research, three factors appear most likely to have introduced conservatism into the results: the shell offset assignment strategy, geometric variations, and the analysis set-up (particularly the boundary conditions). It is, however, not possible to pinpoint a single dominant cause of the deviations. The observations—where the accuracy improved drastically for LBA or worsened for GNA depending on the offset strategy—indicate that at least some of the reported reference values must be correct. This, in turn, suggests that the offset assignment may have been applied inconsistently in the previous works. The section assignment definition strongly influences the structural response. When combined with other minor geometric and setup differences, it can produce the significant dispersion observed when compared to the SBKF data.

Nevertheless, the intention of this work was not to reproduce the exact structural behavior reported in previous studies, but rather to employ the semi-optimized shell geometries used in past research. The verification primarily served to obtain a rough estimate of the model's accuracy and to assess whether the constructed models behave consistently. For this study, the internal consistency across all modeled structures is far more critical than achieving perfect agreement with historical results. The adopted modeling strategy appears to yield conservative collapse loads for both unpressurized and pressurized cases, although its accuracy at higher internal pressures remains uncertain. The results should therefore be interpreted with some caution. However, the reliability trends identified in this study are not expected to be affected. A more detailed investigation into the root cause of the discrepancies is strongly recommended, but falls outside the scope of the present work.

4.5. Model Sensitivity Study

Due to the project's strict time constraints, no dedicated sensitivity study was conducted to quantify the influence of the modelling assumptions and simplifications. Fortunately, several aspects of these sensitivities have been addressed in past studies, and their findings are briefly summarised in this section. Though it should be noted that these investigations focused exclusively on unpressurised shells, and their validity under combined pressure and axial loading is therefore limited. A dedicated study in a pressurised setting is required to assess their impact on structural behaviour fully.

The most influential assumptions concern the geometry of the analysed shells. The present work adopted the as-designed configuration, removed all fillets, and neglected the tapered ends of stiffeners. On TA07, this assumption had the largest impact on the predicted buckling load from all considered aspects [43]. Using as-built skin and stiffener thicknesses (measured after fabrication and averaged) increased the collapse load by nearly 8%, while the as-built stiffener height contributed an additional 1.1%. Since as-built parameters are only known post-manufacturing, their influence cannot be reasonably predicted.

The effect of stiffener fillets has been studied more extensively. Their inclusion increases the effective skin–stiffener junction stiffness and therefore enhances the axial rigidity [58]. Hilburger et al. [43] proposed a shell-thickness tuning approach was used to correlate a 2D shell model (presented in Figure 4.6) with a full 3D solid model including fillets. The authors reported that fillets increased the effective axial stiffness by less than 1% but increased the buckling load by 4.2%. This study was performed on a representative plate segment with an orthogrid pattern. Nonetheless, a similar value was reported in [69], based on an unpublished NASA document indicating an expected increase of approximately 5%.

The omission of tapered stiffeners was also adopted in past studies, although its effect has not been explicitly quantified [37, 94]. In practice, tapering provides a smoother transition between acreage and weld land regions and may marginally reduce local stress concentrations.

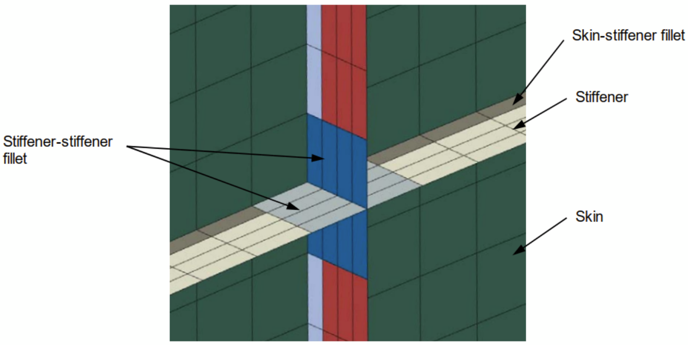

Figure 4.6: Fillet modeling for a shell tank segment [43].

Regarding material behavior, a linear-elastic isotropic model does not fully capture the characteristics of aluminium–lithium alloys. The compressive modulus is slightly higher than the tensile modulus (11.4 Msi vs. 10.8 Msi) [43]. This can be represented by an orthotropic model, where the longitudinal stiffness is taken as the compressive modulus and the circumferential stiffness as the tensile modulus. Such a model increases the global stiffness slightly [58]. Hilburger et al. [43] reported an increase of approximately 1.3% in buckling load when using this improved material model. Conversely, Rudd et al. [69] observed a 1% decrease in collapse load relative to the isotropic case, resulting in better agreement with test results. The authors noted that the benefit is case-dependent, and in some instances, worsened the correlation with strain-gauge measurements. Furthermore, the tank thermal environment effects were neglected after consultation with an ArianeGroup expert. However, aluminum–lithium alloys experience a notable increase in stiffness and strength at cryogenic temperatures—typically on the order of 5–10%, with values depending on the specific temper and temperature range (e.g., liquid oxygen or liquid hydrogen conditions). Such stiffening would increase the collapse load and enable higher allowable pressurization. Thus, it is highly recommended to revisit this assumption in future research.

Lastly, the weld land material was assumed to be unaffected by the friction-stir-welding process [94]. In reality, the weld zone exhibits a different microstructure and reduced elastic modulus. Its inclusion could modify the load attraction in the weld region and potentially increase the collapse load. However, based on available evidence, this effect is not expected to be significant.

Collapse Dependence on the Displacement Magnitude

During the verification runs, an unexpected sensitivity was observed: the predicted collapse load depended on the magnitude of the imposed axial displacement. Initially, all shells were subjected to an identical end-shortening of 0.03 m. However, at 4 bar, both ETTA1 and TA03 remained stable and did not buckle, which required increasing the imposed displacement to 0.08 m. As a consistency check, the same displacement was applied to TA01 to assess the assumed independence of the structural response from the prescribed compression level. This assumption was found to be invalid.

This displacement dependence was observed in both static and dynamic implicit analyses. To ensure consistent comparison across all configurations, all verification analyses were therefore re-run using the higher end-shortening.

The origin of this discrepancy appears to stem from the increment-selection procedure in nonlinear analysis. At higher imposed loads, the solver typically reduces the time increment to satisfy convergence criteria, which results in more frequent stiffness updates and improved tracking of local stiffness changes. This behavior is evident when modifying the displacement in the input file of Wagner et al. [94]. Increasing the prescribed displacement from 0.006 m to 0.01 m (no pressure) produces the curves shown in Figure 4.7.

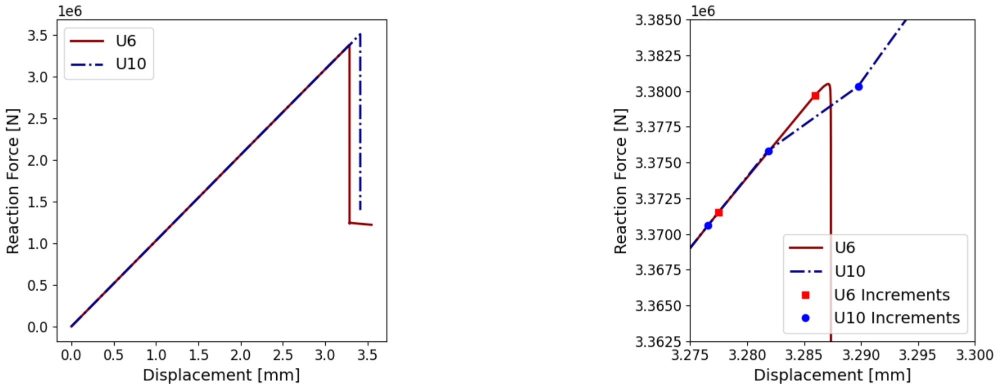

Figure 4.7: Load–displacement curves for TA01 GNA input file from [94], with vertical displacements of 0.006 and 0.01 m.

From the zoomed view, it is evident that the lower imposed displacement (U6) bypasses a local bifurcation point and therefore follows a different equilibrium path, yielding a lower collapse load. Although both analyses share an increment in which displacement and reaction force nearly match immediately before the bifurcation, their gradients differ slightly, implying a small local stiffness mismatch. The U6 case exhibits marginally higher stiffness, and the solver accepts a larger increment that still meets the default convergence tolerance of 0.5%. This larger step skips the bifurcation, resulting in a predicted collapse load of 3.38 MN (higher than the 3.29 MN reported in the reference study). In contrast, the higher imposed displacement continues to follow the post-local-buckling response and reaches a load of 3.51 MN.

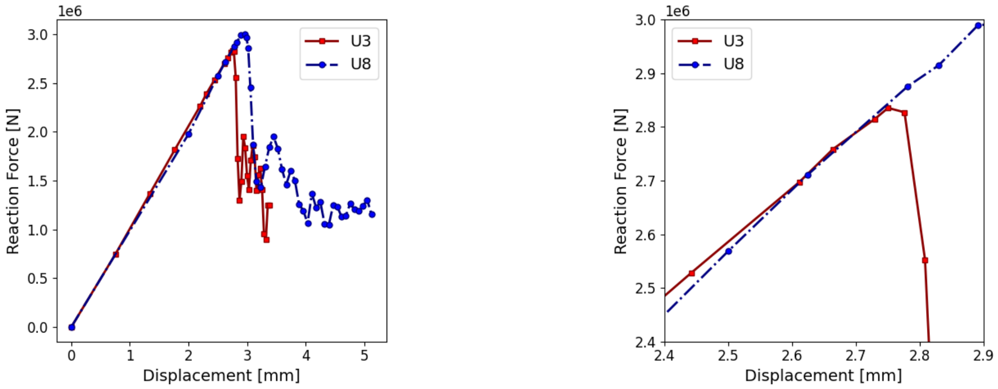

Figure 4.8: Load–displacement curves for TA01 GNA with dynamic implicit analysis and vertical displacements of 0.03 and 0.08 m.

A similar tendency is observed in the dynamic implicit analyses (Figure 4.8), though the responses contain more local fluctuations. When zoomed near the U3 buckling region, the local gradient decreases and the stiffness drops, after which the solution diverges onto a different equilibrium branch. The resulting collapse load is 2.84 MN, compared to 3.0 MN for the higher displacement.

However, this trend is not uniform across all structures. In several cases the higher prescribed displacement leads to lower collapse loads, whereas in others the opposite occurs, as shown in Table 4.6. This indicates that the phenomenon is configuration-dependent and not monotonically related to the imposed end-shortening.

Table 4.6: Comparison of NASA GNA predictions with U3 and U8 results from dynamic implicit analysis.

Structure	NASA GNA [N]	U3 GNA [N]	ΔU3 [%]	U8 GNA [N]	ΔU8 [%]
TA01	3.18×10^6	2.84×10^6	−10.8	3.00×10^6	−5.6
TA03	3.51×10^6	2.75×10^6	−21.4	2.92×10^6	−1.7
TA07	2.49×10^6	3.07×10^6	23.4	2.83×10^6	1.4
TA09	2.60×10^6	2.64×10^6	1.6	2.46×10^6	−5.4
ETTA1	3.41×10^6	3.00×10^6	−12.0	3.43×10^6	4.0

For consistency across the present study, an imposed displacement of 0.08 m was adopted for all structures and pressure levels in both static and dynamic analyses. Nevertheless, this numerical sensitivity warrants further investigation. The behavior appears largely independent of boundary conditions or analysis type, and is more plausibly associated with increment selection and stiffness-update frequency in the nonlinear solver. It is currently unclear whether a displacement threshold exists beyond which the effect diminishes. Until the mechanism is fully characterized and mitigated, caution is advised when interpreting collapse loads obtained from displacement-controlled nonlinear analyses.

5

Results and Discussion

In this chapter, the buckling analysis results are presented. The behavior of the convergence-based approaches: SPLA, MPLA, and DFPA, is first examined in section 5.1. The broader collapse trends across all structures and pressures are discussed in section 5.2. The reliability study follows in section 5.3, where the coefficient of variation, Kendall's W, and the intraclass correlation coefficient are evaluated. Finally, the key observations are synthesized and interpreted in section 5.4.

5.1. Convergence Results

Before analyzing the obtained collapse loads, the convergence behavior of three perturbation-based methods (SPLA, MPLA, and DFPA) was examined. As established in the literature, these approaches are expected to reach a semi-stable collapse-load plateau at sufficiently large perturbation magnitudes. To identify such plateaus, a curve-fitting procedure was applied to generate trendlines, combined with a basic convergence criterion.

In principle, for most structures, the curve-fitting methodology reproduced the response to increasing perturbation magnitudes accurately, as reflected by the high coefficients of determination - all the plots are presented in Appendix C. The associated three-sigma (99.7%) confidence intervals were generally narrow. These intervals were obtained from the parameter covariance matrix returned by curve_fit, where each diagonal entry represents the variance of the corresponding buckling-load parameter. The confidence bounds were then evaluated as three-sigma limits. In several cases, however, the intervals widened substantially because the covariance matrix grew in magnitude or became nearly singular. This occurred when the fitted curve had already flattened near its asymptote, and the parameters became weakly identifiable, or when strong parameter coupling led to multiple near-equivalent solutions. In such cases, tightening the fitting bounds or reducing the number of free parameters reduced the covariance matrix and yielded noticeably narrower confidence intervals.

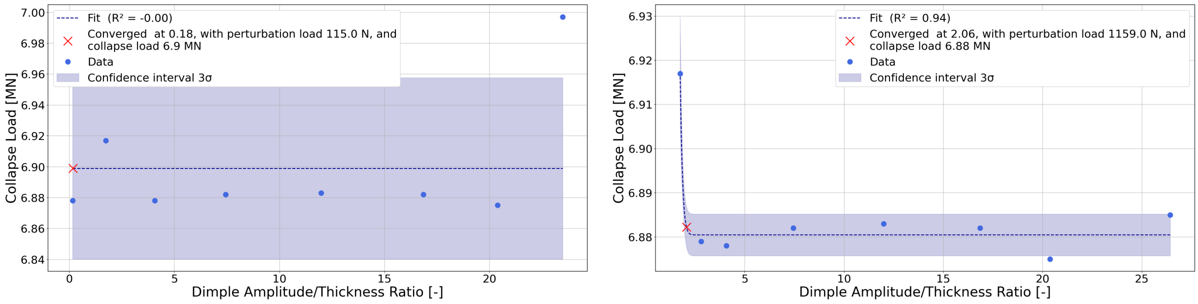

(a) Original convergence plot.

(b) Modified convergence plot.

Figure 5.1: Comparison of convergence behavior of ETTA1 MPLA at 2 bar.

Nonetheless, some approach–pressure combinations did not exhibit the expected convergence behavior. The most prominent example was ETTA1 under the MPLA at 2 bar, where the response was so irregular that selected perturbation loads had to be removed or replaced (100 N, 6000 N removed and 1500 N, 8000 N added) to obtain a physically meaningful trendline and a reasonable converged perturbation magnitude as presented in Figure 5.1.

Furthermore, for the TA03 SPLA analysis, the structure exhibited highly irregular behavior: the collapse load varied noticeably with increasing perturbation magnitude, and at several higher perturbation levels, the cylinder buckled at higher loads than at lower perturbations. This behavior was also observed at 2 bar, with only the 4 bar case stabilizing the response into a trend more consistent with the expected theoretical behavior. A comparison between the unpressurized and 4 bar responses is shown in Figure 5.2.

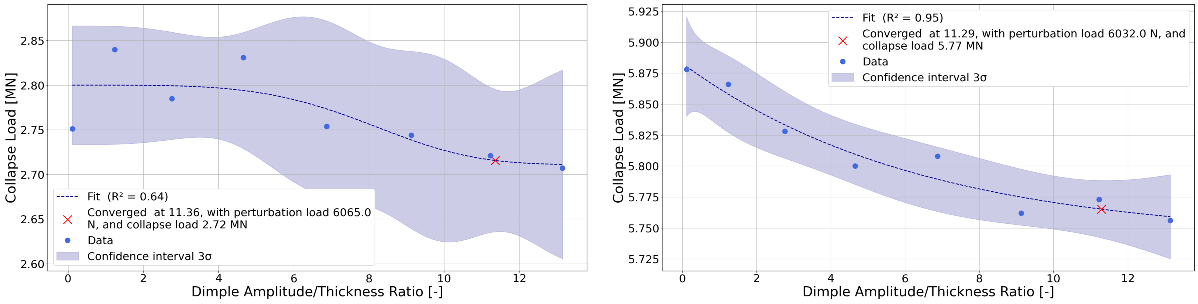

(a) Convergence plot at 0 bar.

(b) Convergence plot at 4 bar.

Figure 5.2: Comparison of SPLA convergence behavior for TA03 across pressure levels.

The simplest explanation for this inconsistent behavior would be an error in the load application. However, the same setup script was used for all shells — including those exhibiting ideal convergence, and a direct inspection of the input files confirmed that the load definition was correct. The observed "outlier" type responses are more plausibly linked to a slight shift in the active buckling mode at specific perturbation magnitudes. This phenomenon was also observed in shells with otherwise well-defined convergence behavior, such as TA07 in the SPLA analysis (Figure 5.3), where the collapse load at P=3000 N exceeded that at P=2000 N, placing the point outside the confidence interval. Once again, inspection of the underlying model did not reveal any errors, and the only difference between the input files for these two runs was the magnitude of the perturbation.

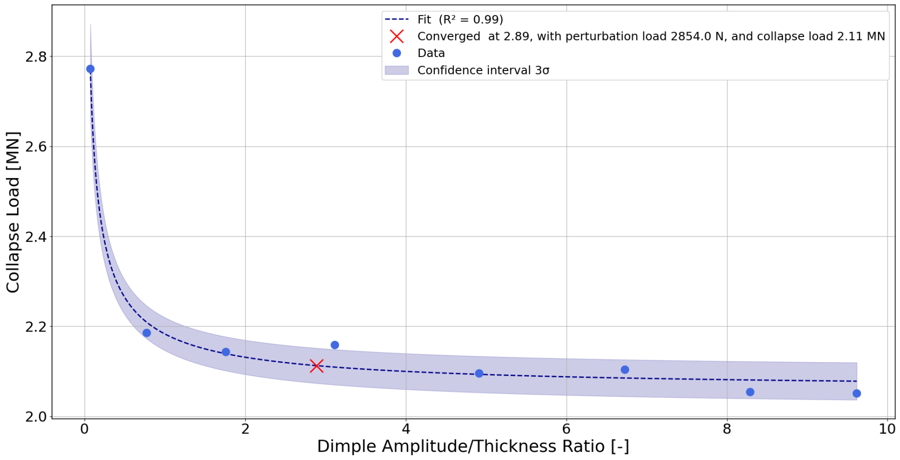

Figure 5.3: TA07 SPLA convergence study with visible perturabtion outlier.

The pressure effect on the structural response also influenced convergence behavior, occasionally producing counterintuitive results in which the converged perturbation magnitude was lower than in the unpressurized baseline. This anomaly, despite the expectation that higher pressures should require larger imperfection magnitudes, appears to stem from the stabilizing effect of internal pressure on the shell, which suppresses sensitivity to local perturbations. It is also possible that the current convergence criterion of 5% is too lenient, allowing these shifts in the fitted asymptote to appear as converged behavior.

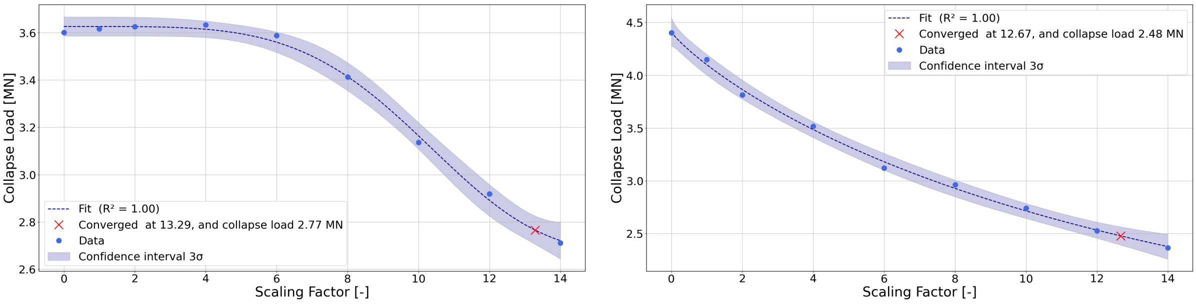

(a) Convergence of TA01 DFPA at 4 bar.

(b) Convergence of TA09 DFPA at 4 bar.

Figure 5.4: Comparison of convergence behavior between structures.

For DFPA, the proposed stretched exponential fit captured the response particularly well, yielding smaller confidence intervals than the SPLA/MPLA counterparts and consistently very high R^2 values. Notably, the convergence checks were performed on the compressive load bump magnitude, not the displacement response - like in SPLA/MPLA approaches, and in several cases, the inspected load range for the bump magnitude was insufficient to reach a true asymptote. At the same time, DFPA remained the most conservative approach, systematically producing the lowest collapse loads. Extending the bump-magnitude range could, in principle, improve convergence, but it would also push the predicted buckling performance even lower. This trend was especially pronounced at higher pressures. Although increasing the upper bound (e.g., to 14 or 16) initially appeared to be a remedy, additional tests showed a continued degradation in the predicted collapse load. Representative examples of this behavior are shown in Figure 5.4.

Table 5.1: Comparison of converged and check loads for SPLA, MPLA, and DFPA across ETTA1 and TA01.

			ETTA1 – 0 bar					
$N_{\text{SPLA},P=4665}$ [N]	N_{Check} [N]	Δ [%]	$N_{\text{MPLA},P=4961}$ [N]	N_{Check} [N]	Δ [%]	$N_{\text{DFPA},P=12.7}$ [N]	N_{Check} [N]	Δ [%]
3.11×10^6	2.97×10^6	4.7	1.46×10^6	1.52×10^6	−3.9	1.90×10^6	1.82×10^6	4.2
			ETTA1 – 0.06895 bar					
$N_{\text{SPLA},P=2211}$ [N]	N_{Check} [N]	Δ [%]	$N_{\text{MPLA},P=3918}$ [N]	N_{Check} [N]	Δ [%]	$N_{\text{DFPA},P=11.81}$ [N]	N_{Check} [N]	Δ [%]
3.69×10^6	3.67×10^6	0.6	2.65×10^6	2.72×10^6	−2.4	2.48×10^6	2.54×10^6	−2.4
			ETTA1 – 2 bar					
$N_{\text{SPLA},P=1962}$ [N]	N_{Check} [N]	Δ [%]	$N_{\text{MPLA},P=1159}$ [N]	N_{Check} [N]	Δ [%]	$N_{\text{DFPA},P=12.71}$ [N]	N_{Check} [N]	Δ [%]
6.88×10^6	6.89×10^6	0.3	6.88×10^6	6.98×10^6	1.4	4.56×10^6	4.58×10^6	−0.3
			TA01 – 0 bar					
$N_{\text{SPLA},P=2338}$ [N]	N_{Check} [N]	Δ [%]	$N_{\text{MPLA},P=3173}$ [N]	N_{Check} [N]	Δ [%]	$N_{\text{DFPA},P=12.53}$ [N]	N_{Check} [N]	Δ [%]
2.02×10^6	2.03×10^6	−0.5	1.52×10^6	1.56×10^6	−2.5	1.47×10^6	1.49×10^6	−1.4
			TA01 – 2 bar					
$N_{\text{SPLA},P=2243}$ [N]	N_{Check} [N]	Δ [%]	$N_{\text{MPLA},P=5977}$ [N]	N_{Check} [N]	Δ [%]	$N_{\text{DFPA},P=13.24}$ [N]	N_{Check} [N]	Δ [%]
3.30×10^6	3.32×10^6	0.5	2.83×10^6	2.82×10^6	−0.3	2.42×10^6	2.43×10^6	0.4
			TA01 – 4 bar					
$N_{\text{SPLA},P=3594}$ [N]	N_{Check} [N]	Δ [%]	$N_{\text{MPLA},P=5128}$ [N]	N_{Check} [N]	Δ [%]	$N_{\text{DFPA},P=13.29}$ [N]	N_{Check} [N]	Δ [%]
3.67×10^6	3.67×10^6	0.2	3.34×10^6	3.38×10^6	1.0	2.77×10^6	2.70×10^6	−2.4

Nevertheless, the very high R^2 values may appear indicative of overfitting — typically arising when too many model parameters are fitted relative to the number of data points. However, two points mitigate this concern. First, the trend line is obtained using non-linear least-squares optimization [71], which by design does not inflate the coefficient of determination. Second, the fit accuracy can be directly verified by running simulations at the converged perturbation magnitude. This check was performed for ETTA1 and TA01, with results shown in Table 5.1. The fitted collapse loads closely match the actual simulation values, with deviations of approximately −4% to +5%. This confirms that the high R^2 values reflect genuine predictive accuracy rather than overfitting.

Overall, the examples presented here are intended to highlight the absence of fully systematic convergence behavior across all structures. For brevity, not every deviation is discussed in detail, but the illustrated phenomena should be kept in mind when interpreting the reliability results.

5.2. General Buckling Behavior

A summary of the collapse loads obtained for all considered shells, pressure levels, and imperfection-modeling approaches is presented in Figure 5.5. In addition to the nonlinear analysis results, collapse-load estimates based on the knockdown factors provided in SP-8007 [87] and those derived within the SBKF project [37] are included to illustrate the level of conservatism inherent to current design practices. The derivation of the applied knockdown factors is detailed in Appendix D. As observed, the KDF-based predictions are indeed highly conservative compared to the majority of nonlinear imperfection-modeling approaches. Although the new KDF formulation provided higher estimates compared to the SP-8007 monograph, it is very limited in scope for pressurized structures. The buckling curves are provided only for up to 10 psi (0.6895 bar), and thus, it was solely applied for the ETTA1 - 1 psi case. The KDF in the new SBKF are significancy improved compared to the traditionally used SP-8007 ones. For TA03, TA07, and TA09, the KDF estimates exceed the collapse loads predicted by the DFPA methods, suggesting that these non-traditional imperfection-modeling approaches may lead to very conservative or inaccurate predictions for certain configurations.

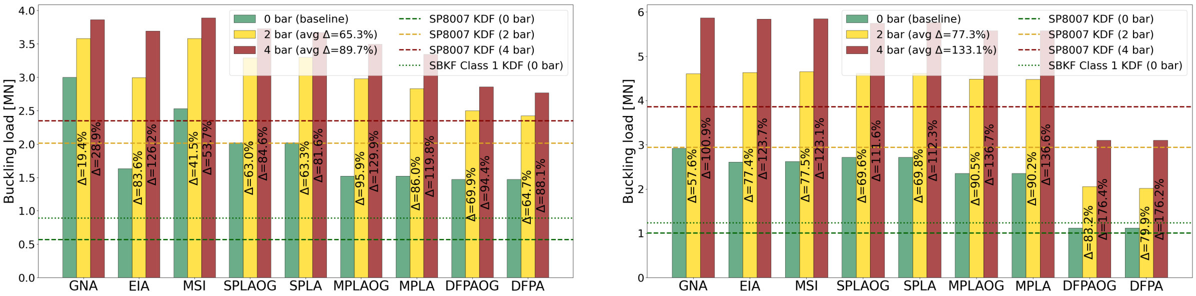

(a) Buckling loads of TA01.

(b) Buckling loads of TA03.

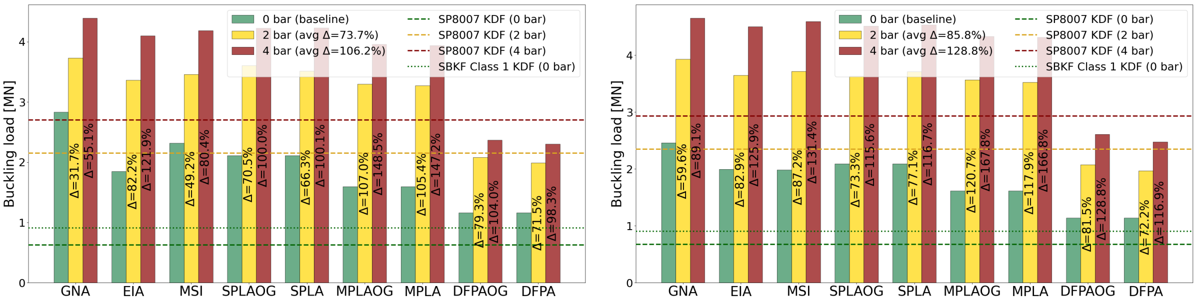

(c) Buckling loads of TA07.

(d) Buckling loads of TA09.

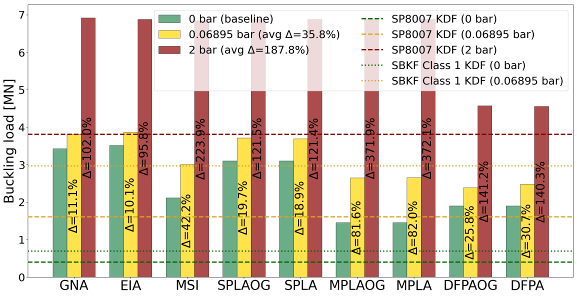

(e) Buckling loads of ETTA1.

Figure 5.5: Buckling loads of all structures, across three pressure regimes obtained in the study.

Overall, and in agreement with previous studies, increasing internal pressure consistently raises the buckling load of the structures, irrespective of the modeling approach. However, the magnitude of this stabilizing effect

varies substantially between shells and imperfection-modeling methods, underscoring the strong configuration and approach dependence of pressurized buckling predictions.
To establish a baseline, the geometric nonlinear analysis was examined first, as it reflects the behavior of the geometrically perfect shells. ETTA1 showed the largest relative improvement, with a 102% increase at 2 bar compared to the unpressurized case, and already at 0.06895 bar, the load increased by 11%. For 2.4 meter in diameter shells, the improvement at 2 bar ranged from 19.4% for TA01 to 60% for TA09. This disparity is peculiar given that all test articles share the same diameter, but upon closer inspection TA01 has nearly twice the slenderness (expressed in R/t_{eff}) of TA09. Despite the former having a thicker skin of 2.54 mm (vs. 1.73 mm), the latter has a much denser grid pattern.

At 4 bar, the trend shifts slightly - TA01 again shows the smallest increase (29%), whereas TA03 reaches 101%, followed by TA09 at 89%. The inconsistent performance between the shells suggests that pressure sensitivity is strongly linked to their designed buckling behaviour. As discussed in [35], the test articles were intentionally designed to trigger different governing buckling modes. Both TA01 and TA03 were intended to exhibit global buckling prior to the onset of local modes or yielding. Moreover, TA03 was derived from a scaled Ares I core-stage tank segment with built-in axial load relief and hoop-stiffening effects from internal pressure, and was used to validate FEM predictions of weld land buckling. Finally, although the longitudinal weld geometries were broadly similar, the transition-region width differed noticeably between shells. Combined with the varying acreage stiffness and grid pattern, makes it difficult to attribute the observed performance increase to a single structural feature.

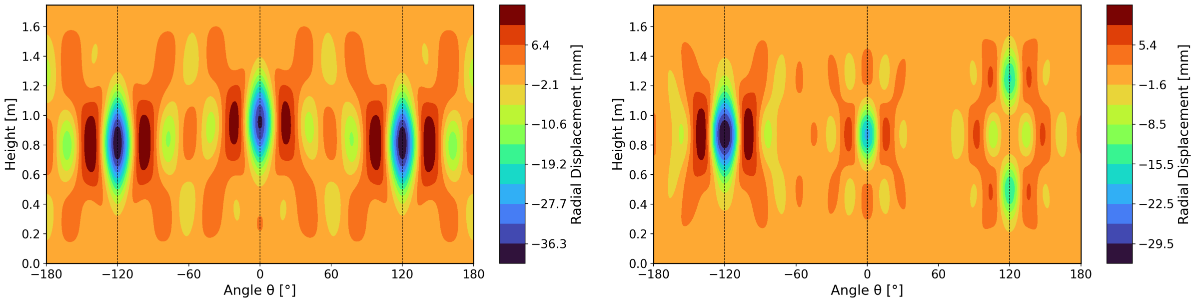

(a) Shells buckling load at 0 bar.

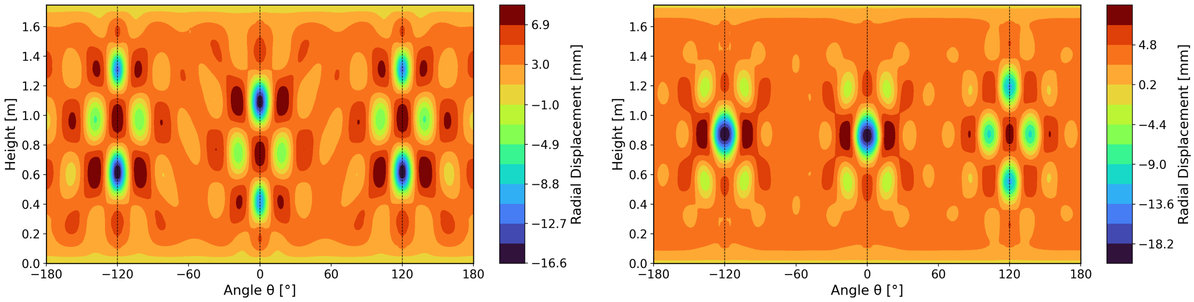

(b) Shells buckling load at 2 bar.

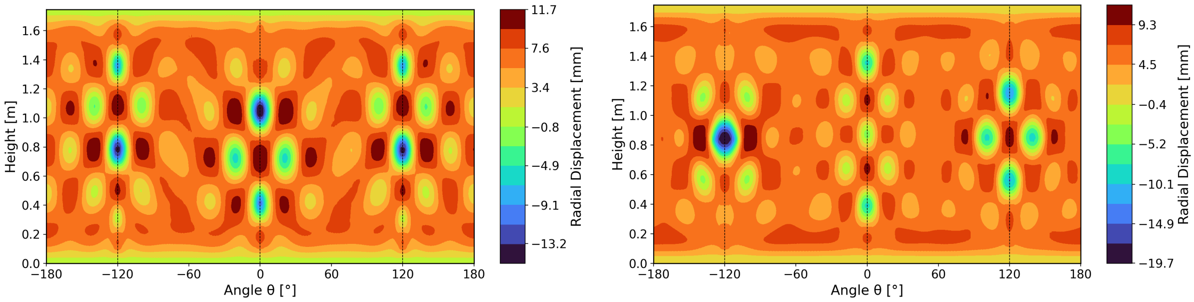

(c) Shells buckling load at 4 bar.

Figure 5.6: Effect of internal pressure on the EIA buckling mode of TA03 (left) and TA09 (right).

When non-geometrically perfect imperfection modeling strategies are applied, the absolute buckling-load behavior becomes even more volatile across the barrel segments. The data clearly indicate that the largest increase between the unpressurized state and 2 bar occurs for MPLA. For the smaller shells, the increase ranges from 86% to 118%, and reaches a remarkable 371% for ETTA1. The MPLAOG variant behaves almost identically, with nearly the same percentage increases. This suggests that MPLA, where loads are introduced at every weld line, may be overly conservative in the unpressurized case and significantly amplified by internal pressure. The perturbation load at which the collapse load converges is lower than in the single-load SPLA case, as the extent of the stiffness degradation is greater. However, as visible in Figure 5.7, it still nucleates from a single dimple. In theory, as the buckling load of both should be the same, the resulting dimples are therefore shallower, and at higher pressures are bulged out to a greater degree, contributing to the observed large increases in collapse load. The greater the number of perturbation locations, the more the dimple depth is reduced—explaining the extreme increase observed for ETTA1 when eight perturbation loads were used, and thus recorded the greatest increase in buckling load at 2 bar - 372%.

For SPLA, the collapse load increases from 82% for TA01 at 4 bar to over 114% for TA09, with the highest increase again observed for ETTA1 (121.4%). The SPLA variant using unpressurized converged perturbation loads shows a comparable trend. Overall, the SPLA and MPLA convergence approaches yield broadly similar results, aside from a few notable deviations. These discrepancies are likely tied to the convergence calculation itself and the shell-dependent buckling response mechanisms discussed in section 5.1.

Another noteworthy observation is made for the eigenmode imperfection approach, where the performance increase remains within a narrow range: 77–88% at 2 bar, and 122% (TA07) to 126% (TA01) at 4 bar for all small-diameter test articles. In contrast, the Space Shuttle external tank shows the lowest increase among the considered shells, reaching only 95.8% at the highest pressure level.
The near-consistent behavior of the small-diameter shells can be linked to their buckling mode patterns. Unlike ETTA1, these cylinders always buckle in the first linear global mode - characterized by a couple of deep dents. Consequently, the eigenmodes imperfections remain highly similar across pressure, because the pressure linearly bulged them out as illustrated in Figure 5.6. This uniformity in the imposed imperfection shape naturally limits the variation in pressure-induced performance gains. The small discrepancy, mostly stems from different initial imperfection magnitude as for certain shells the first linear mode indicated deeper grooves. Though it is

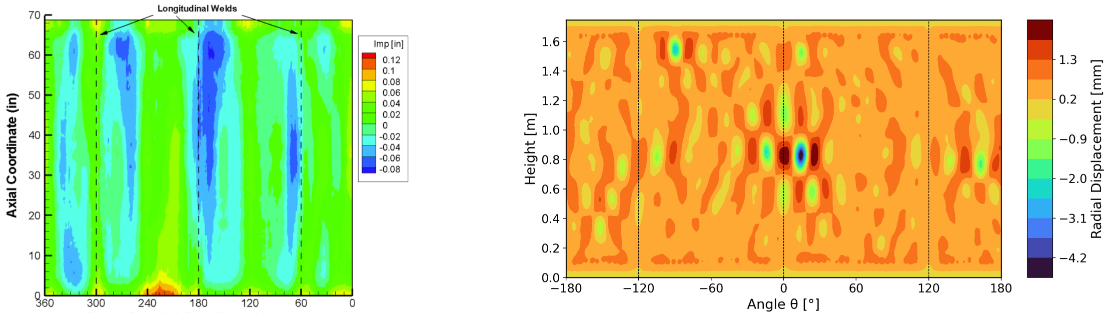

(a) Measured radial imperfections of TA01[83], with a corresponding buckling mode

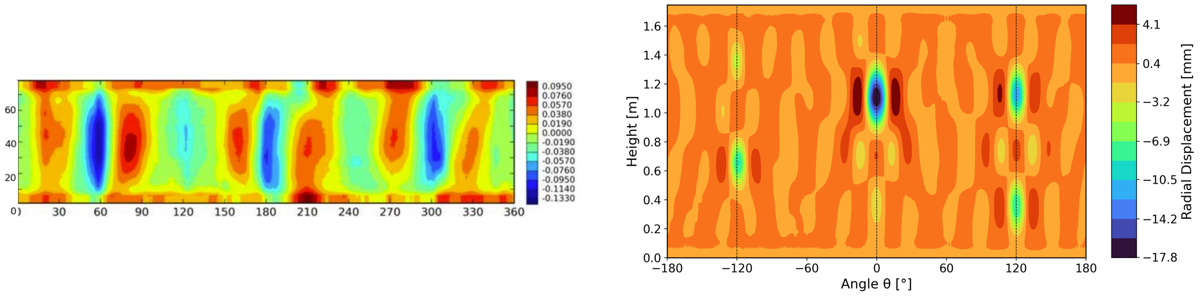

(b) Measured radial imperfections of TA09 [69], with a corresponding buckling mode.

Figure 5.7: Comparison of imperfection signatures of TA01 and TA09, with their resulting bucklign modes.

plausible that using the acreage skin thickness which is with 1 mm for the small shells, instead of the $t_{\text{effective}}$ (which accounts for the added grid stiffness) sets the eigenmode imperfection amplitude to comparable levels, further reducing the pressure effect.

The lowest collapse-load improvements (excluding ETTA1) were obtained for the measured-imperfection approach, ranging from 41.5–87.2% at 2 bar and 53.7–131.4% at 4 bar. The lowest gains correspond to TA01, while the highest are observed for TA09. This highlights that similarity in imperfection shape is not the only driver - the magnitude of the measured field plays an equally strong, if not more substantial, role in the structural response. Notably, the imperfection signature of TA01 is unique in that its dominant disturbance is not centered on the welds, unlike TA09, which is reflected in their respective buckling modes (Figure 5.7) - further explaining the reduced sensitivity to pressurization.

When the percentage improvement between consecutive pressure levels is examined, the variation in buckling load becomes far less pronounced. For the 8-ft test articles, most methods fall within a 20–30% increase, with the exception of TA01, where GNA and MGI show only about an 8% gain. This behavior suggests that the pressure-dependent performance increase reaches a practical upper limit, set by the interaction between structural configuration and imperfection modeling, as foreseen in small-scale pressurized buckling experiments [77]. The results for ETTA1 reinforce this interpretation: even at only 1 psi the structure exhibited more than a 10% improvement across the approaches.

5.2.1. Normalized Buckling Trends

Knowing the general trends, the interquartile range of the normalized buckling data was evaluated. A wide spread is immediately apparent across methods and structures, ranging from 1.60 for GNA to only 0.53 for DFPA for the unpressurized case presented in Figure 5.8. Both perturbation-based approaches—DFPA and MPLA, predict lower collapse loads on average compared to the remaining methods. However, DFPA, with a mean normalized value of 0.69, also exhibits the smallest spread (≈0.25), confirming its highly conservative but internally consistent behavior. A notable outlier is the MPLA result for ETTA1, which, combined with the exceptionally large non-normalized performance increase, indicates that applying perturbation loads at every weld land becomes overly conservative when the number of welds exceeds three.

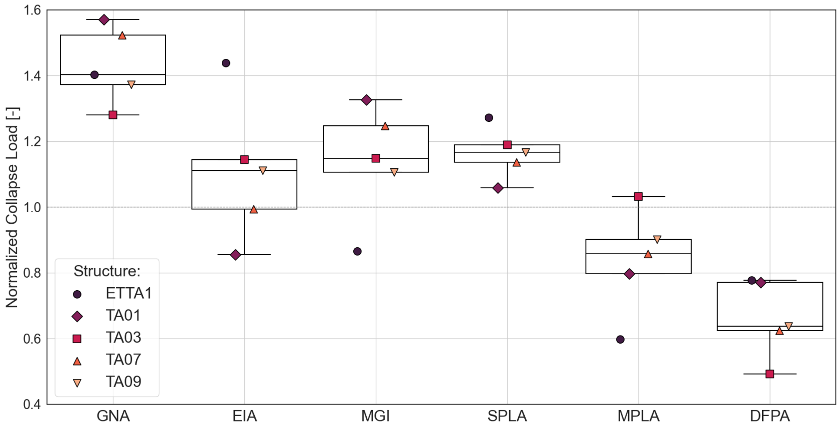

Figure 5.8: Normalized buckling loads of all shells at an internal pressure of 0 bar.

In contrast, the most extensive spread is observed for the measured imperfections approach. Despite identical manufacturing conditions, imperfection fields vary significantly across the shells, and this variability directly affects buckling performance. As expected, TA01 (the only shell with additional reinforcement near the weld land) shows the most favorable response within this method.

For the pressurized cases, the overall trends change markedly. The ranges of the normalized buckling loads, both per method and across methods, for each structure are significantly smaller than those in the unpressurized baseline. Consequently, the spread in mean normalized collapse loads contracts for all approaches except DFPA, which retains a wider range due to its inherent conservatism.

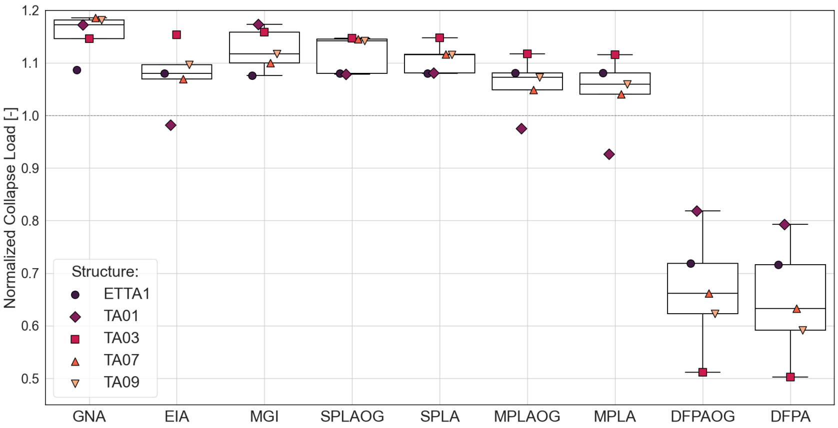

Figure 5.9: Normalized buckling loads of all shells at an internal pressure of 2 bar.

At 2 bar, the variation in mean values across methods is small, with a difference of only about 12% between the most conservative (GNA) and MPLA. At this pressure level, the MGI, SPLAOG, and SPLA approaches produce similar means and ranges, although the ordering of structures differs. The lowest spread is observed for the eigenmode-based method. However, this result is statistically fragile because two of the five structures (TA03 and TA09) are flagged as outliers, reducing the number of reliable data points.

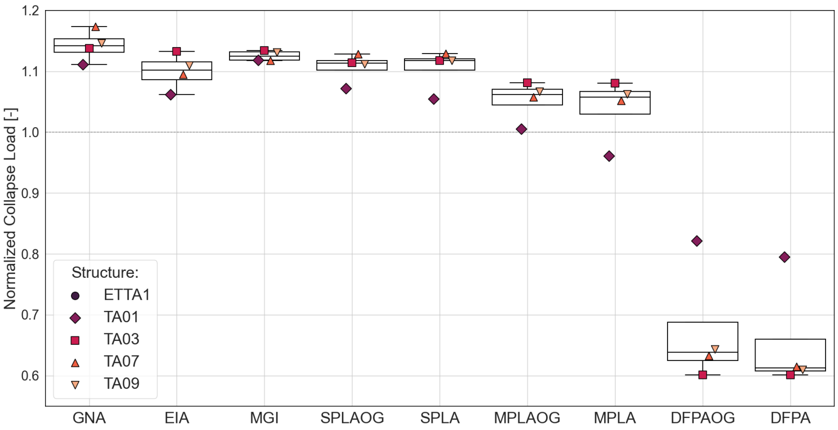

Figure 5.10: Normalized buckling loads of all shells at an internal pressure of 4 bar.

Another notable observation concerns the relative positions of the individual structures. Unlike the unpressurized baseline - where several shells had at least one method producing the highest buckling load, once the pressure is applied, TA03 becomes the top-performing structure for nearly all approaches (except for the load-induced imperfection methods), which is expected as it is the shell with the lowest slenderness. As a result, the average collapse load increase shifts in its favor, and thus the most conservative DFPA predicts even lower normalized performance for TA03 than at 0 bar.

The spreads for TA03 and ETTA1 are also the most consistent across the methods. This aligns with earlier observations: these two structures are the most strongly influenced by internal pressurization, which suppresses method-dependent variability and drives the results toward a common pressure-dominated response. The case of ETTA1 is particularly odd. Its normalized load variability remains below 26%, and when DFPA is excluded, the difference between approaches becomes nearly constant, with a spread of approximately 0.4% - which is clearly visible on Figure 5.5. To understand this behavior, the buckling patterns for the methods (except for those using the unpressurized baseline converge perturbation) were plotted and are shown in Figure 5.11.

It becomes clear that the methods yield nearly identical collapse loads because they trigger almost identical buckling patterns. While small-amplitude half-waves appear at each weld line, the response is dominated by two half-waves spanning the entire circumference of the segment — a shallower one near the top and a much deeper one at the base. This behavior corresponds to the well-known elephant-foot buckling mode, named for its visual resemblance to an elephant's foot Figure 5.12.

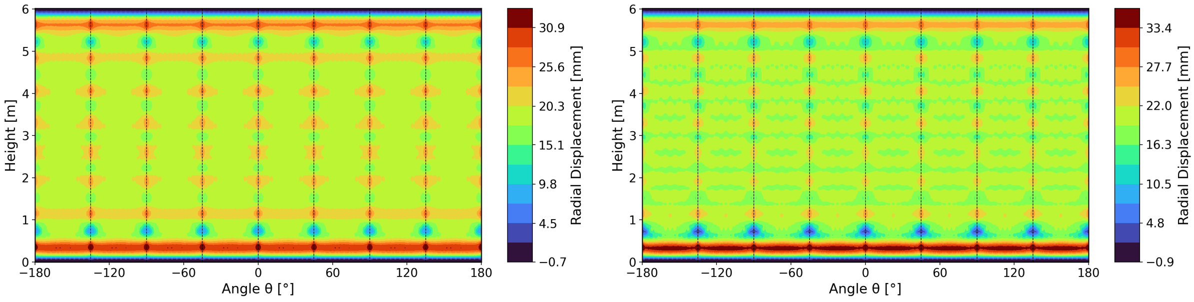

(a) GNA at 2 bar

(b) EIA at 2 bar

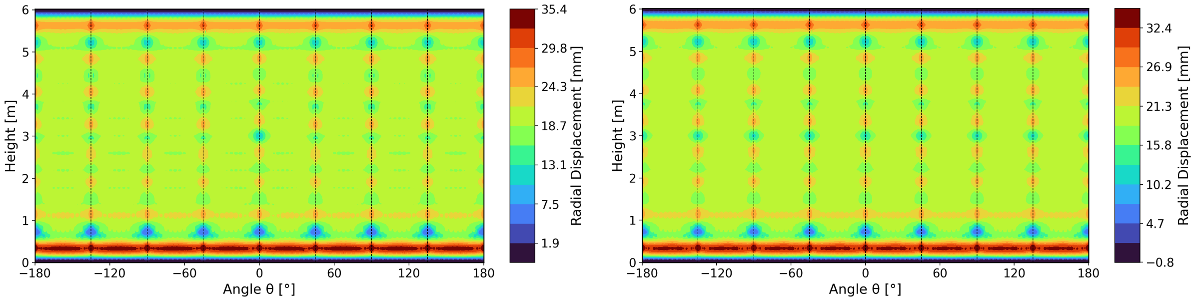

(c) SPLA with P=1962 N at 2 bar

(d) MPLA with P=1159 N at 2 bar

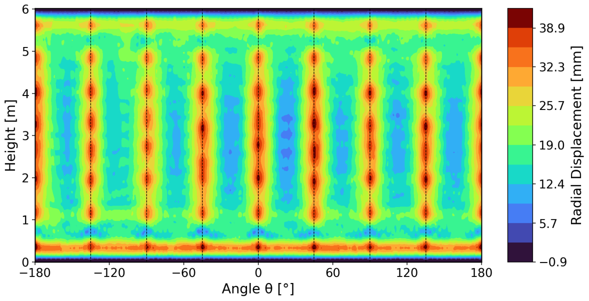

(e) MSI at 2 bar

Figure 5.11: ETTA1 buckling modes at 2 bar pressure.

(a) Elephant foot [48].

(b) Elephant foot buckling on a steel tank[59].

Figure 5.12: Visualization of elephant-foot buckling.

As described by Rotter [68], elephant-foot buckling occurs in shells with high radius-to-thickness ratios (typically above 250) and is driven by the increase in bending stresses near the base under internal pressure. In this region, the tensile circumferential stresses dominate over the relatively low axial compressive stresses, producing the characteristic plastically bulged deformation. At lower pressurization levels, however, the response remains more elastic, and the buckling pattern resembles the unpressurized mode - consistent with the behavior observed in this study at 0.06895 bar.

For TA03, the larger spread between methods is likely linked to the absence of this pressure-dominated buckling regime. Its slenderness is insufficient to trigger an elephant-foot mode ($R/t_{\text{eff}} = 80.1$), and the resulting buckling shapes, as shown, do not converge toward a single dominant feature.

At 4 bar, the trends from 2 bar persist, as illustrated in Figure 5.10. The spread across methods decreases further, including for DFPA, which contracts to only 0.05. The lowest spreads are again observed for the MGI and SPLA variants. It can be partly attributed to the relatively small imperfection amplitudes they introduce, which already yield the highest accuracy in the unpressurized baseline. Under internal pressure, these shallow dents are effectively bulged out, pushing the response closer to that of a near-perfect cylinder and reducing variability across methods. However, this explanation raises the question of why the geometrically perfect GNA (nominally the true baseline) exhibits a wider spread. This can be rationalized by the fact that a perfect structure buckles in a near symmetric manner governed by the orthogrid pattern. This dependence causes the buckling response to diverge more noticeably between cylinders.

The larger range observed for the eigenmode approach follows similar logic, but is dependent on the magnitude instead. As proved, the smaller shells exhibit similar buckling patterns at high pressures, but the radial displacement varies significantly. The initial imperfection pattern is a result of both the first mode shape and the thickness magnitude. Even though the modes look similar - Figure 5.13, the depths of the introduced imperfections from the linear buckling analysis vary significantly, leading to a large discrepancy in the collapse values. Combined with the method's inherently conservative nature, this results in a broader spread of normalized collapse loads.

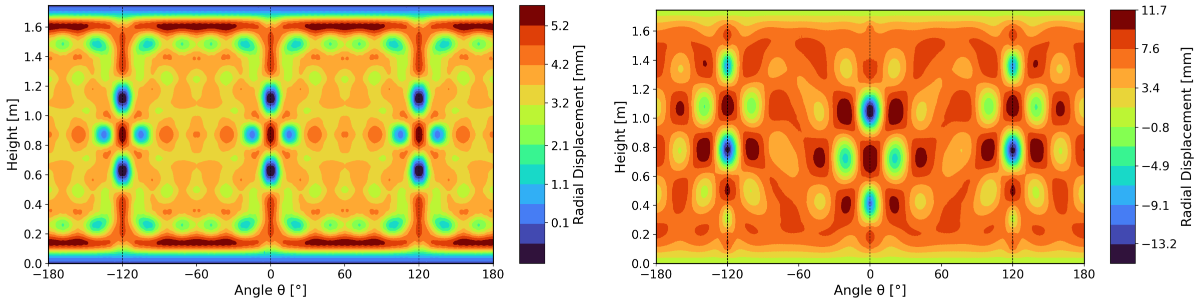

(a) TA01 buckling pattern.

(b) TA03 buckling pattern.

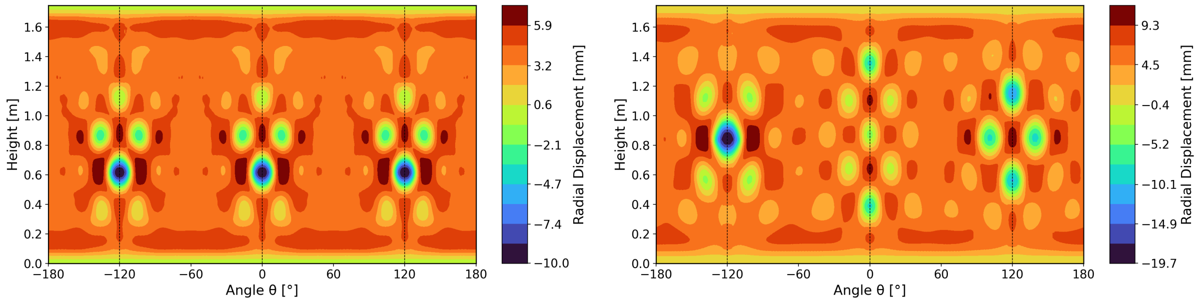

(c) TA07 buckling pattern.

(d) TA09 buckling pattern.

Figure 5.13: Eigenmode buckling modes at 4 bar internal pressure.

5.3. Statistical Reliability

In this section, the results of the statistical measures are introduced and discussed, with a focus on the initial statistical metrics in the following subsections. Where the application of a given method depends on a particular data structure, the corresponding normality and heteroscedasticity test results are also presented. The methods are discussed in the following order: coefficient of variation in subsection 5.3.1, Kendall's W in subsection 5.3.2, and ICC in subsection 5.3.3.

5.3.1. Coefficient of Variation Analysis

Based on the global trends discussed previously, pressurized buckling appears more consistent than its unpressurized counterpart. To quantify this behavior, a reliability assessment was carried out. As shown in Table 5.2, none of the individual pressure levels satisfy the heteroscedasticity requirement for the coefficient of variation to be formally applicable. The null hypothesis of constant residual variance is rejected only for the combined 2 bar+4 bar dataset. CV values were therefore computed for completeness and are reported in Table 5.3, but comparisons across pressure levels should be interpreted with caution. Nevertheless, the CV results validate the interquartile trends: increasing pressure reduces the relative variability of the buckling predictions, with CV decreasing monotonically across the considered pressure levels.

Table 5.2: Results of the Breusch–Pagan heteroscedasticity tests at different pressure levels.

Pressure [bar]	BP p-value	H_0: Homoscedasticity
0	0.4550	Fail to reject
2	0.0770	Fail to reject
4	0.1781	Fail to reject
2+4	0.0015	Reject

In the combined pressure case, the lowest CV values are obtained with the SPLA variants, followed by MGI and SPLAOG, indicating that these imperfection-modeling strategies yield the most consistent structural response. At the opposite end, the DFPA variants exhibit the highest variability. This lack of consistency is likely governed by the interaction between the DFPA-induced weld land imperfection field and the shell-specific weld geometry, which will be further discussed in subsection 5.3.3.

Interestingly, the MPLA case using the unpressurized converged perturbation magnitude shows lower variability (CV = 0.041) than the standard MPLA variant (CV = 0.058). This behavior aligns with the smaller dimple amplitudes associated with the baseline convergence loads, which reduce stiffness degradation and yield more uniform buckling loads across the structures.

Table 5.3: Coefficient of variation (CV) per method across pressure levels. Columns marked with * correspond to heteroscedastic data.

Method	CV_0	CV_2	CV_4	$CV_{2+4}{}^*$
SPLA	0.067	0.026	0.031	0.026
GNA	0.082	0.037	0.022	0.030
MGI	0.154	0.036	0.007	0.026
DFPA	0.179	0.172	0.143	0.150
MPLA	0.191	0.069	0.051	0.058
EIA	0.196	0.058	0.027	0.045
SPLAOG	–	0.031	0.023	0.026
MPLAOG	–	0.050	0.031	0.041
DFPAOG	–	0.169	0.147	0.150

5.3.2. Coefficient of Concordance Analysis

Kendall's W does not require assumptions on the underlying data distribution and can therefore be applied directly. Unlike the coefficient of variation or ICC, it does not assess the absolute magnitude of the response - only the rank ordering matters.

Firstly, the resulting coefficients per method are presented in Table 5.4. In this formulation, W measures how consistently a given modeling approach ranks the structures across pressure levels—essentially, how stable the relative buckling predictions remain as pressure increases.

The two most conservative approaches, DFPA and DFPAOG, show near-perfect agreement (W = 0.91). This indicates that, for these methods, the relative ranking of the structures is almost unchanged across pressure levels - pressure mainly scales the buckling loads but does not reorder the cylinders in terms of predicted buckling strength. The MPLAOG variant and the EIA approach follow with W = 0.78 and W = 0.73, respectively, implying moderate sensitivity to pressure changes while still maintaining a high degree of rank stability. MGI trails just behind with W = 0.69, consistent with its higher variability, as both the magnitude and spatial character of the measured imperfection fields differ between shells, leading to more frequent shifts in their estimated collapse loads.

Table 5.4: Coefficient of concordance for all approaches across pressurization levels.

Method	**Kendall's W**
DFPA	0.91
DFPAOG	0.91
EIA	0.78
MPLAOG	0.73
MGI	0.69
MPLA	0.62
SPLAOG	0.62
GNA	0.51
SPLA	0.49

The lowest agreement is observed for SPLA (W = 0.49). This suggests that a single shallow local imperfection, scaled only in amplitude, does not provide a uniform representation of the pressure-dependent buckling behavior across the cylinders. In this regime, the pressure effect becomes dominant, and the ranking tends to align more closely with the geometrically perfect GNA response (W = 0.51), while the imposed perturbation no longer governs the structural response consistently.

Kendall's W was also calculated per structure to assess how consistently the modeling approaches estimate collapse loads across pressure levels. Ideally, if the pressure–method interaction were independent of the barrel design, each structure would exhibit an identical ordering of methods at all pressures. In this context, W quantifies how stable the ranking of modeling approaches remains as pressure increases.

Table 5.5: Kendall's W per structure, quantifying agreement between method rankings across pressure levels.

Structure	**Kendall's W**
TA01	0.97
TA07	0.97
TA09	0.94
TA03	0.86
ETTA1	0.61

The obtained results presented in Table 5.5 align well with the conclusions drawn from the IQR study. The structures least sensitive to pressurization, TA01 and TA07, show the highest agreement across pressure levels (W = 0.97), followed by TA09 (W = 0.94). TA01 includes additional stringers near the weld land, while TA07 and TA09 employ a picture-frame stiffener layout. In all three cases, the increased weld land stiffness reduces the sensitivity of the buckling response to pressure-induced changes. For these cylinders, pressure primarily scales the collapse load without altering the relative influence of the imperfection-modeling approaches, and the ranking of methods is therefore preserved. TA03 shows lower agreement (W = 0.86), indicating that the relative performance of the methods shifts as pressure increases, which has already been substantiated during the interquartile analysis. The lowest agreement is obtained for ETTA1 (W = 0.61), confirming that this structure is most affected by pressure–structure interaction and the associated local deformation patterns.

For ETTA1, the normalized buckling loads from 2 bar were duplicated at 4 bar to maintain a balanced dataset, since the shell could not be pressurized further without local yielding, and hence the ranking of the methods is identical. Nevertheless, structure exhibits elephant-foot buckling - a mode dominated by global geometry rather than amplitude-sensitive imperfections, and as a result, the normalized collapse loads are near-identical across methods. Due to the small disparities between them, the method reshuffles the order extensively compared to the non-pressurized case. The new ranking significantly varies from the first one, and despite the 4 bar being identical to 2 bar, leads to reduced Kendall's W relative to the other shells.

Overall, the analysis shows that the consistency of the modeling approaches is strongly structure-dependent, with weld-reinforced configurations exhibiting more uniform behavior across methods. While some approaches are inherently more rank-stable, the less conservative ones are more strongly influenced by the interaction between pressure and structural stiffness, leading to reduced agreement as the pressurization level increases.

5.3.3. ICC Analysis

The absolute reliability of the results was evaluated using the intraclass correlation coefficient. The ICC measures how consistently the modeling approaches predict the absolute collapse loads across shells and pressures. Each value is reported together with a 95% confidence interval, which indicates the precision of the estimate (Table 5.9). In several method-based cases, the intervals are wide, and the lower bounds extend into the negative range—this reflects low statistical precision stemming from a small sample (15 data points) rather than "negative reliability" [52]. In contrast, the pressure-based ICC values exhibit much narrower intervals, primarily due to the larger number of observations per pressure level (45 data points) [56]. Consequently, the ICC values in this study should be interpreted as qualitative indicators of relative reliability, rather than strict statistical limits, especially when the underlying assumptions are not fully satisfied. Similarly to Kendall's W, for ETTA1, the normalized buckling loads from 2 bar were duplicated at 4 bar to maintain a balanced dataset.

Table 5.6: AAssumption checks for ICC analysis: Breusch–Pagan (homoscedasticity) and Shapiro–Wilk (normality) tests.

Pressure [bar]	BP p-value	H_0: Homoscedasticity	SW p-value	H_0: Normality
0	0.4550	Fail to reject	0.4234	Fail to reject
2	0.0779	Fail to reject	0.0842	Fail to reject
4	0.1778	Fail to reject	0.0083	Reject

Table 5.7: Method-wise ICC assumption checks: Breusch–Pagan test for heteroscedasticity.

Method	BP p-value	H_0: Homoscedasticity	SW p-value	H_0: Normality
DFPA	0.7917	Fail to reject	0.0083	Reject
DFPAOG	0.8767	Fail to reject	0.0807	Fail to reject
EIA	0.1342	Fail to reject	0.7415	Fail to reject
GNA	0.0351	Reject	0.1529	Fail to reject
MPLA	0.2085	Fail to reject	0.1592	Fail to reject
MPLAOG	0.1504	Fail to reject	0.3383	Fail to reject
MGI	0.1209	Fail to reject	0.2610	Fail to reject
SPLA	0.1787	Fail to reject	0.0670	Fail to reject
SPLAOG	0.1448	Fail to reject	0.0942	Fail to reject

As outlined, the assumptions of homoscedasticity and normality required for ICC calculation were first evaluated. The results are presented in Table 5.6 for pressure-based ICC, and in Table 5.7 for method-based. Consistent with the earlier coefficient of variation analysis, the data across pressure levels is not uniformly homoscedastic, and the same behaviour is observable when inspecting individual methods. Likewise, the Shapiro–Wilk test rejected normality for 4 bar cases and for the DFPA method. These tests already indicate how the distribution of collapse loads evolves under increasing internal pressure.

The change in normality with pressure is directly related to the degree to which the collapse response remains geometrically dominated. At 0 bar, the variability of the collapse load is broad and smooth, resulting in a high Shapiro–Wilk p-value. With increasing pressure, the shell stiffens, and the response becomes less sensitive to local geometric imperfections, reducing the spread of values, as visible in Figure 5.9 and Figure 5.10. At higher pressures, this narrowing of the distribution is sufficient to suppress the tails, allowing the normality assumption to fail.

For the distributed force perturbation approach, the loss of normality appears to arise from the relative structural performance of the shells under this loading rather than from variability in the method itself. As discussed previously, TA01 is the most resilient to the formation of the half-wave dents at weld lands owing to the presence of additional stiffeners. TA07 and TA09 feature the ‘picture-frame’ stiffener transition, where a stringer runs adjacent to the weld land. This configuration improves their resistance to the DFPA-induced buckling mode, though to a lesser extent than TA01. As shown in Figure 5.9,Figure 5.10, both TA07 and TA09 indeed exhibit nearly identical performance.

By contrast, TA03 and ETTA1 employ a traditional tapered stiffener transition, where the first stiffener is positioned at the end of the transition region. Based on this geometry alone, both would be expected to buckle at comparatively lower loads, though this is not reflected in the results. The space shuttle external tank segment performs significantly better, whereas TA03 persistently yields the lowest normalized buckling load across all pressure levels for this imperfection type. The difference in performance is most likely due to the slenderness difference R/t_{eff} of 309.3 to 80.1 and possibly the article scale effect. As a result, the performance groups form three distinct clusters: two shells (TA07 and TA09) with intermediate performance, one shell (TA03) performing comparatively poorly, and two shells (TA01 and ETTA1) performing considerably better. This clustering produces a skewed distribution rather than a symmetric one, which directly explains the observed lack of normality for DFPA.

Table 5.8: ICC assumption checks excluding the 0 bar cases: Breusch–Pagan and Shapiro–Wilk tests.

Method	BP p-value	H_0: Homoscedasticity	SW p-value	H_0: Normality
DFPA	0.6119	Fail to reject	0.0083	Reject
DFPAOG	0.7166	Fail to reject	0.0807	Fail to reject
EIA	0.2862	Fail to reject	0.7415	Fail to reject
GNA	0.3857	Fail to reject	0.1529	Fail to reject
MPLA	0.5540	Fail to reject	0.1592	Fail to reject
MPLAOG	0.3980	Fail to reject	0.3383	Fail to reject
MGI	0.0559	Fail to reject	0.2610	Fail to reject
SPLA	0.7592	Fail to reject	0.0670	Fail to reject
SPLAOG	0.2084	Fail to reject	0.0842	Fail to reject

The origin of heteroscedasticity in GNA can be attributed to noticeable changes in variance with pressure. A low coefficient of concordance already showed that GNA is a pressure-sensitive method, and the structures exhibit significant performance variability from unpressurized to 4 bar loading. When the Breusch–Pagan and Shapiro-Wilk tests are repeated excluding the 0 bar baseline - results presented in Table 5.8, both homoscedasticity and normality are obtained for all approaches.

Table 5.9: Intraclass Correlation Coefficient ICC(3,1) per method with and without the 0 bar condition.

Method	ICC(3,1)	95% CI	ICC(3,1) excl. 0 bar	95% CI excl. 0 bar
DFPA	0.90	[0.53–0.99]	0.89	[0.04–0.99]
DFPAOG	0.93	[0.63–0.99]	0.90	[0.11–0.99]
EIA	0.65	[0.00–0.97]	0.70	[-0.46–0.98]
GNA	0.07	[-0.37–0.85]	0.38	[-0.75–0.94]
MPLA	0.82	[0.29–0.99]	0.91	[0.15–0.99]
MPLAOG	0.71	[0.07–0.98]	0.83	[-0.18–0.99]
MGI	0.02	[-0.39–0.83]	0.09	[-0.86–0.90]
SPLA	0.76	[0.12–0.98]	0.79	[-0.29–0.98]
SPLAOG	0.62	[-0.04–0.97]	0.78	[-0.32–0.98]

The ICC per method (temporarily disregarding the assumption violation for DFPA) shown in Table 5.9 indicates that MGI exhibits the lowest reliability (ICC = 0.03), and this remains the case even when the unpressurized state is excluded (ICC = 0.09). This confirms that MGI predictions vary substantially with pressure and become unreliable once pressurization stiffens the shell and partially suppresses the influence of the measured imperfection field. This behavior is noteworthy, given that MGI is typically regarded as the most accurate approach for unpressurized analysis, as demonstrated on small-scale specimens by [77]. However, due to the strongly localized imperfection shape and magnitude, despite strong evidence of imperfections’ signature pattern between the shells, at elevated pressure, the response becomes highly dependent on local shell behavior, reducing its predictive robustness. Despite a relatively narrow spread in the IQR analysis, the corresponding performance of structures shifts noticeably, as visible in Figure 5.9 and Figure 5.10. In this sense, MGI behaves similarly to the geometric nonlinear analysis, which also shows poor reliability across cases (ICC ranging from 0.07 to 0.38).

At the opposite end, the MPLA and DFPA variants exhibit the highest reliability across the pressure levels. DFPAOG provides the most consistent predictions (ICC = 0.93) and performs slightly better than its per-pressure variant (ICC_{DFPA} = 0.90). MPLA, when evaluated only for the pressurized states, also yields high reliability (ICC = 0.82). For both considered cases, the remaining approaches show moderate reliability: SPLA ICC = 0.76-0.79, EIA ICC = 0.65-0.70, and SPLAOG ICC = 0.62-0.78.

When the unpressurized baseline is excluded, the reliability of both MPLA variants improves further, with the per-pressure MPLA becoming the most reliable method (ICC = 0.91). The ICC for the DFPA variants decreases slightly, but the analysis becomes valid, as both statistical assumptions are satisfied once the baseline is removed. This marginal decrease may be linked to the visibly wider collapse-load spread at 2 bar relative to 4 bar.

Table 5.10: Intraclass Correlation Coefficient ICC(3,1) per pressure level.

Pressure [bar]	**ICC(3,1)**	**95% CI**
0	0.72	[0.46–0.91]
2	0.88	[0.72–0.97]
4	0.93	[0.83–0.98]

Finally, the intraclass correlation coefficient was also evaluated per pressure level. In this formulation, the ICC quantifies the reliability of all methods under a fixed internal pressure. The results in Table 5.10 mostly reaffirm the trends already visible in the boxplots and do not introduce additional new insight. At 0 bar, the reliability is only moderate, reflecting the large dispersion in collapse loads. With increasing pressure, the ICC rises to good or excellent levels. This behavior is consistent with reduced imperfection sensitivity under pressurization. Once the shell stiffens, the relative influence of the imposed imperfection shapes diminishes, leading to more uniform predictions. However, the same pressure-induced narrowing of the collapse-load distribution leads to the normality requirement failing at higher pressures. Consequently, the ICC values at 4 bar should be interpreted with caution.

5.4. Discussion

In this work, several imperfect buckling-modeling strategies were applied to five cylindrical shells over three internal pressure levels. The resulting response highlights a strong interaction between internal pressurization and buckling behavior, which is highly structure-dependent and influenced by parameters such as shell radius, skin stiffness, orthogrid layout, and weld land design. In general, the 2.4 m-diameter test articles exhibit smaller pressure-induced performance gains than the 8.4 m Space Shuttle external tank segment. Among shells of equal diameter, the magnitude of the pressure-induced stiffness improvement further depends on the orthogrid pattern, stiffener height, skin thickness, and transition-region geometry.

Across all structures, the increase in collapse load between 0 bar and 2 bar is substantially larger than that between 2 bar and 4 bar, indicating the presence of a pressure-effect threshold beyond which additional pressurization yields diminishing stiffening benefits. This trend is consistent with previously reported observations for small-scale pressurized cylinders [77].

The following subsections evaluate the performance and reliability of each imperfection-modeling strategy in light of these trends, with particular emphasis on the associated imperfection signatures and the statistical reliability measures.

5.4.1. GNA Reliability

The geometric nonlinear approach - used as a benchmark of the performance, is inherently the least conservative approach, producing the highest collapse loads for all shells. Simultaneously, it exhibits the lowest reliability - both ICC and Kendall's W confirm weak consistency and agreement across pressure levels. This is reflected in the wide spread of normalized buckling loads, indicating that GNA is strongly structure-dependent.

Despite this, comparison with unpressurized buckling tests for TA01 [42] and pressurised results from [58] for ETTA1 suggests that the simplified GNA model may approximate the true buckling loads more closely than some imperfect-shape methods, primarily due to modeling assumptions (listed in section 4.5) leading to underestimating the structures stiffness. The method remains useful as a baseline but offers limited predictive robustness in a pressurized environment.

5.4.2. EIA Reliability

The eigenmode imperfection approach, widely used in industry, shows moderate consistency (Kendall's W = 0.73), suggesting that its shell-specific imperfection fields are only moderately influenced by increasing internal pressure. The ICC values indicate moderate overall reliability.

This behavior reflects the method's sensitivity to the interaction between pressure and structural stiffness. Moreover, for some shells, the dominance of local eigenmodes over the global one in the linear buckling analysis complicates the selection of an appropriate one. Furthermore, the choice of the reference thickness for mode amplitude scaling significantly impacts the method's effect on the structure's stiffness. Lastly, EIA does not reflect the imperfection signature associated with the manufacturing of the metallic segments - instead, it results from the stiffness distribution.

5.4.3. MGI Reliability and Imperfection Signature Consistency

The measurements of the shells' OMLs confirmed a strong association of manufacturing method with the shell's radial displacement, validating that the imperfection signature from welding is present and impacts the buckling performance for all considered structures. All shells exhibit weld land-dominated signatures (to a varying degree), but their magnitudes differ substantially. The observed pattern for TA01 does not resemble the ones observed for other test articles. Smaller shells were most likely manufactured at the same facility, roughly in the same period, and yet exhibit different imperfection patterns and magnitudes. For TA03, the magnitude of the radial deformation was not available in literature and thus was adapted from the other small articles' measurements. The verification showed that, although it was a representative value, the assumed magnitude was too large, leading to conservative buckling estimates. Further evidence is seen when comparing TA01 and TA02 (built for combined axial and bending testing [83]) - Figure 5.14, which share the same orthogird design yet display different imperfection patterns. The source of the imperfection for TA02 seems to be more related to the forming phase of the manufacturing than the actual stir friction welding.

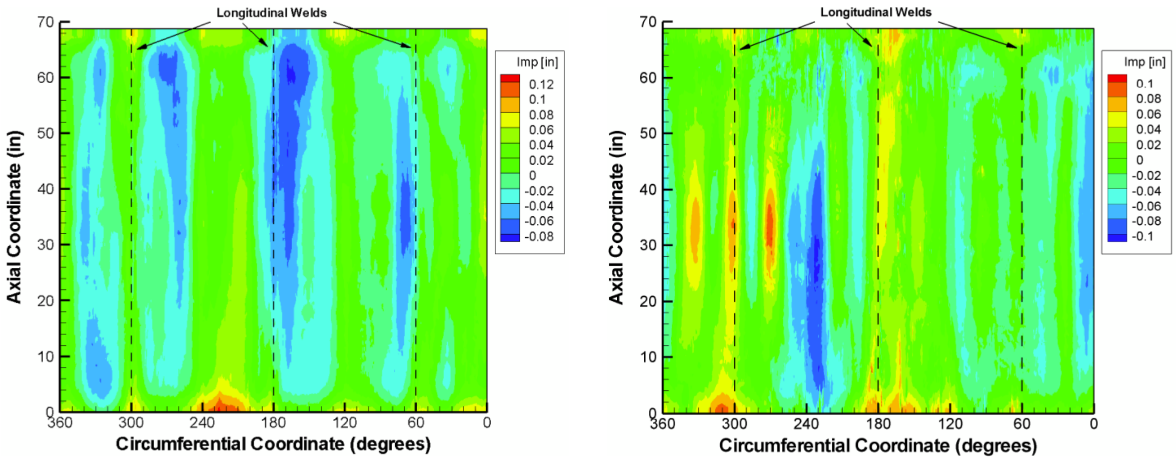

(a) Measured radial imperfections of TA01.

(b) Measured radial imperfections of TA02.

Figure 5.14: Comparison of OML radial imperfections of TA01 and TA02, with identical grid pattern [83].

This highlights that knowing the imperfection signature is insufficient - its magnitude and spatial distribution strongly influence the response, making MGI highly structure-specific.

Statistically, MGI has one of the highest concordance measures (Kendall's W) but very low ICC, driven by significant changes in shell buckling performances across pressure levels. The IQR analysis shows significant normalized buckling variability, except at 4 bar, where internal pressure nearly entirely suppresses the imperfection effect. The pressure effect leads to reaching collapse loads at the same level or even higher than those obtained for GNA. This aligns with Sim et al. [77] findings, who reported that MGI may become unconservative at higher pressures depending on the shell design and pressure range. High uncertainty and the need for actual measurements of the designed specimen make this approach infeasible for the preliminary/detailed phases of the development, with potential use only for qualification/verification.

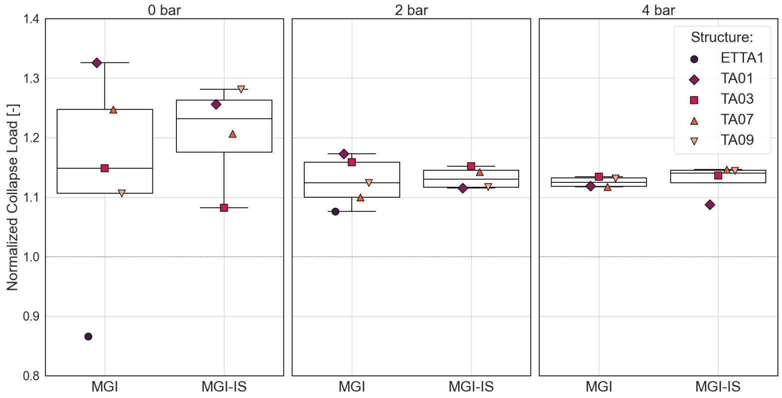

Figure 5.15: Buckling performance comparison between the measured imperfections (MGI) and imposed radial imperfections (MGI-IS).

Nonetheless, this study relied on measured imperfections of the built shells, as all structures were physically manufactured. In a real design environment, these data would not be available, and more generic imperfection patterns would be required. To assess how manufacturing variability influenced the analysis, a sensitivity study was performed in which an identical imposed imperfection field was applied to all structures. The study was limited to the 2.4-m shells due to their dimensional and manufacturing consistency. The radial imperfection field was taken from TA09 (shown in Figure 5.7), as it was the most representative of the assumed signature, exhibiting three distinct longitudinal half-waves at the welds and having the largest magnitude. The statistical analysis was repeated with this sensitivity case included, but importantly, the newly obtained collapse loads were not used for normalization. This prevented artificial bias, since the imposed imperfection pattern was identical across the shells, and could lead to skewing data distribution. The comparison of normalized buckling load spreads is illustrated in Figure 5.15.

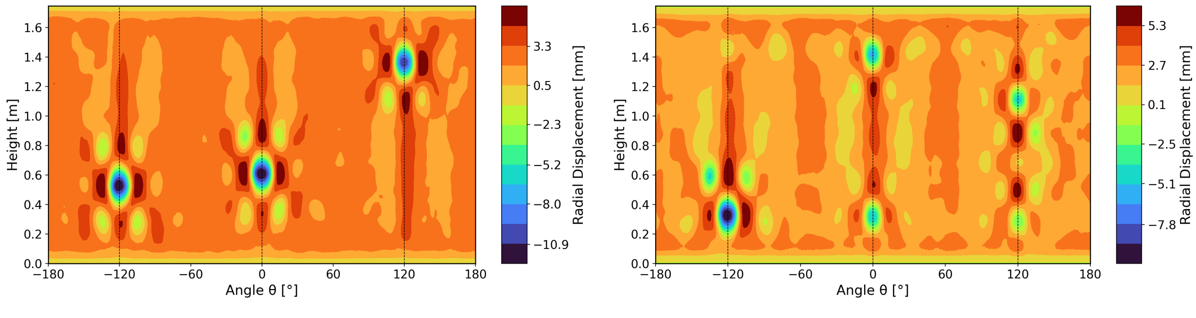

(a) Buckling mode with the original imposed radial imperfections.

(b) Buckling mode with the TA09 imposed radial imperfections.

Figure 5.16: Comparison of buckling mode of TA07 with different measured imperfections.

The imposed imperfection pattern reduces the shell performance more strongly than the original measurements, as both the number of dents and their magnitude increase. At 0 bar, the difference between the actual MGI and the artificial MGI-IS collapse loads ranged from −5.8% to −3.3%, decreasing gradually with pressure to reach −2.8% to +2.5% at 4 bar. The largest deviation occurred for TA07, which collapse load (as the only structure) increased notably under pressurization relative to its MGI baseline. This behavior is not fully understood, as the measured OML imperfections for TA07 are narrower and shallower than those imposed. A closer inspection of the buckling modes at 2 bar (where the discrepancy is largest), shown in Figure 5.16, reveals a fundamental mode change, including different half-wave numbers, locations, and amplitudes.

For the coefficient of variation across 2 and 4 bar, the imposed-pattern case gives the lowest scatter among all methods, with a CV of 0.024, slightly outperforming the original MGI (CV = 0.026). As visible in Figure 5.15, this reduction results primarily from the significantly smaller spread at 2 bar.

The copied imperfections result in a Kendall's W of 0.62, lower than the original MGI, likely caused by the ranking change of TA07. The intraclass correlation coefficient across all pressures is negative (ICC=−0.21, CI95% $=[-0.45, 0.67]$). Since ICC(3,1) becomes negative only when $MS_{\text{error}} > MS_{\text{rows}}$, the result indicates that the pressure-dependent variability dominates the structural variability, leading to a larger error. For the original MGI, this error term is also large but slightly smaller, resulting in a very small yet positive ICC. It is plausible that a larger set of shells would shift the value into a weakly positive range.

Together, these results show that MGI exhibits low reliability across the full pressure range. However, when the 0-bar condition is removed, the ICC increases to 0.72, substantially higher than the original MGI value (0.10). This demonstrates that the MGI approach can appear reliable, but only when the imperfection effect remains strong and uniform. Such conditions cannot be guaranteed in practice. Despite being nominally “equivalent” to MGI in collapse magnitude, the subtle differences in collapse loads produced by MGI-IS lead to statistically different reliability characteristics.

It is therefore difficult to draw firm conclusions about the mathematical reliability of the method. If a consistent imperfection signature can be assumed for all structures — and reliably reproduced in future designs — the method can demonstrate high reliability. Otherwise, if the imperfection pattern differs between shells, the reliability quickly deteriorates.

5.4.4. SPLA & MPLA Reliability

The single and multiple perturbation approaches and their variants, with perturbation loads taken from the unpressurized baseline convergence study, showed significantly different behaviors.

SPLA produces relatively high collapse loads—second only to GNA and MGI, but shows the lowest Kendall's W (0.49), indicating strong variation of the method's influence across structures and pressures. The single perturbation dimple is highly sensitive to local shell stiffness and weld land geometry, and this sensitivity changes with internal pressure. Nonetheless, SPLA maintains good absolute reliability (ICC).

MPLA shows the opposite trend, moderate concordance but excellent absolute reliability. It consistently produces collapse loads near the cross-method mean and is the only perturbation-based strategy that reproduces the imperfection signature of all shells with reasonable accuracy (apart from MGI). However, its response is strongly dependent on the magnitude of the converged perturbation. As demonstrated, some structures did not exhibit a strong convergent behavior within the selected range of dimple amplitude-to-thickness ratio, particularly TA03, which recorded the highest normalized collapse loads despite lacking weld-reinforcement. The convergence disturbance is governed by different phenomena. It is usually caused by one or more recorded responses falling beyond the 3σ interval due to the perturbation loads following a different convergence path. The existence of these outliers was not fully studied, but it is also possible that they are influenced by the numerical setting of the solver.

The simplified SPLA-OG and MPLA-OG variants, which use the unpressurized convergence load for all pressures, track the behavior of their full counterparts closely and achieve higher Kendall's W. Their reliability is reduced compared to the standard methods because pressure-dependent stiffening is not reflected in the imperfection amplitude. Nevertheless, the approach has potential - it achieves collapse loads comparable to those from full convergence studies while reducing computational cost.

Nevertheless, as reported by [77] for small-scale shells, both perturbation methods, after reaching a particular pressure threshold, became unconservative in their results. Furthermore, the study confirmed the order of the approaches in terms of magnitude of the collapse load, ranking the MPLA behind the SPLA and MGI.

5.4.5. DFPA Reliability

The distributed force perturbation approach was introduced as a computationally efficient alternative to SBPA. Although it reproduces SBPA-like buckling patterns, DFPA is significantly more conservative across all pressure levels. This is partly due to the modeling assumptions - edge warping allowed and load-controlled analysis, which are known to lower predicted collapse loads [88].

DFPA and DFPAOG consistently produce the lowest collapse loads, but they also yield the highest method consistency (Kendall's W) and the strongest absolute reliability. The collapse load remains heavily influenced by shell design: reinforced weld land structures offer greater resistance to the localized loads, whereas conventional weld land configurations lead to extremely conservative predictions.

The results confirm observations made by Sim et al. [77] that non-traditional imperfection methods are less sensitive to pressure-induced stiffening. However, DFPA appears overly conservative relative to the other approaches and should not be treated as the most accurate method for metallic launch-vehicle shells.

6

Conclusions and Recommendations

This thesis set out to compare the performance of several imperfection modeling buckling strategies across a range of pressures for representative launch vehicle metallic propellant tank segments, to identify the most relevant one for future use. Due to limited pressurized shell buckling test data, the currently used methods are overly conservative, fail to leverage current high-precision manufacturing, and result in poor design selection in the early stages of vehicle development.

An extensive literature study was conducted, establishing approaches that have been utilized in the past for buckling assessment of launch vehicle structures, with potential application to the analysis of pressurized hardware. These methods have been modified and adjusted for this work to account for internal pressure. The imperfection modeling strategies are divided into those that aim to replicate the effects of manufacturing imperfections, called traditional imperfections, and those that rely on imperfect load transfer or distribution at the boundary condition, referred to as non-traditional imperfections. The review identified the ideal structures for the analysis, establishing that NASA's Shell Knockdown Factor Project test articles are the most suitable candidates, spanning nearly an entire feasible domain of launch propellant tank designs. The study revealed that metallic propellant tank shells exhibit a common imperfection pattern, referred to as an imperfection signature, left by friction stir welding multiple curved tank panels into barrel segments. Simultaneously, newer work showed that the weld land geometry itself dictates the buckling performance of shells more than the imperfection signature.

The study led to the formulation of the following research question:

To what extent does the reliability of imperfection modeling approaches for pressurized metallic stiffened launch vehicle propellant tank segments depend on the recreation of the imperfection signature?

Based on this question, the following hypothesis is proposed:

There exists an imperfection modeling approach that does not resemble the imperfection signature, but can provide high reliability in the prediction of buckling behavior for pressurized cases.

Research Question Answer

The extensive analysis revealed several ambiguities in the relationship between reliability and imperfection-modeling approaches.

Firstly, the reliability of a given method depends strongly on how reliability is defined. Depending on whether relative agreement or absolute consistency is deemed more important, the results would change. Similarly, whether reliability should reflect only the final collapse load or also the robustness of the intermediate modeling steps leads to different interpretations.

In this study, agreement and consistency were treated as equally important, and the modeling procedure was required to remain verifiable throughout the analysis chain. Under this definition, no method can be considered universally reliable and accurate across all pressure levels.

Methods closely tied to shell stiffness, design features, or manufacturing-related imperfections tend to be less consistent. Their performance becomes highly dependent on the specific structural configuration, increasing scatter and reducing predictability. At 0 bar, the shell is susceptible to local geometric details, whereas increasing pressure progressively suppresses radial imperfections and reduces the dependence on the exact imperfection signature. When the initial imperfections are significant or their magnitude scales with pressure, their influence persists longer, making the approach appear more reliable. However, the agreement observed across shells under pressure remains configuration-dependent, making the consistency–agreement relation inherently ambiguous.

Signature-reproducing approaches - MPLA and MGI, show mixed behavior. MGI exhibits reduced reliability because every measured shell is unique and reflects structure-specific variability. If the imperfection map applied were always identical, then the reliability would increase, but the pattern obtained can not be guaranteed to match the prediction, based on the current evidence. MPLA, which aims to capture the dominant effect of weld centerline indentations through multiple perturbation locations, is less affected by pressure but still limited by a convergence criterion that can behave poorly for specific configurations.

The remaining methods that do not attempt to recreate the signature - SPLA, EIA, and GNA, either become overly sensitive to pressure, resulting in uncorrelated performance between shells, or remain inherently dependent on shell stiffness, producing significant performance variation across different designs. The loading-type imperfection in DFPA is the only approach that does not modify the shell stiffness by altering its geometry, and it therefore benefits cleanly from pressure stiffening, showing stable improvements with increasing pressure.

Overall, MPLA and DFPA become the most reliable in pressurized cases, yielding high Kendall's W, strong ICC values, and consistent trends across shells. However, MPLA's convergence behavior limits its reliability (likely inaccurate), while DFPA remains highly conservative and dependent on the weld land design.

Consequently, the hypothesis is both supported and contradicted depending on the interpretation. When accuracy and reliability are considered together, MPLA, which partially recreates the imperfection signature, offers the best balance, yielding collapse results between conservative DFPA and the highly overconservative remaining methods. If only reliability is prioritized, DFPA becomes the preferred option despite its conservative bias.

Recommendations for future work

The current study focused almost entirely on numerical reliability, given the extremely limited validation options available to assess the accuracy of the considered methods. Therefore, the most important recommendation is to perform a dedicated buckling test campaign at representative pressure levels and structural scales. Experimental data would allow direct comparison with numerical predictions, enable the calculation of pressurized knockdown factors, and provide a far deeper understanding of method reliability and the structure–approach interaction.

Secondly, although this work concentrated on metallic shells, the growing adoption of composites in launch vehicles makes it highly relevant to investigate imperfection-modeling strategies for pressurized CFRP tanks. As reported in the literature, a composite shell's sensitivity to specific imperfection fields depends strongly on the laminate configuration - understanding how internal pressure modifies this relationship would be valuable.

Regarding the scope of this work, the study could be extended to additional shells with different stiffener layouts—for example, the isogrid cylinders ITA01 and ITA02 from the SBKF programme [43]. To determine the effect of weld land effects under pressure, the study can be extended to include a seamless integrally machined cylinder, such as STA8.1 [69], which has been used in the unpressurized studies on the subject. Moreover, tank designs with non-integrally machined stiffeners should be included in future studies, as these designs might exhibit different imperfection signatures, influenced by sets of stiffener welds. Overall, extending the work with multiple manufacturing and stiffening concepts would reveal if the discovered trends and observations are universal or specifically hold for tank designs assumed in the work.

In terms of general pressure-dependent behavior, it would be beneficial to identify which structural parameters specifically control the extent of the stabilizing effect, which, as this study demonstrated, varies substantially between shells. In addition, the threshold beyond which further pressurization no longer increases the collapse load warrants detailed investigation. Small-scale tests conducted by Sim et al. [77] have already suggested such a limit, but new test articles would likely be required, since SBKF cylinders reach skin pocket yielding at roughly 5 bar.

With respect to numerical procedures, further work should explore the use of dynamic implicit analysis in pressurized buckling. Alternatives such as quasi-static dynamic applications should be examined, and a systematic study should aim to determine the optimal non-default HHT damping parameter. In the same context, the single boundary perturbation approach should be reincluded and evaluated under realistic pressure levels and dynamic-implicit schemes, since previous studies used only low-pressure static Newton–Raphson analyses [76, 77].

The distributed force perturbation approach proposed in this thesis should also be refined, particularly in optimizing the perturbation width, as in this work, it was derived solely on one structure. Furthermore, alternative boundary conditions should be explored in greater detail to identify ways to reduce shell warpage at the edges and, consequently, increase the collapse loads of the analyzed shells.

Finally, the statistical analysis would greatly benefit from larger datasets. The intraclass correlation coefficient, in particular, operates at the limit of stability with the small sample size available here. Increasing at least the number of pressurization levels would significantly improve the robustness and precision of the confidence intervals.

References

[1] En 1993-1-6: Eurocode 3: Design of steel structures - part 1-6: Strength and stability of shell structures. Technical report, EUROPEAN COMMITTEE FOR STANDARDIZATION, 2 2007.

[2] M. A. Arbelo, R. Degenhardt, S. G. Castro, and R. Zimmermann. Numerical characterization of imperfection sensitive composite structures. *Composite Structures*, 108:295–303, 2014. ISSN 02638223. doi:10.1016/j.compstruct.2013.09.041.

[3] J. Arbocz and J. H. Starnes Jr. Future directions and challenges in shell stability analysis. *Thin-Walled Structures*, 40:729–754, 9 2002. ISSN 02638231. doi:10.1016/S0263-8231(02)00024-1.

[4] J. Arbocz and J. G. Williams. Imperfection surveys on a 10-ft-diameter shell structure. *AIAA Journal*, 15 (7):949–956, 1977. ISSN 00011452. doi:10.2514/3.7389.

[5] W. Balogh. International context, space law and regulations. ESA Academy Presentation, 2025. Presented by Werner Balogh, Head of Space Transportation Policy & Communication Office, ESA Space Transportation Directorate.

[6] C. A. Bobak, P. J. Barr, and A. J. O'Malley. Estimation of an inter-rater intra-class correlation coefficient that overcomes common assumption violations in the assessment of health measurement scales. *BMC Medical Research Methodology*, 18(1), 9 2018. ISSN 14712288. doi:10.1186/s12874-018-0550-6.

[7] T. S. Breusch and A. R. Pagan. A simple test for heteroscedasticity and random coefficient variation. *Econometrica*, 47:1287, 9 1979. ISSN 00129682. doi:10.2307/1911963.

[8] D. Bushnell. Buckling of shells-pitfall for designers. *AIAA Journal*, 19:1183–1226, 9 1981. ISSN 0001-1452. doi:10.2514/3.60058.

[9] S. Castro, J. Reichardt, and E. Lozano. DESICOS Plug-in for Abaqus, 2 2021. URL `https://zenodo.org/records/4506587`. Accessed: 02.07.2025.

[10] S. G. Castro, R. Zimmermann, M. A. Arbelo, and R. Degenhardt. Exploring the constancy of the global buckling load after a critical geometric imperfection level in thin-walled cylindrical shells for less conservative knock-down factors. *Thin-Walled Structures*, 72:76–87, 2013. ISSN 02638231. doi:10.1016/j.tws.2013.06.016.

[11] S. G. Castro, R. Zimmermann, M. A. Arbelo, R. Khakimova, M. W. Hilburger, and R. Degenhardt. Geometric imperfections and lower-bound methods used to calculate knock-down factors for axially compressed composite cylindrical shells. *Thin-Walled Structures*, 74:118–132, 2014. ISSN 02638231. doi:10.1016/j.tws.2013.08.011.

[12] H. R. Coldwater, R. R. Foll, G. J. Howell, and J. A. Dutton. Space shuttle external tank performance improvements — the challenge. In *NASA Conference Publication*, pages 357–364, 1985. URL `https://ntrs.nasa.gov/api/citations/19850008607/downloads/19850008607.pdf`. NASA/MSFC; Martin Marietta Aerospace.

[13] Dassault Systèmes. Abaqus 6.5 structural analysis guide: 6.3.2 Implicit Dynamic Analysis Using Direct Integration, 2009. URL `https://classes.engineering.wustl.edu/2009/spring/mase5513/abaqus/docs/v6.5/books/stm/default.htm?startat=ch02s04ath19.html`. Accessed: 08.12.2025.

[14] Dassault Systèmes. Abaqus 2016 analysis user's guide: 6.3.2 Implicit Dynamic Analysis Using Direct Integration, 2016. URL `http://130.149.89.49:2080/v2016/books/usb/default.htm?startat=pt03ch06s03at07.html`. Accessed: 08.12.2025.

[15] Dassault Systèmes. ABAQUS 2016: Element geometry, 2016. URL `http://130.149.89.49:2080/v2016/books/gsa/default.htm?startat=ch05s01.html`.

[16] Dassault Systèmes. Defining the Initial Geometry of Conventional Shell Elements, 2024. URL `https://docs.software.vt.edu/abaqusv2024/English/SIMACAEELMRefMap/simaelm-c-shellgeometry.htm`.

[17] R. Degenhardt, A. Kling, R. Zimmermann, F. Odermann, and F. de. *Dealing with Imperfection Sensitivity of Composite Structures Prone to Buckling*, chapter Chapter 1. InTech, 8 2012. doi:10.5772/45810.

[18] R. Degenhardt, S. G. Castro, M. A. Arbelo, R. Zimmerman, R. Khakimova, and A. Kling. Future structural stability design for composite space and airframe structures. *Thin-Walled Structures*, 81:29–38, 2014. ISSN 02638231. doi:10.1016/j.tws.2014.02.020.

[19] M. Deml and W. Wunderlich. Direct evaluation of the 'worst' imperfection shape in shell buckling. *Computer Methods in Applied Mechanics and Engineering*, 149:201–222, 10 1997. ISSN 00457825. doi:10.1016/S0045-7825(97)00055-8.

[20] Y. Dodge. *The Concise Encyclopedia of Statistics*. Springer New York, New York, NY, 2008. ISBN 978-0-387-32833-1. doi:10.1007/978-0-387-32833-1_200. URL `https://doi.org/10.1007/978-0-387-32833-1_200`.

[21] H. W. Douglass, M. M. Bailey, W. Wagner, R. B. Keller, C. Brownfield, R. A. Morehouse, F. R. Shwartzberg, L. T. Thompson, G. T. Smith, and R. T. Barrett. NASA Space Vehicle Design Criteria SP-8088: Liquid Rocket Metal Tanks and Tank Components. Technical report, NASA, 5 1974.

[22] D. Ducros. Artist's view of the first ariane 6 to launch, 2024. URL `https://www.esa.int/ESA_Multimedia/Images/2024/03/Artist_s_view_of_the_first_Ariane_6_to_launch`. Image by ESA; Accessed: 24.11.2025.

[23] D. Edberg and W. Costa. *Design of Rockets and Space Launch Vehicles, Second Edition*. American Institute of Aeronautics & Astronautics, 2 edition, 12 2022. ISBN 9781624106422.

[24] D. C. Elton. Stretched exponential relaxation, Aug. 2018. URL `https://arxiv.org/abs/1808.00881`. Originally written November 2013.

[25] M. Esslinger. *Hochgeschwindigkeitsaufnahmen vom Beulvorgang dünnwandiger, axialbelasteter Zylinder*. Deutsche Forschungs-und Versuchsanst. für Luft-und Raumfahrt, 1969.

[26] L. Friedrich and K. U. Schröder. Discrepancy between boundary conditions and load introduction of full-scale built-in and sub-scale experimental shell structures of space launcher vehicles. *Thin-Walled Structures*, 98:403–415, 1 2016. ISSN 02638231. doi:10.1016/j.tws.2015.10.007.

[27] L. Friedrich, T.-A. Schmid-Fuertes, and K.-U. Schröder. Comparison of theoretical approaches to account for geometrical imperfections of unstiffened isotropic thin walled cylindrical shell structures under axial compression. *Thin-Walled Structures*, 92:1–9, 2015. ISSN 0263-8231. doi:https://doi.org/10.1016/j.tws.2015.02.019. URL `https://www.sciencedirect.com/science/article/pii/S0263823115000609`.

[28] W. H. Greene. *Econometric Analysis*. Pearson Education, Upper Saddle River, NJ, 7 edition, 2012. ISBN 978-0-13-139538-1.

[29] Y. Guo, M. Pan, X. Wei, F. Luo, F. Sun, and M. Ruess. Implicit dynamic buckling analysis of thin-shell isogeometric structures considering geometric imperfections. *International Journal for Numerical Methods in Engineering*, 124(5):1055–1088, 2023. doi:https://doi.org/10.1002/nme.7150. URL `https://onlinelibrary.wiley.com/doi/abs/10.1002/nme.7150`.

[30] P. Hao, B. Wang, K. Tian, K. Du, and X. Zhang. Influence of imperfection distributions for cylindrical stiffened shells with weld lands. *Thin-Walled Structures*, 93:177–187, 8 2015. ISSN 02638231. doi:10.1016/j.tws.2015.03.017.

[31] W. Haynie and M. Hilburger. Comparison of methods to predict lower bound buckling loads of cylinders under axial compression. In *51st AIAA/ASME/ASCE/AHS/ASC structures, structural dynamics, and materials conference 18th AIAA/ASME/AHS adaptive structures conference 12th*, page 2532, 2010.

[32] W. T. Haynie, M. W. Hilburger, M. Bogge, M. Maspoli, and B. Kriegesmann. Validation of lower-bound estimates for compression-loaded cylindrical shells. In *Collection of Technical Papers - AIAA/ASME/ASCE/AHS/ASC Structures, Structural Dynamics and Materials Conference*, 2012. ISBN 9781600869372. doi:10.2514/6.2012-1689.

[33] M. Hilburger. Developing the next generation shell buckling design factors and technologies. In *53rd AIAA/ASME/ASCE/AHS/ASC Structures, Structural Dynamics and Materials ConferenceBR 20th AIAA/ASME/AHS Adaptive Structures ConferenceBR 14th AIAA*. American Institute of Aeronautics and Astronautics, 4 2012. ISBN 978-1-60086-937-2. doi:10.2514/6.2012-1686.

[34] M. Hilburger, W. Haynie, A. Lovejoy, M. Roberts, J. Norris, W. Waters, and H. Herring. Sub-scale and full-scale testing of buckling-critical launch vehicle shell structures. In *53rd AIAA/ASME/ASCE/AHS/ASC Structures, Structural Dynamics and Materials ConferenceBR 20th AIAA/ASME/AHS Adaptive Structures ConferenceBR 14th AIAA*. American Institute of Aeronautics and Astronautics, 4 2012. ISBN 978-1-60086-937-2. doi:10.2514/6.2012-1688.

[35] M. Hilburger, A. Lovejoy, R. Thornburgh, and C. Rankin. Design and analysis of subscale and full-scale buckling-critical cylinders for launch vehicle technology development. In *53rd AIAA/ASME/ASCE/AHS/ASC Structures, Structural Dynamics and Materials Conference 20th AIAA/ASME/AHS Adaptive Structures Conference 14th AIAA*, page 1865, 2012.

[36] M. W. Hilburger. Shell buckling knockdown factor: Project overview and status, 05 2015. URL `https://ntrs.nasa.gov/api/citations/20160007439/downloads/20160007439.pdf`.

[37] M. W. Hilburger. On the development of shell buckling knockdown factors for stiffened metallic launch vehicle cylinders. In *AIAA/ASCE/AHS/ASC Structures, Structural Dynamics, and Materials Conference, 2018*. American Institute of Aeronautics and Astronautics Inc, AIAA, 2018. ISBN 9781624105326. doi:10.2514/6.2018-1990.

[38] M. W. Hilburger and I. Raju. Buckling, shells, knockdown factors, and validation testing, 2012. URL `https://nescacademy.nasa.gov/video/d1138efc82bf483ca596694a206d7e811d`. Accessed: 08.12.2025.

[39] M. W. Hilburger and J. H. Starnes. Effects of imperfections of the buckling response of composite shells. *Thin-Walled Structures*, 42(3):369–397, 2004. ISSN 02638231. doi:10.1016/j.tws.2003.09.001.

[40] M. W. Hilburger and J. H. Starnes. Buckling behavior of compression-loaded composite cylindrical shells with reinforced cutouts. *International Journal of Non-Linear Mechanics*, 40:1005–1021, 9 2005. ISSN 00207462. doi:10.1016/j.ijnonlinmec.2005.02.001.

[41] M. W. Hilburger, M. P. Nemeth, and J. H. Starnes. Shell buckling design criteria based on manufacturing imperfection signatures. In *AIAA Journal*, volume 44, pages 654–663, 3 2006. doi:10.2514/1.5429.

[42] M. W. Hilburger, W. A. Waters, and W. T. Haynie. Buckling test results from the 8-foot-diameter orthogrid-stiffened cylinder test article ta01. Technical report, NASA, 2015. URL `https://ntrs.nasa.gov/citations/20150017037`.

[43] M. W. Hilburger, M. C. Lindell, W. A. Waters, and N. W. Gardner. Test and analysis of buckling-critical stiffened metallic launch vehicle cylinders. In *2018 AIAA/ASCE/AHS/ASC Structures, Structural Dynamics, and Materials Conference*. American Institute of Aeronautics and Astronautics, 1 2018. ISBN 978-1-62410-532-6. doi:10.2514/6.2018-1697.

[44] J. Horák, G. J. Lord, and M. A. Peletier. Cylinder buckling: The mountain pass as an organizing center. *SIAM Journal on Applied Mathematics*, 66(5):1793–1824, 2006. doi:10.1137/050635778.

[45] J. Hutchinson and J. Frauenthal. Elastic postbuckling behavior of stiffened and barreled cylindrical shells. *Journal of Applied Mechanics*, 1969.

[46] D. K. Huzel and D. H. H. Huang. Design of liquid propellant rocket engines nasa sp-125. Technical report, NASA, 7 1971.

[47] C. Hühne, R. Rolfes, E. Breitbach, and J. Teßmer. Robust design of composite cylindrical shells under axial compression - simulation and validation. *Thin-Walled Structures*, 46:947–962, 7 2008. ISSN 02638231. doi:10.1016/j.tws.2008.01.043.

[48] iStock by Getty Images. Elephant leg isolated, n.d. URL `https://www.istockphoto.com/nl/foto/elephant-leg-isolated-gm178885792-25252241`. Accessed: 08.12.2025.

[49] H.-I. Kim, C.-H. Sim, J.-S. Park, K. Lee, J.-T. Yoo, and Y.-H. Yoon. Derivation of buckling knockdown factors using the equivalent model for isogrid-stiffened cylinders. In *Proceeding of the 8th European Conference for Aeronautics and Space Sciences*, 2019.

[50] H. I. Kim, C. H. Sim, J. S. Park, K. Lee, J. T. Yoo, and Y. H. Yoon. Numerical derivation of buckling knockdown factors for isogrid-stiffened cylinders with various shell thickness ratios. *International Journal of Aerospace Engineering*, 2020, 2020. ISSN 16875974. doi:10.1155/2020/9851984.

[51] W. T. Koiter. A translation of "the stability of elastic equilibrium". Technical Report AFFDL-TR-70-25, Air Force Flight Dynamics Laboratory, Air Force Systems Command, Wright–Patterson Air Force Base, Ohio, 1970. DTIC Accession Number: AD704124. Sponsored by Lockheed Missiles & Space Company, Sunnyvale, California. Distribution unlimited.

[52] T. K. Koo and M. Y. Li. A guideline of selecting and reporting intraclass correlation coefficients for reliability research. *Journal of Chiropractic Medicine*, 15(2):155–163, 2016. doi:10.1016/j.jcm.2016.02.012. URL `https://pmc.ncbi.nlm.nih.gov/articles/PMC4913118/`.

[53] B. Kriegesmann, M. Hilburger, and R. Rolfes. The effects of geometric and loading imperfections on the response and lower-bound buckling load of a compression-loaded cylindrical shell. In *53rd AIAA/ASME/ASCE/AHS/ASC Structures, Structural Dynamics and Materials ConferenceBR 20th AIAA/ASME/AHS Adaptive Structures ConferenceBR 14th AIAA*. American Institute of Aeronautics and Astronautics, 4 2012. ISBN 978-1-60086-937-2. doi:10.2514/6.2012-1864.

[54] P. Legendre. Species associations: The Kendall coefficient of concordance revisited. *Journal of Agricultural, Biological, and Environmental Statistics*, 10(2):226–245, 6 2005. ISSN 10857117. doi:10.1198/108571105X46642.

[55] Z. Li, Y. Cao, and G. Pan. Influence of geometric imperfections on the axially loaded composite conical shells with and without cutout. *AIP Advances*, 10, 9 2020. ISSN 21583226. doi:10.1063/5.0021103.

[56] D. Liljequist, B. Elfving, and K. S. Roaldsen. Intraclass correlation – a discussion and demonstration of basic features. *PLoS ONE*, 14, 7 2019. ISSN 19326203. doi:10.1371/journal.pone.0219854.

[57] A. Lovejoy, M. Hilburger, and P. Chunchu. Effects of Buckling-Knockdown Factor, Internal Pressure and Material on the Design of Stiffened Cylinders. In *51st AIAA/ASME/ASCE/AHS/ASC Structures, Structural Dynamics, and Materials Conference
 18th AIAA/ASME/AHS Adaptive Structures Conference
 12th*, Reston, Virigina, 4 2010. American Institute of Aeronautics and Astronautics. ISBN 978-1-60086-961-7. doi:10.2514/6.2010-2778.

[58] A. E. Lovejoy, M. W. Hilburger, and N. W. Gardner. Test and analysis of full-scale 27.5-foot-diameter stiffened metallic launch vehicle cylinders. In *2018 AIAA/ASCE/AHS/ASC Structures, Structural Dynamics, and Materials Conference*. American Institute of Aeronautics and Astronautics, 1 2018. ISBN 978-1-62410-532-6. doi:10.2514/6.2018-1989.

[59] P. K. Malhotra, T. Wenk, and M. Wieland. Simple procedure for seismic analysis of liquid-storage tanks. *Structural Engineering International: Journal of the International Association for Bridge and Structural Engineering (IABSE)*, 10:197–201, 2000. ISSN 10168664. doi:10.2749/101686600780481509.

[60] K. O. McGraw and S. P. Wong. Forming inferences about some intraclass correlation coefficients. *Psychological Methods*, 1:30–46, 3 1996. doi:10.1037/1082-989X.1.1.30.

[61] S. Miladi and M. S. Razzaghi. A parametric study on inelastic buckling in steel cylindrical shells with circular cutouts. *International Journal of Advanced Structural Engineering*, 6, 3 2014. ISSN 20086695. doi:10.1007/s40091-014-0047-4.

[62] P. Mishra, C. M. Pandey, U. Singh, A. Gupta, C. Sahu, and A. Keshri. Descriptive statistics and normality tests for statistical data. *Annals of Cardiac Anaesthesia*, 22(1):67–72, 2019. doi:10.4103/aca.ACA_157_18. URL `https://doi.org/10.4103/aca.ACA_157_18`.

[63] M. S. Nair, D. Sathyan, and K. A. Jose. Design of a typical aerospace interstage structure using orthogrid/waffle configuration. *Materials Today: Proceedings*, 5 2023. ISSN 22147853. doi:10.1016/j.matpr.2023.05.082.

[64] M. P. Nemeth, R. D. Young, T. J. Collins, and J. H. Starnes. Effects of welding-induced imperfections on behavior of space shuttle superlightweight tank. *Journal of Spacecraft and Rockets*, 36:812–819, 1999. ISSN 00224650. doi:10.2514/2.3519.

[65] S. F. Newman, K. M. Taminger, M. Domack, and W. Tayon. Development and characterization of the integrally stiffened cylinder (isc) process. Technical report, NASA Langley Research Center, 5 2020. URL `https://ntrs.nasa.gov/citations/20200005462`.

[66] A. C. Orifici and C. Bisagni. Perturbation-based imperfection analysis for composite cylindrical shells buckling in compression. *Composite Structures*, 106:520–528, 12 2013. ISSN 02638223. doi:10.1016/j.compstruct.2013.06.028.

[67] L. G. Portney, M. P. Watkins, et al. *Foundations of clinical research: applications to practice*, volume 892. Pearson/Prentice Hall Upper Saddle River, NJ, 2009.

[68] J. M. Rotter. Elephant's foot buckling in pressurised cylindrical shells. *Stahlbau*, 75:742–747, 9 2006. ISSN 00389145. doi:10.1002/stab.200610079.

[69] M. T. Rudd, M. W. Hilburger, A. E. Lovejoy, M. C. Lindell, N. W. Gardner, and M. R. Schultz. Buckling response of a large-scale, seamless, orthogrid-stiffened metallic cylinder. In *2018 AIAA/ASCE/AHS/ASC Structures, Structural Dynamics, and Materials Conference*, page 1987, 2018.

[70] H. Schmidt. Stability of steel shell structures. *Journal of Constructional Steel Research*, 55:159–181, 7 2000. ISSN 0143974X. doi:10.1016/S0143-974X(99)00084-X.

[71] SciPy Developers. scipy.optimize.curve_fit, 2025. URL `https://docs.scipy.org/doc/scipy/reference/generated/scipy.optimize.curve_fit.html`. Accessed: 25.11.2025.

[72] O. Shechtman. *The Coefficient of Variation as an Index of Measurement Reliability*, pages 39–49. Springer, 5 2013. ISBN 978-3-642-37131-8. doi:10.1007/978-3-642-37131-8_4.

[73] P. E. Shrout and J. L. Fleiss. Intraclass correlations: Uses in assessing rater reliability. *Psychological Bulletin*, 86:420–428, 1979. ISSN 1939-1455. doi:10.1037/0033-2909.86.2.420.

[74] C. H. Sim, H. I. Kim, Y. L. Lee, J. S. Park, and K. Lee. Derivations of Knockdown Factors for Cylindrical Structures Considering Different Initial Imperfection Models and Thickness Ratios. *International Journal of Aeronautical and Space Sciences*, 19(3):626–635, 9 2018. ISSN 20932480. doi:10.1007/s42405-018-0069-4.

[75] C. H. Sim, H. I. Kim, J. S. Park, and K. Lee. Derivation of knockdown factors for grid-stiffened cylinders considering various shell thickness ratios. *Aircraft Engineering and Aerospace Technology*, 91(10):1314–1326, 10 2019. ISSN 17488842. doi:10.1108/AEAT-11-2018-0272.

[76] C. H. Sim, D. Y. Kim, J. S. Park, J. T. Yoo, Y. H. Yoon, and K. Lee. Derivation of Buckling Knockdown Factors for Pressurized Orthogrid-Stiffened Cylinders of Launch Vehicle Structures. *International Journal of Aeronautical and Space Sciences*, 24(5):1295–1310, 11 2023. ISSN 20932480. doi:10.1007/s42405-023-00621-4.

[77] C. H. Sim, D. Y. Kim, M. H. Jeon, J. S. Park, I. G. Kim, J. T. Yoo, Y. H. Yoon, and K. Lee. Investigation of buckling knockdown factors for pressurized metallic cylinders using various numerical modeling techniques of initial imperfections. *International Journal of Aeronautical and Space Sciences*, 25:698–715, 4 2024. ISSN 20932480. doi:10.1007/s42405-023-00667-4.

[78] E. M. Sosa, L. A. Godoy, and J. G. Croll. Computation of lower-bound elastic buckling loads using general-purpose finite element codes. *Computers and Structures*, 84:1934–1945, 11 2006. ISSN 00457949. doi:10.1016/j.compstruc.2006.08.016.

[79] G. Speicher and H. Saal. Numerical calculation of limit loads for shells of revolution with particular regard to the applying equivalent initial imperfection. *in Buckling of Shell Structure, on Land, in the Sea, and in the Air*, pages 466–475, 1991.

[80] Statsmodels Developers. Statsmodels api documentation, 2025. URL `https://www.statsmodels.org/stable/api.html`. Accessed: 28.11.2025.

[81] Statsmodels Developers. Breusch–pagan test for heteroscedasticity, 2025. URL `https://www.statsmodels.org/stable/generated/statsmodels.stats.diagnostic.het_breuschpagan.html`. Accessed: 08.12.2025.

[82] R. P. Thornburgh and M. W. Hilburger. Longitudinal Weld Land Buckling in Compression-Loaded Orthogrid Cylinders. Technical report, NASA Langley Research Center, 12 2010. URL `https://ntrs.nasa.gov/citations/20110004012`.

[83] R. P. Thornburgh and M. W. Hilburger. Pre-test analysis predictions for the shell buckling knockdown factor checkout tests-TA01 and TA02. Technical report, National Aeronautics and Space Administration, 1 2011. URL `https://ntrs.nasa.gov/api/citations/20110004286/downloads/20110004286.pdf`.

[84] K. Tian, B. Wang, P. Hao, and A. M. Waas. A high-fidelity approximate model for determining lower-bound buckling loads for stiffened shells. *International Journal of Solids and Structures*, 148-149:14–23, 9 2018. ISSN 00207683. doi:10.1016/j.ijsolstr.2017.10.034.

[85] R. Vallat. *pingouin.intraclass_corr — Pingouin statistical package documentation*, 2023. URL `https://pingouin-stats.org/build/html/generated/pingouin.intraclass_corr.html`. Accessed: 08.12.2025.

[86] W. V.L., P. Seide, and J. Peterson. Buckling of thin-walled circular cylinders. Technical report, NASA Langley Research Center, 9 1965.

[87] W. V.L., P. Seide, J. Peterson, and M. Hilburger. Buckling of thin-walled circular cylinders. Technical report, NASA Langley Research Center, 2020. URL `http12s://ntrs.nasa.gov/citations/20205011530`.

[88] H. N. Wagner and C. Hühne. Robust knockdown factors for the design of cylindrical shells under axial compression: potentials, practial application and reliability analysis. *International Journal of Mechanical Sciences*, 135:410–430, 1 2018. ISSN 00207403. doi:10.1016/j.ijmecsci.2017.11.020.

[89] H. N. Wagner, C. Hühne, and S. Niemann. Robust knockdown factors for the design of axially loaded cylindrical and conical composite shells – Development and Validation. *Composite Structures*, 173:281–303, 8 2017. ISSN 02638223. doi:10.1016/j.compstruct.2017.02.031.

[90] H. N. Wagner, C. Hühne, and S. Niemann. Robust knockdown factors for the design of axially loaded cylindrical and conical composite shells – development and validation. *Composite Structures*, 173:281–303, 8 2017. ISSN 02638223. doi:10.1016/j.compstruct.2017.02.031.

[91] H. N. Wagner, C. Hühne, S. Niemann, and R. Khakimova. Robust design criterion for axially loaded cylindrical shells - simulation and validation. *Thin-Walled Structures*, 115:154–162, 6 2017. ISSN 02638231. doi:10.1016/j.tws.2016.12.017.

[92] H. N. Wagner, C. Hühne, K. Rohwer, S. Niemann, and M. Wiedemann. Stimulating the realistic worst case buckling scenario of axially compressed unstiffened cylindrical composite shells. *Composite Structures*, 160:1095–1104, 1 2017. ISSN 02638223. doi:10.1016/j.compstruct.2016.10.108.

[93] H. N. Wagner, C. Hühne, S. Niemann, K. Tian, B. Wang, and P. Hao. Robust knockdown factors for the design of cylindrical shells under axial compression: Analysis and modeling of stiffened and unstiffened cylinders. *Thin-Walled Structures*, 127:629–645, 6 2018. ISSN 02638231. doi:10.1016/j.tws.2018.01.041.

[94] H. N. Wagner, C. Hühne, and S. Niemann. Buckling of launch-vehicle cylinders under axial compression: A comparison of experimental and numerical knockdown factors. *Thin-Walled Structures*, 155, 10 2020. ISSN 02638231. doi:10.1016/j.tws.2020.106931.

[95] R. Wagner. Abaqus tutorial: Non-linear buckling analysis of a full-scale launch-vehicle cylinder under combined loading, 10 2020. URL `https://www.researchgate.net/publication/344445604_ABAQUS_Tutorial_Non-linear_buckling_analysis_of_a_full-scale_launch-vehicle_cylinder_under_combined_loading`. Accessed: 12.12.2024.

[96] R. Wagner. Abaqus tutorial: Load controlled vs displacement controlled buckling analysis and shell-edge warpege, 2021. URL `https://www.bilibili.com/video/BV15K4y1R7vW/?vd_source=72eee40569225048d242170de1e6b8c2`. Accessed: 10.10.2025.

[97] B. Wang, P. Hao, G. Li, Y. Fang, X. Wang, and X. Zhang. Determination of realistic worst imperfection for cylindrical shells using surrogate model. *Structural and Multidisciplinary Optimization*, 48:777–794, 10 2013. ISSN 16151488. doi:10.1007/s00158-013-0922-9.

[98] B. Wang, K. Du, P. Hao, C. Zhou, K. Tian, S. Xu, Y. Ma, and X. Zhang. Numerically and experimentally predicted knockdown factors for stiffened shells under axial compression. *Thin-Walled Structures*, 109: 13–24, 12 2016. ISSN 02638231. doi:10.1016/j.tws.2016.09.008.

[99] B. Wang, X. Ma, P. Hao, Y. Sun, K. Tian, G. Li, K. Zhang, L. Jiang, and J. Guo. Improved knockdown factors for composite cylindrical shells with delamination and geometric imperfections. *Composites Part B: Engineering*, 163:314–323, 4 2019. ISSN 13598368. doi:10.1016/j.compositesb.2018.11.049.

[100] S. C. White, P. M. Weaver, and K. C. Wu. Post-buckling analyses of variable-stiffness composite cylinders in axial compression. *Composite Structures*, 123:190–203, 5 2015. ISSN 02638223. doi:10.1016/j.compstruct.2014.12.013.

[101] T. Winterstetter and H. Schmidt. Stability of circular cylindrical steel shells under combined loading. *Thin-Walled Structures*, 40:893–910, 10 2002. ISSN 02638231. doi:10.1016/S0263-8231(02)00006-X.

[102] C. Zaiontz. *Intraclass Correlation.* Real Statistics Using Excel, 2024. URL `https://real-statistics.com/reliability/interrater-reliability/intraclass-correlation/`. Accessed: 08.12.2025.

A

SBKF Shells Data

Table A.1: Summary of reported buckling loads for all structures.

Structure	Method	lbf/in	lbf	N	Source	Comments
TA01	Linear Buckling	2406.0	7.24×10^5	3.22×10^6	[35]	p.6
	GNA	2368.2	7.14×10^5	3.18×10^6	[35]	Figure 16, p.29
	MSI Buckling	2017.7	6.09×10^5	2.71×10^6	[35]	Figure 16, p.29
	Test Buckling	–	6.89×10^5	3.06×10^6	[42]	p.47
TA03	Linear Buckling	2416.0	7.29×10^5	3.24×10^6	[35]	p.9
	GNA	2613.0	7.88×10^5	3.51×10^6	[35]	p.10
	MSI Buckling	2446.2	7.38×10^5	3.28×10^6	[35]	Figure 20, p.33
	Test Buckling	–	–	–	–	No experimental data available
TA07	Linear Buckling	–	–	–	–	Not reported
	GNA	–	5.30×10^5	2.36×10^6	[43]	Calculated using MSI's (inc. 4.5%), p.20.
	MSI Buckling	–	5.54×10^5	2.60×10^6	[43]	p.14
	Test Buckling	–	6.47×10^5	2.88×10^6	[43]	p.13
TA09	Linear Buckling	–	–	–	–	Not reported
	GNA	–	5.85×10^5	2.60×10^6	[69]	Table 2, p.7
	MSI Buckling	–	5.09×10^5	2.26×10^6	[69]	Table 2, p.7
	Test Buckling	–	–	–	–	No experimental data available
ETTA1	Linear Buckling	565.6	5.86×10^5	2.61×10^6	[35]	p.11
	GNA	740.0	7.68×10^5	3.41×10^6	[35]	p.11
	MSI Buckling	513.7	5.33×10^5	2.37×10^6	[35]	Figure 29, p.42
	MSI Buckling at 1 psi	761.5	7.89×10^5	3.51×10^6	[35]	Figure 32, p.45
	Test Buckling at 1 psi	–	8.01×10^5	3.56×10^6	[34]	p.9-p.10

Table A.2: Geometry parameters of the investigated shells. ETTA1 height was estimated from a plot.

Structure	t_{skin} [in]	R [in]	H [in]	h_s [in]	h_r [in]	t_s [in]	t_r [in]	b_s [in]	b_r [in]	L [in]	Sources
TA01	0.10	48.0	0.400	0.300	0.300	0.100	0.100	4.000	4.000	68.750	[35, 43]
TA03	0.06	48.0	0.723	0.663	0.663	0.065	0.060	1.813	4.314	68.750	[35, 43]
TA07	0.09	48.0	0.440	0.350	0.350	0.105	0.100	2.364	4.400	68.750	[43]
TA09	0.07	48.0	0.570	0.500	0.500	0.065	0.065	2.009	4.900	68.750	[43]
ETTA1	0.09	165.0	1.050	0.960	0.960	0.090	0.100	10.800	15.320	237.000	[35, 43, 58, 95]

Table A.3: Weld land and transition region parameters of the investigated shells.

Structure	w_{weld} [in]	t_{weld} [in]	$w_{\text{trans.}}$ (axial/circ) [in]	$t_{\text{trans.}}$ [in]	Sources
TA01	1.26	0.250	1.016 / 1.688	0.160	[35, 42, 43]
TA03	1.26	0.300	1.530 / 1.333	0.100	[35, 43]
TA07	1.26	0.200	2.364 / 0.666	0.145	[43]
TA09	1.27	0.200	2.009 / 0.774	0.135	[43]
ETTA1	2.00	0.325	3.0 / 3.0 (assumed)	0.208	[37, 95]

B

Effective Thickness Calculations

The membrane and bending stiffness's for isotropic cylinders with rings and stringers were defined in [86] as presented in Equation B.1, Equation B.2.

$$\begin{aligned} A_{11} &= \frac{Et}{1-\nu^2} + \frac{E_s A_s}{b_s} \\ A_{22} &= \frac{Et}{1-\nu^2} + \frac{E_r A_r}{b_r} \end{aligned} \tag{B.1}$$

$$\begin{aligned} D_{11} &= \frac{Et^3}{12(1-\nu^2)} + \frac{E_s I_s}{b_s} + z_s^2 \frac{E_s A_s}{b_s} \\ D_{22} &= \frac{Et^3}{12(1-\nu^2)} + \frac{E_r I_r}{b_r} + z_r^2 \frac{E_r A_r}{b_r} \end{aligned} \tag{B.2}$$

The parameters E and ν refer to material Young's modulus and posisson ratio respectively. The subscript s in variabels refers to the stringer properties, wheras r to ring ones. Variables t, t_s, and t_r corressponds to cylinder, stringer and ring thciknesses. Moments of inertia I_s and I_r are dependent on the heights h_s, h_r of the stiffeners.

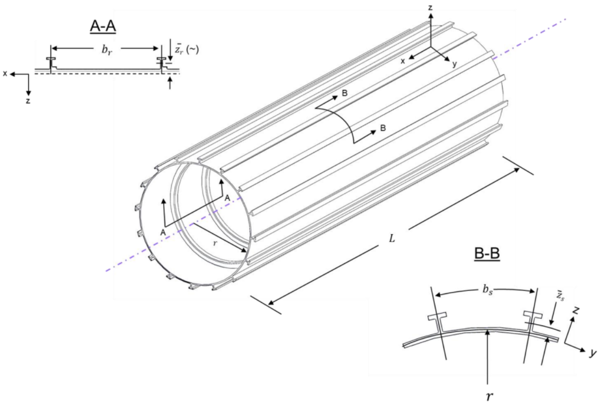

Figure B.1: Stiffened shell geometry with indicated centroid distances [87].

As the stiffeners are integrally milled the rings and stringers stiffenss moduli - E_s and E_r, are identical as the cylidner stifness E. The distance of stiffener centroid from reference surface z - (as indicated in Figure B.1), is a sum of half the acrage thickness and the stiffener height. All relations (listed in Equation B.3) were adopted from [94].

$$\begin{aligned}
A_s &= h_s \cdot t_s \\
A_r &= h_r \cdot t_s \\
I_s &= \frac{1}{12} h_s^3 t_s \\
I_r &= \frac{1}{12} h_r^3 t_s \\
z_s &= -\frac{h_s + t}{2} \\
z_r &= \frac{h_s + t}{2}
\end{aligned} \tag{B.3}$$

C

Shells’ Convergence Study

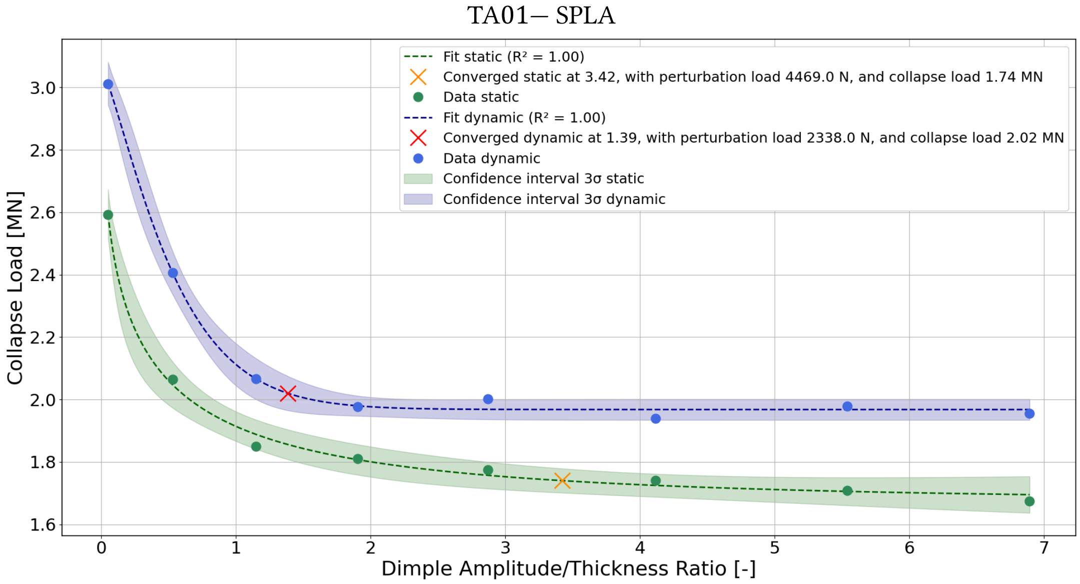

(a) 0 bar

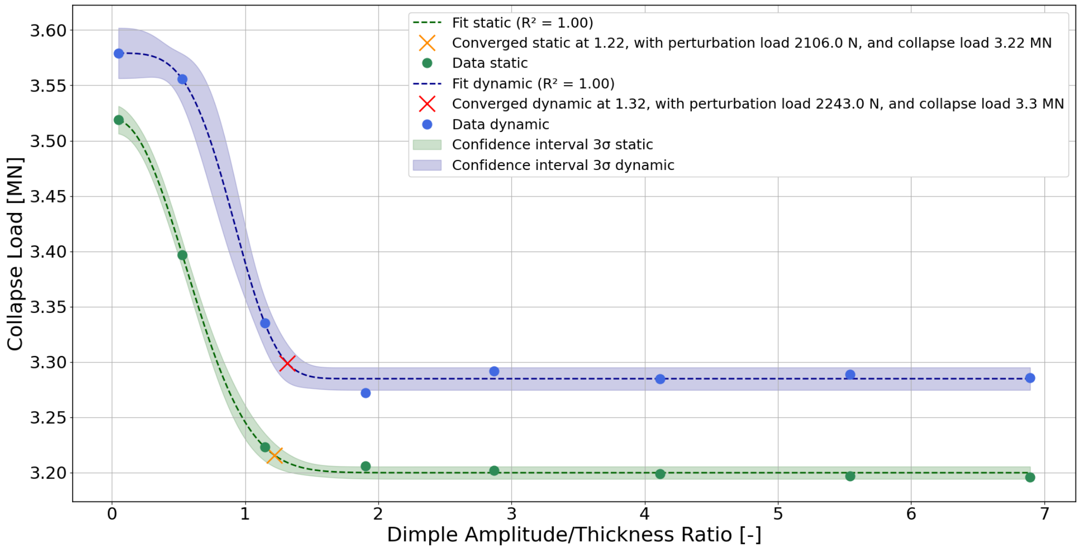

(b) 2 bar

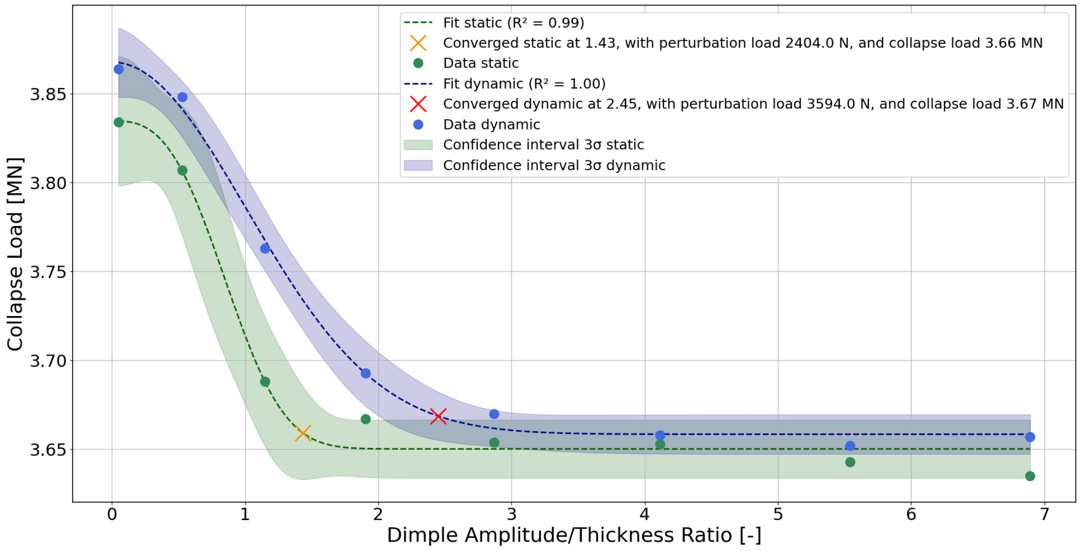

(c) 4 bar

Figure C.1: Convergence behavior of TA01 for SPLA.

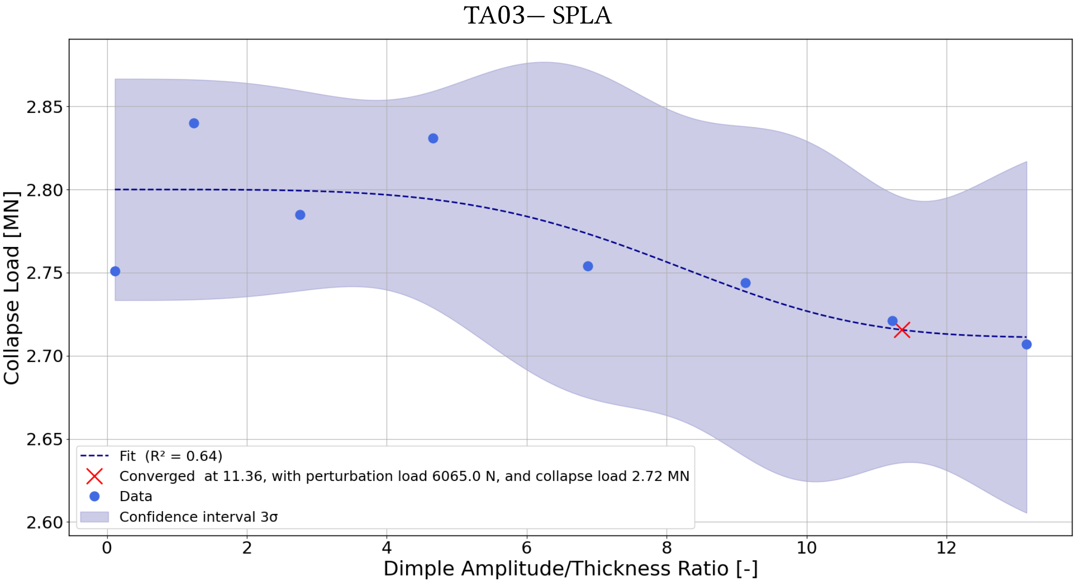
TA03— SPLA

(a) 0 bar

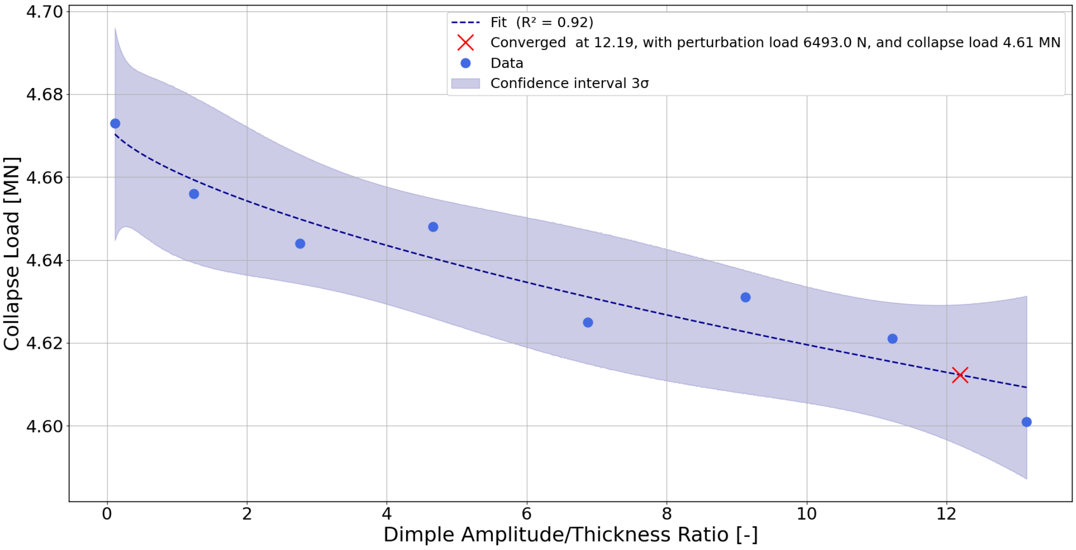

(b) 2 bar

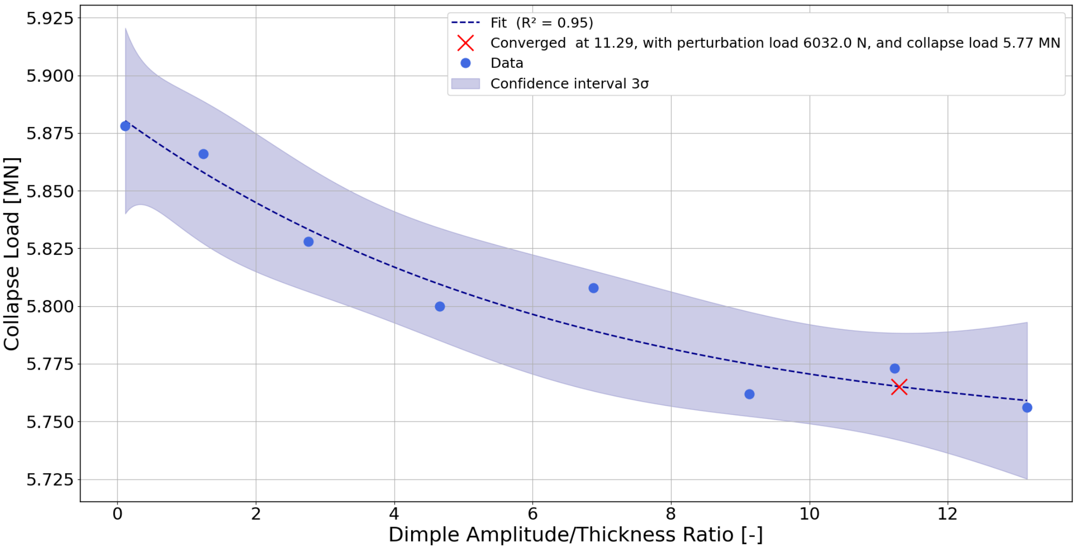

(c) 4 bar

Figure C.2: Convergence behavior of TA03 for SPLA.

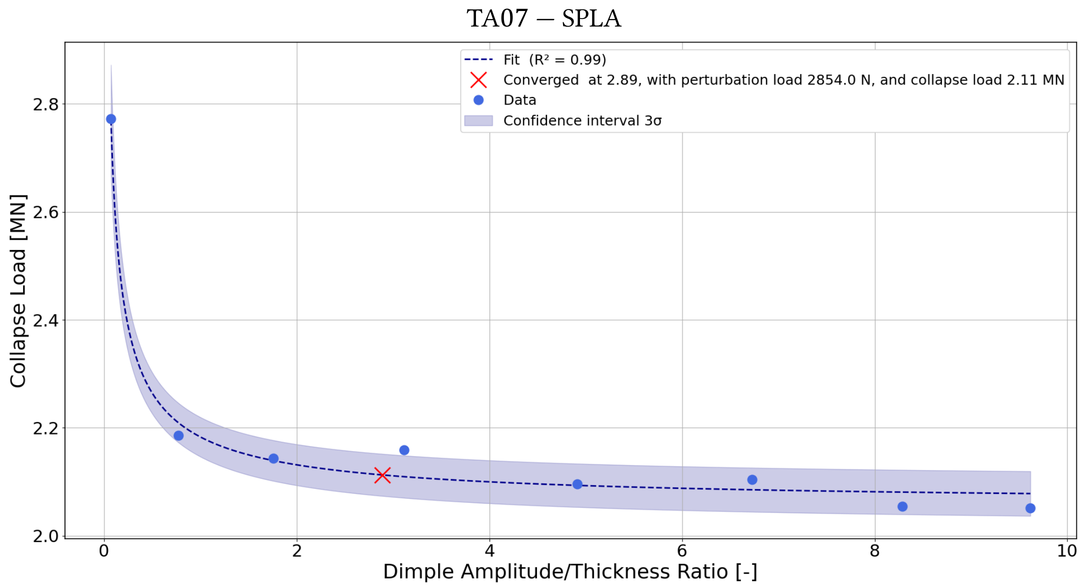

(a) 0 bar

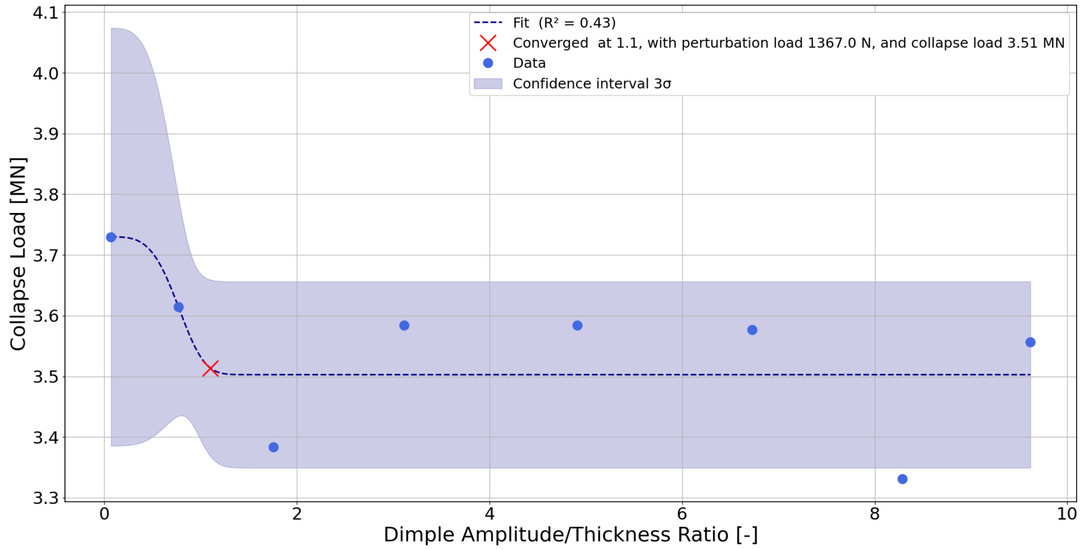

(b) 2 bar

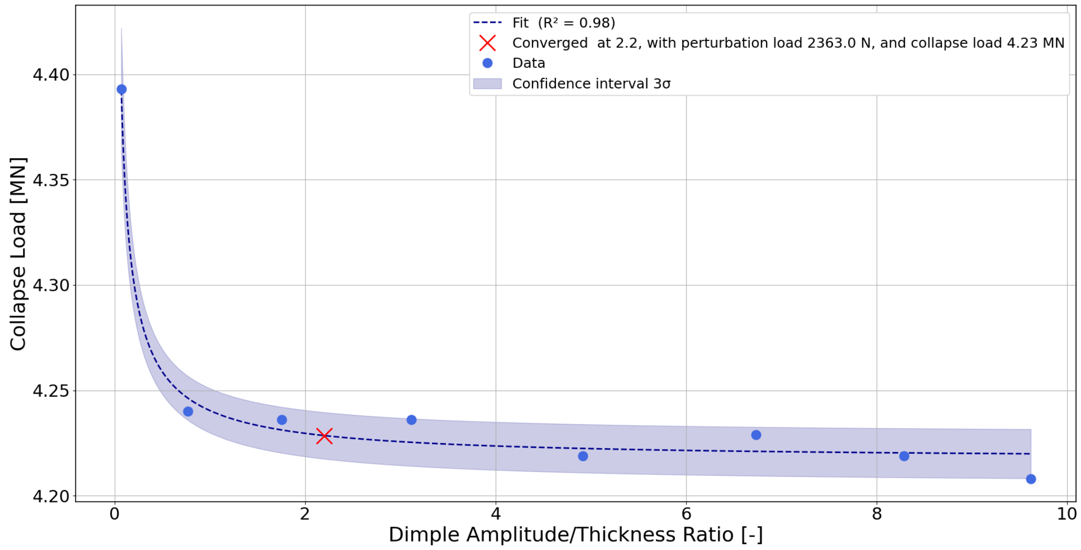

(c) 4 bar

Figure C.3: Convergence behavior of TA07 for SPLA.

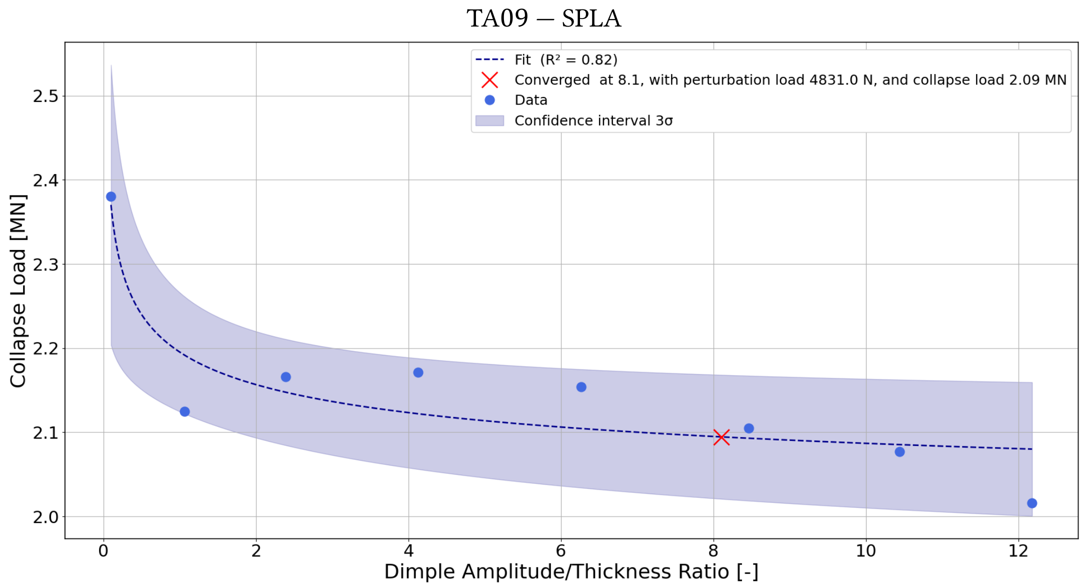

(a) 0 bar

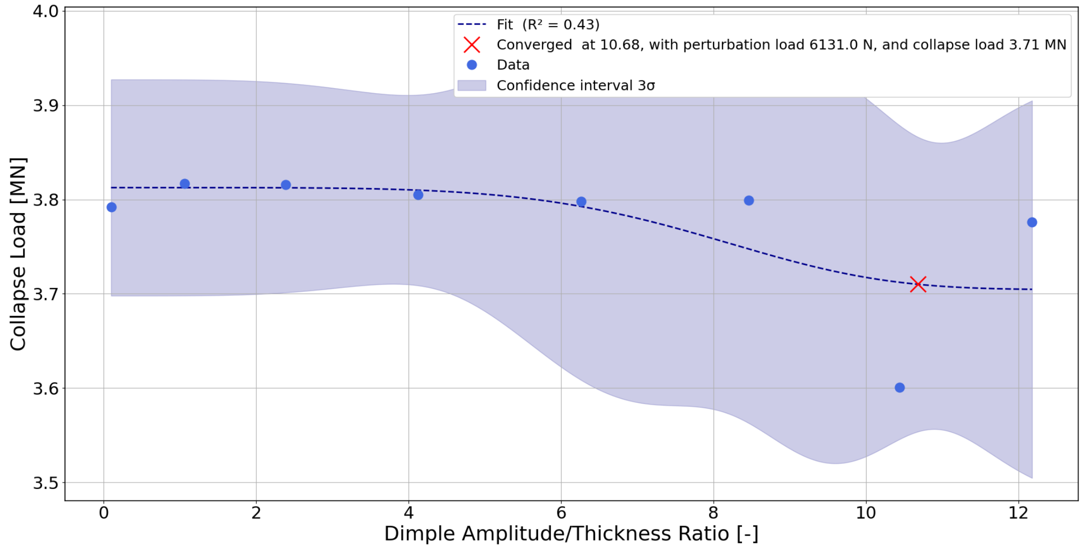

(b) 2 bar

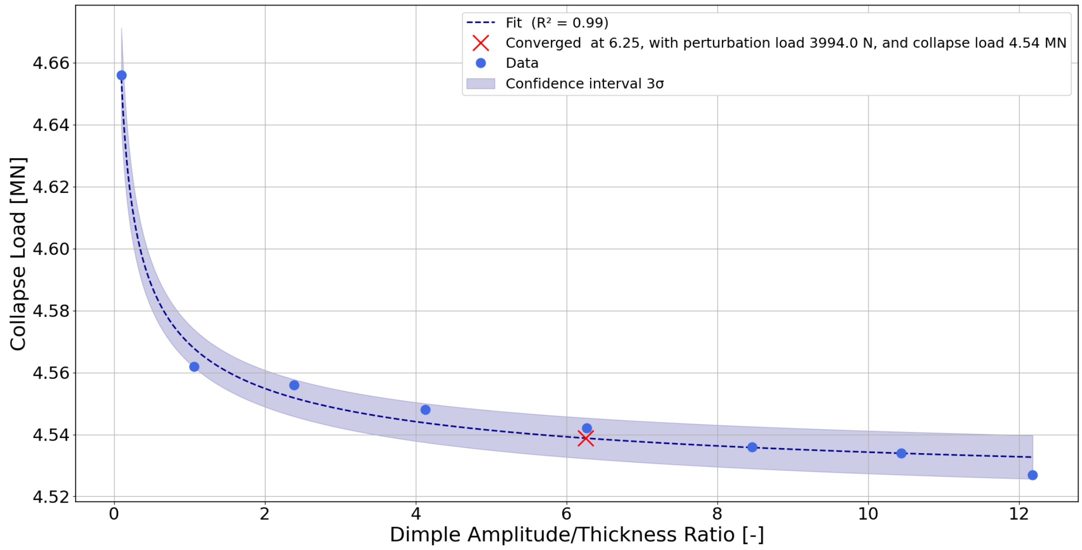

(c) 4 bar

Figure C.4: Convergence behavior of TA09 for SPLA.

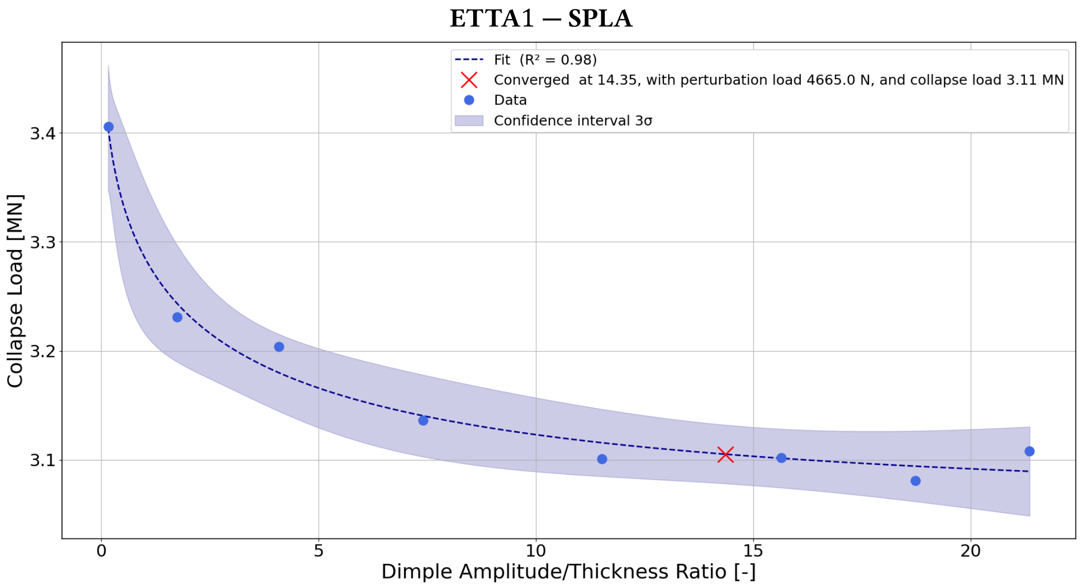

(a) 0 bar

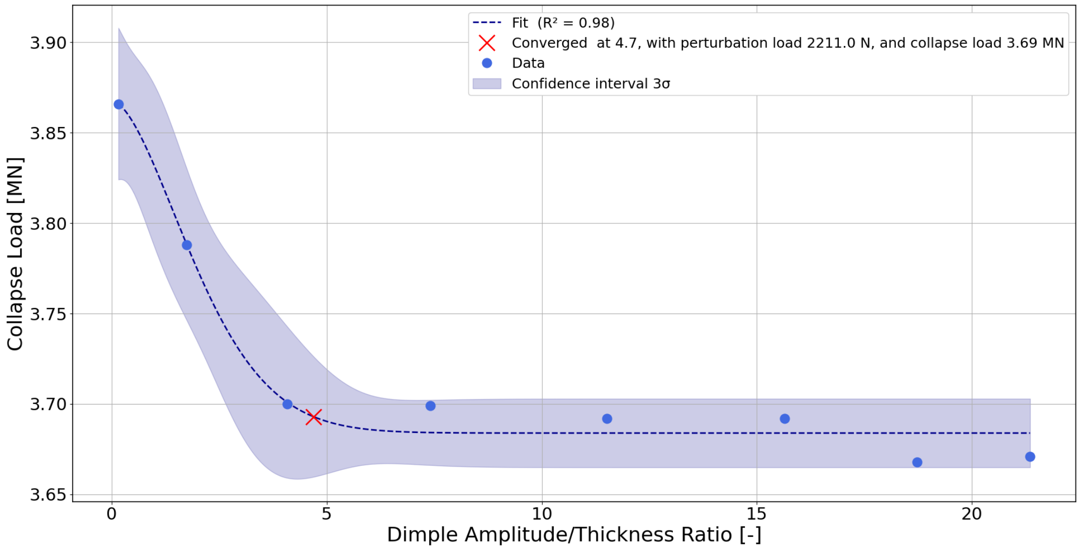

(b) 0.06895 bar

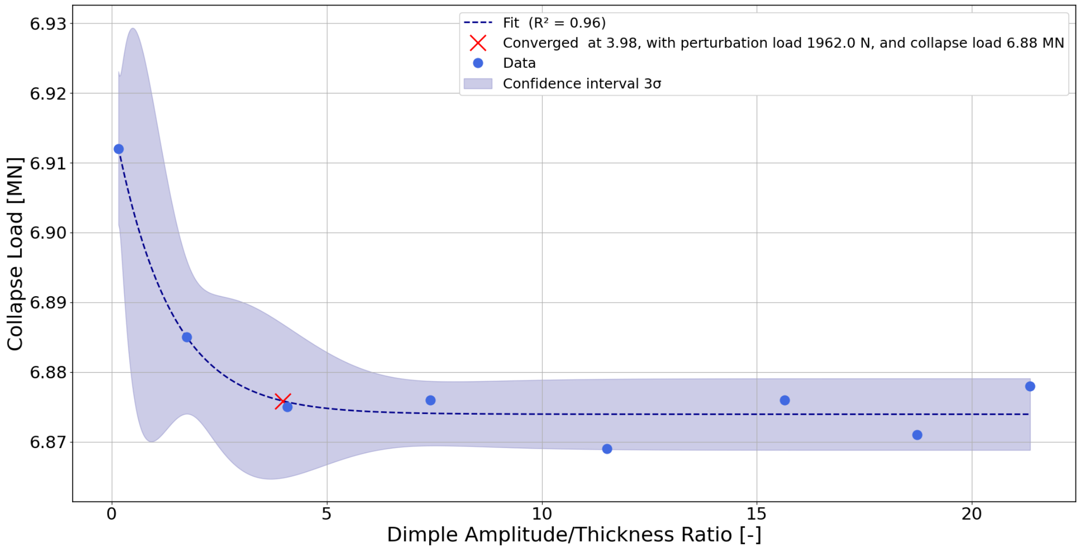

(c) 2 bar

Figure C.5: Convergence behavior of ETTA1 for SPLA.

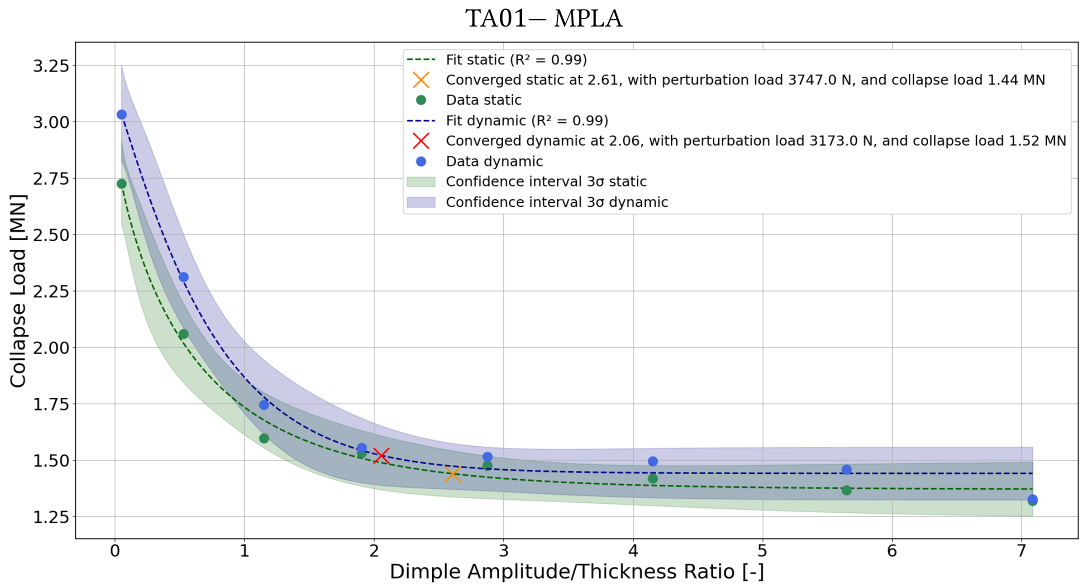

(a) 0 bar

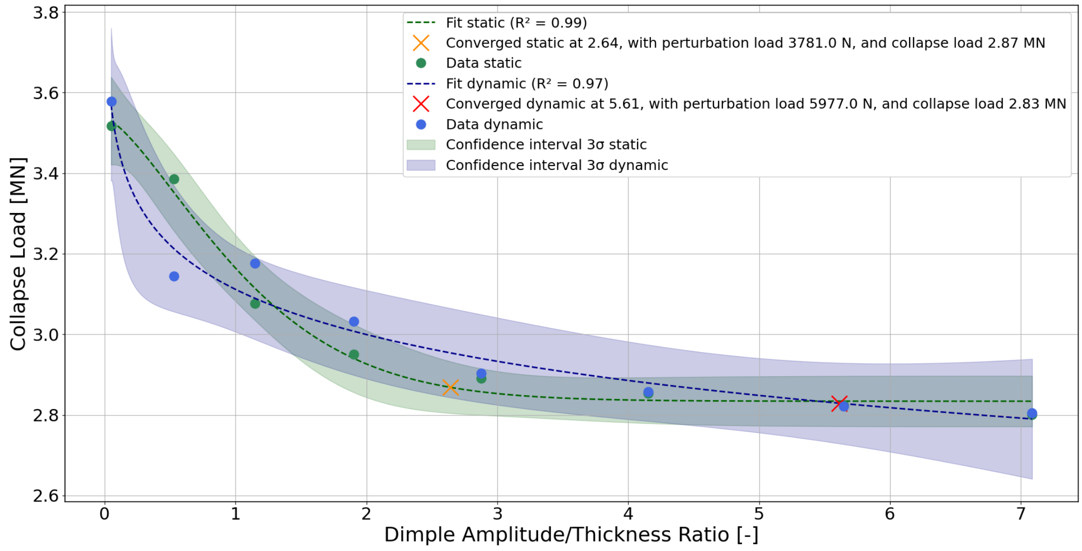

(b) 2 bar

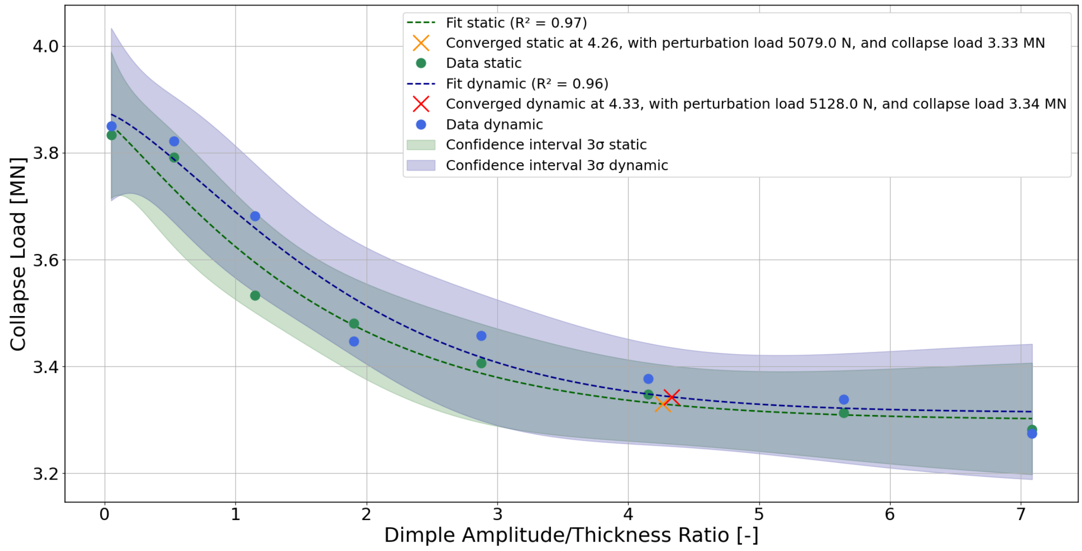

(c) 4 bar

Figure C.6: Convergence behavior of TA01 for MPLA.

TA03— MPLA

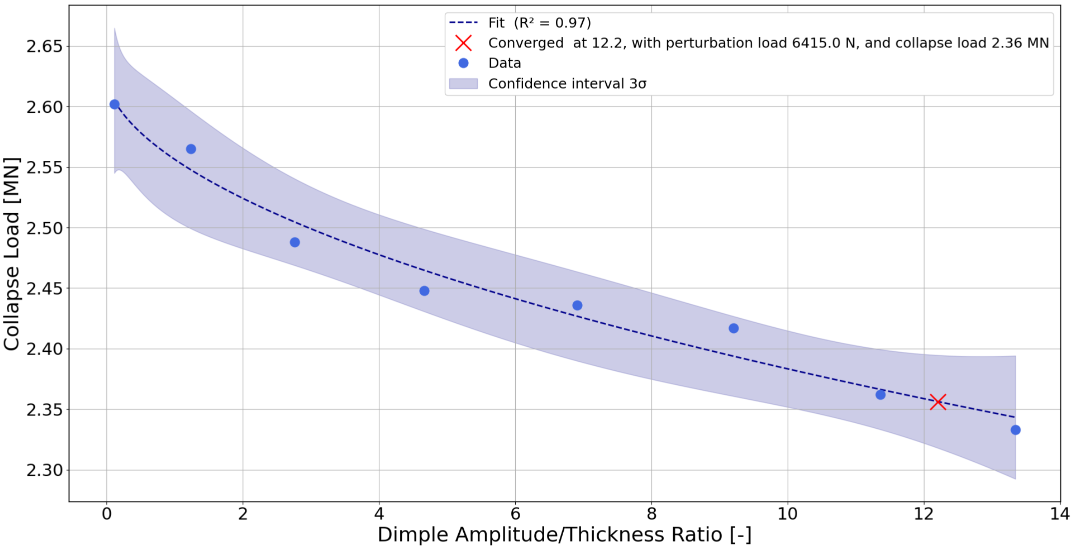

(a) 0 bar

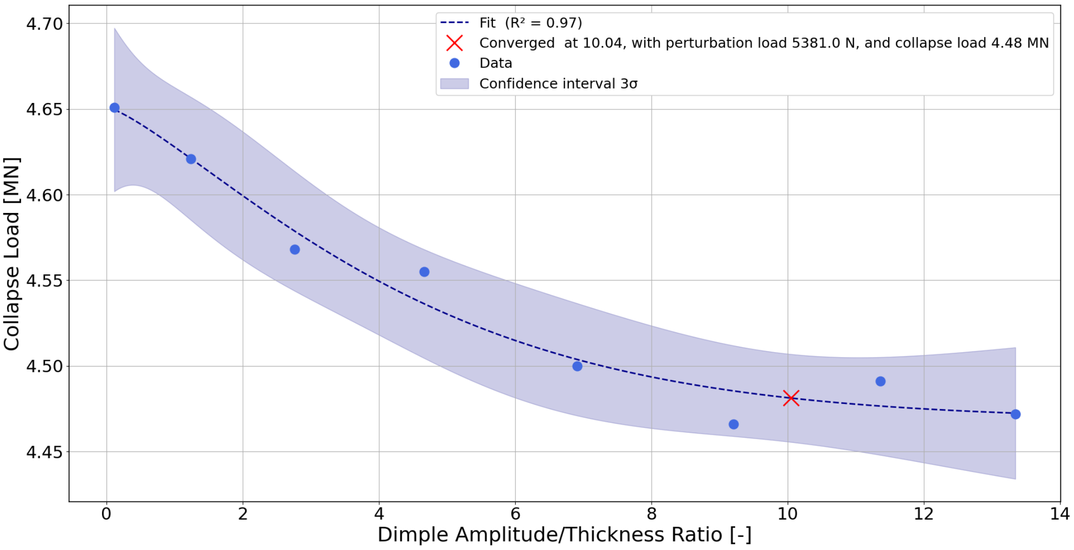

(b) 2 bar

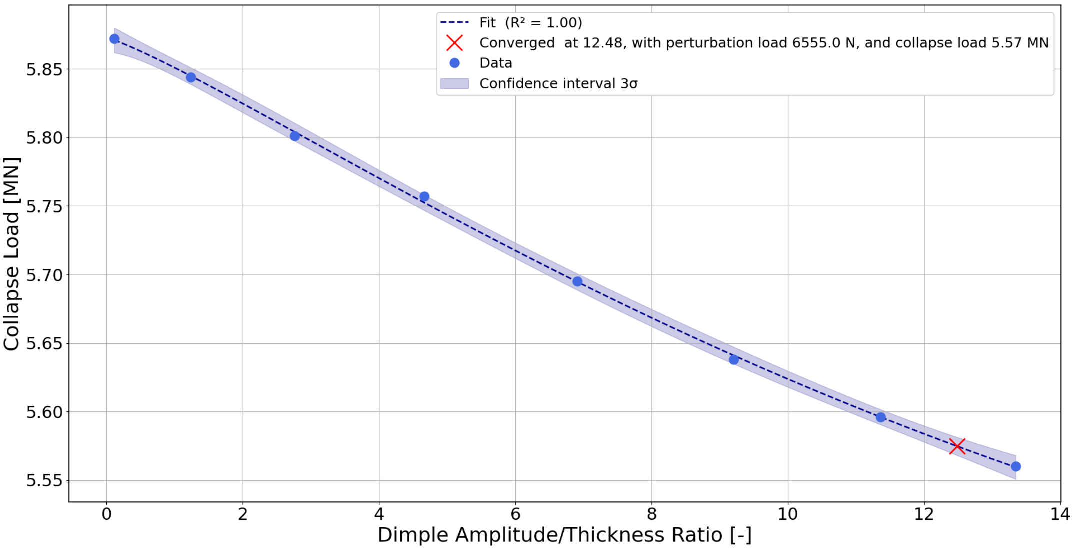

(c) 4 bar

Figure C.7: Convergence behavior of TA03 for MPLA.

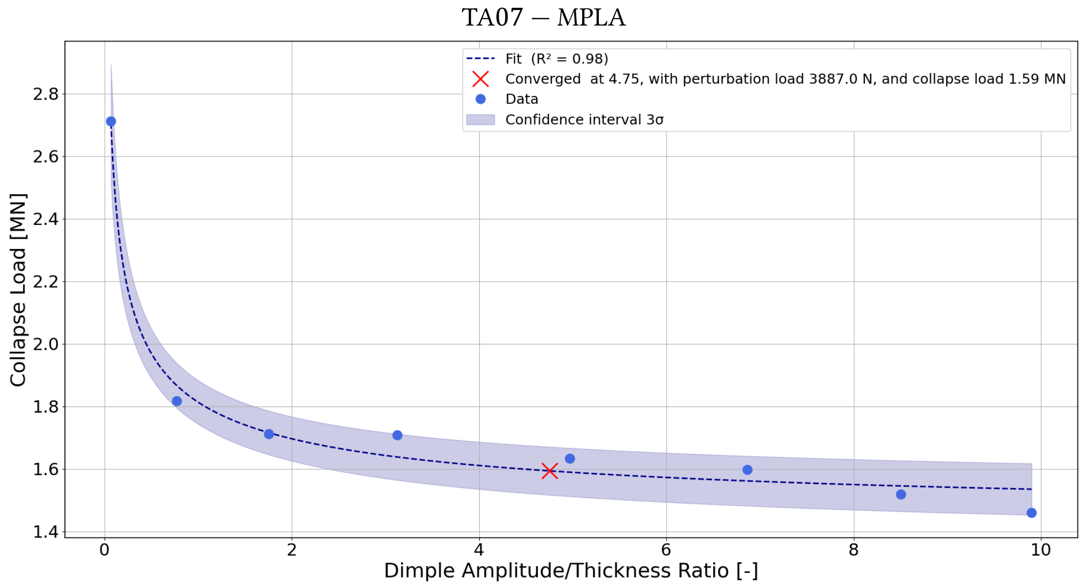

(a) 0 bar

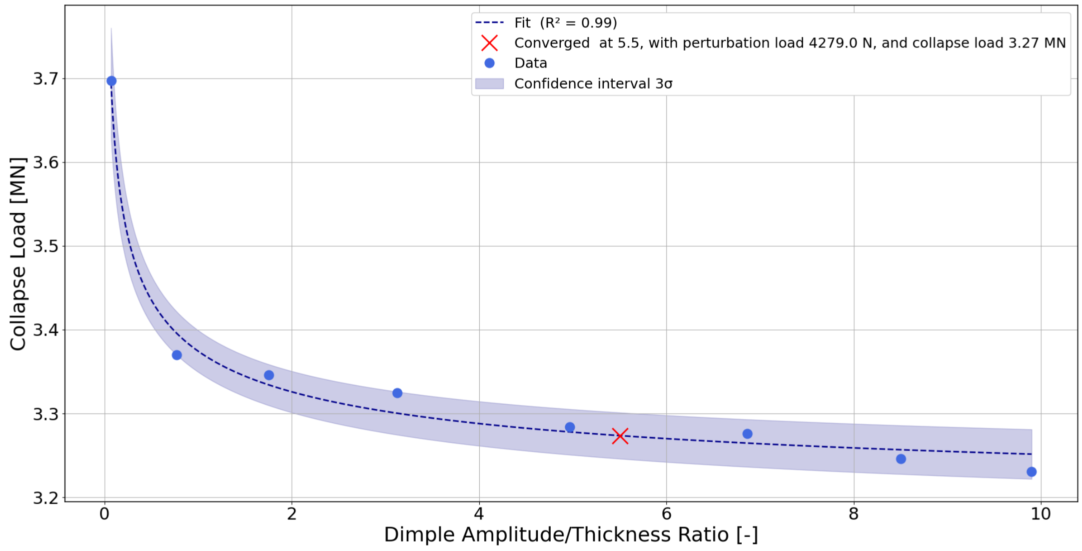

(b) 2 bar

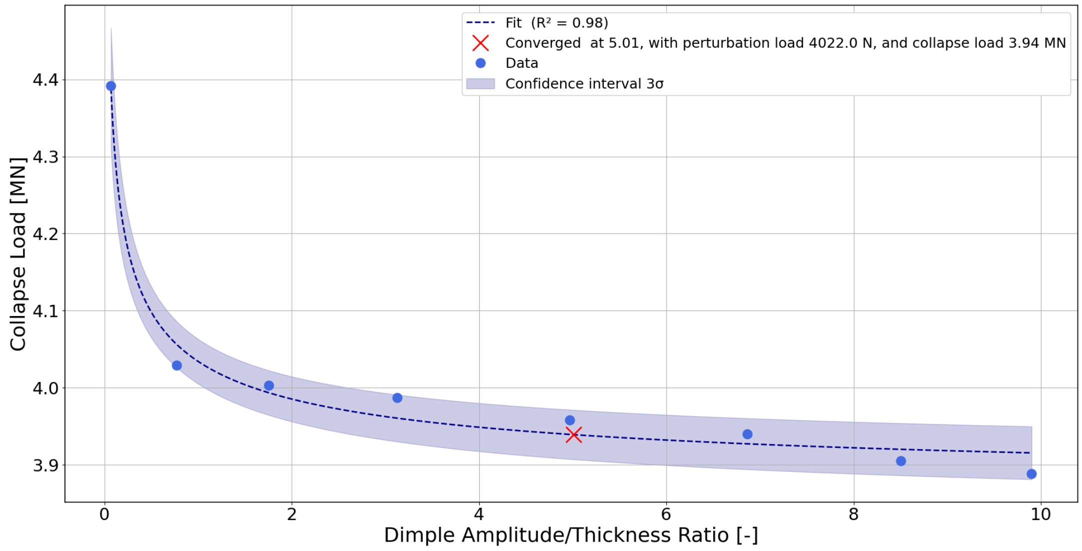

(c) 4 bar

Figure C.8: Convergence behavior of TA07 for MPLA.

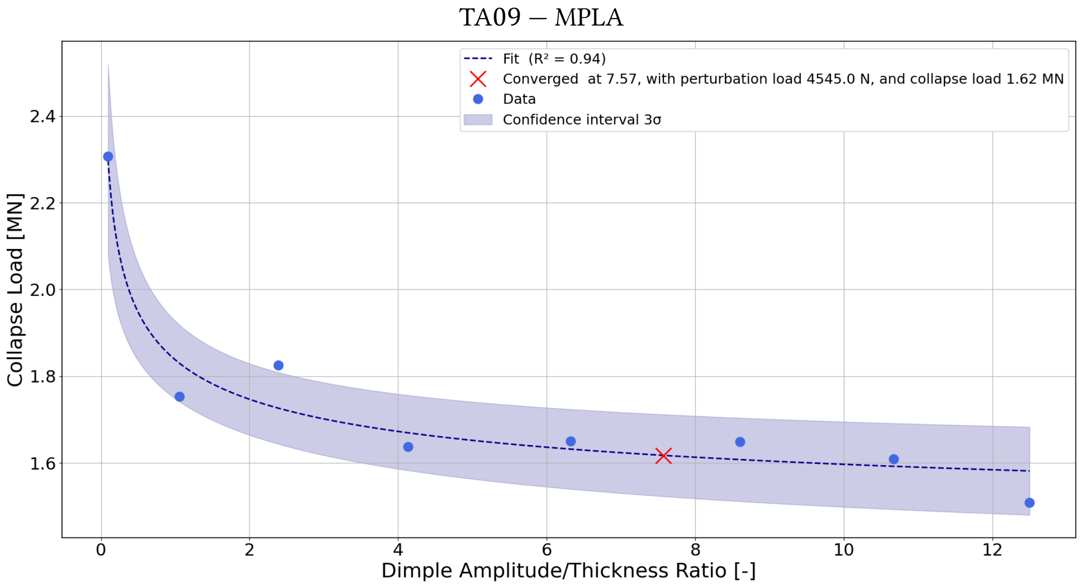

(a) 0 bar

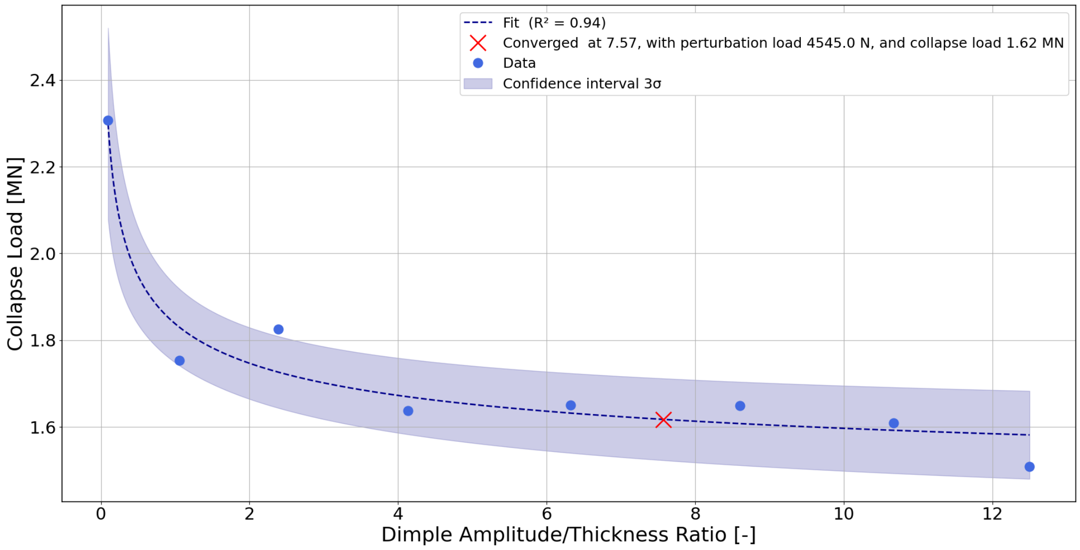

(b) 2 bar

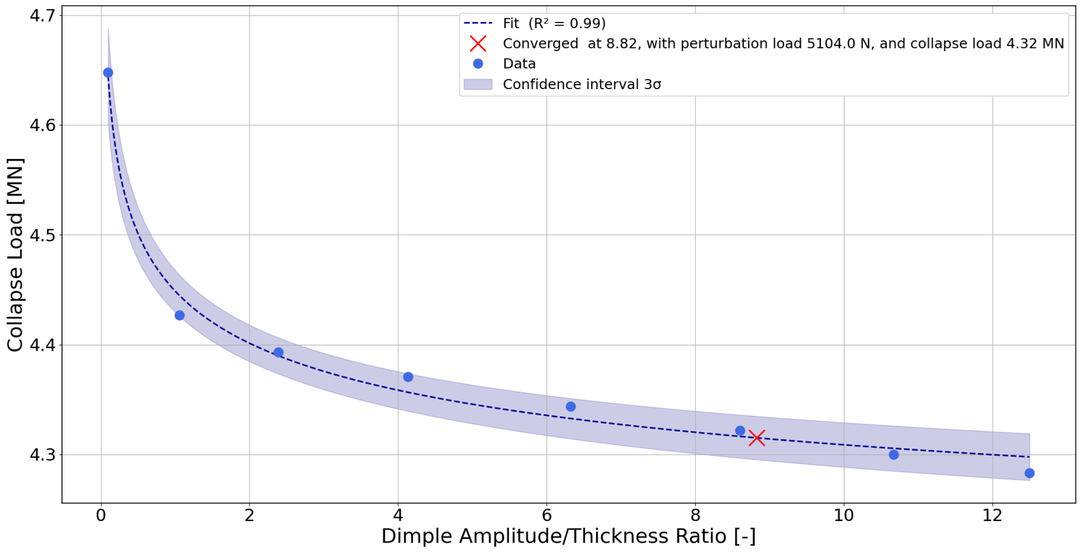

(c) 4 bar

Figure C.9: Convergence behavior of TA09 for MPLA.

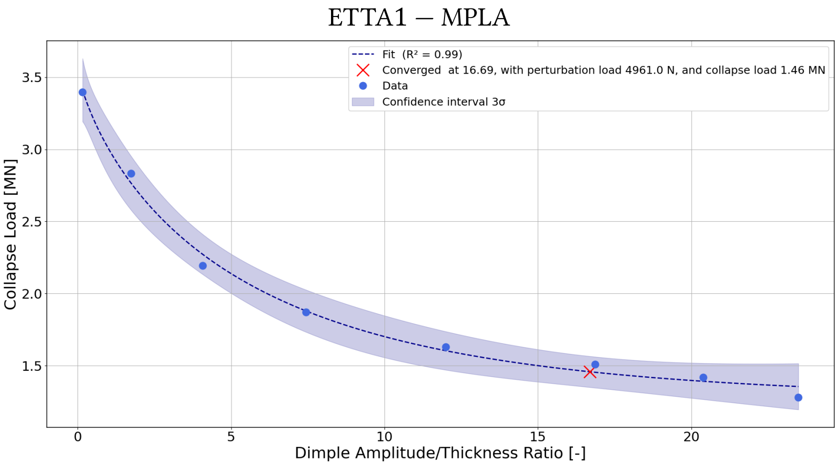

(a) 0 bar

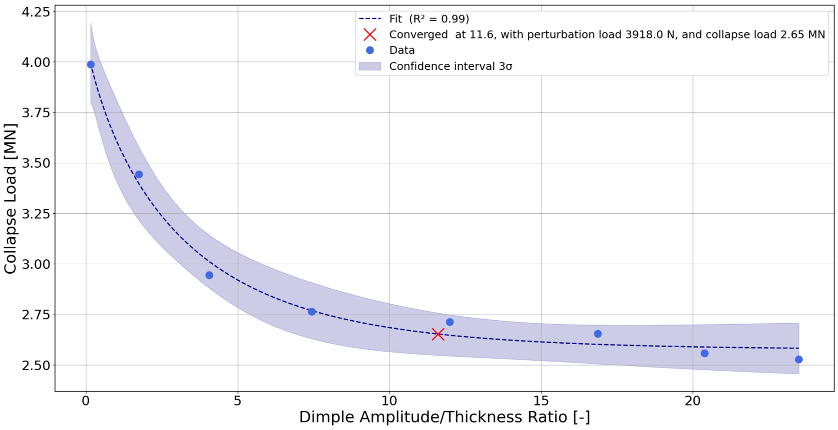

(b) 0.06895 bar

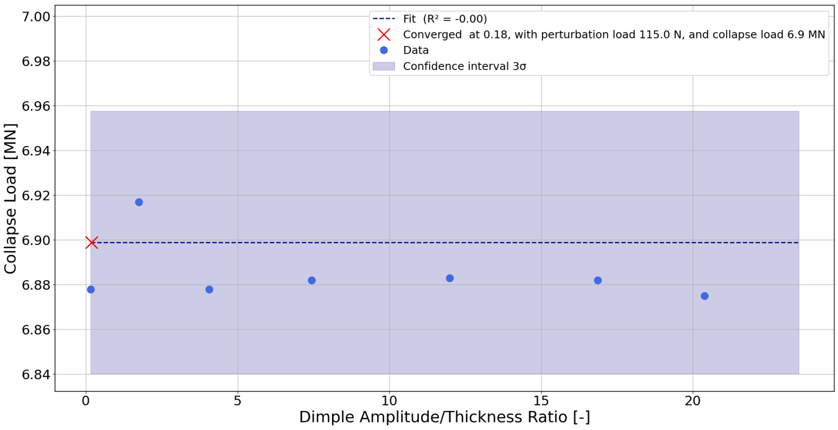

(c) 2 bar

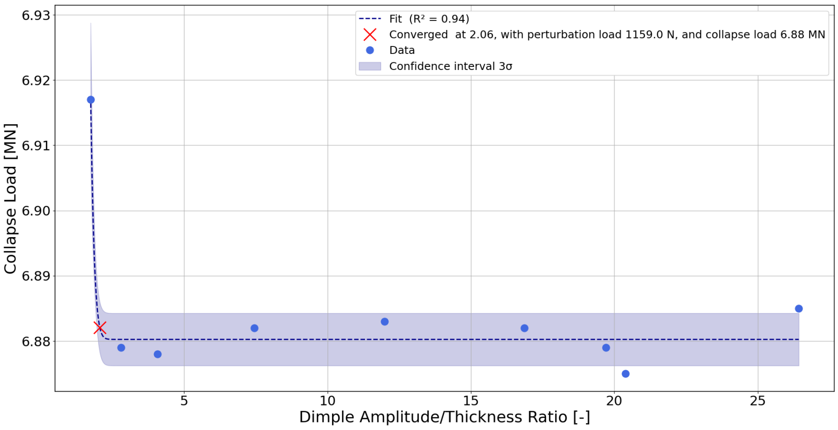

(d) 2 bar

Figure C.10: Convergence behavior of ETTA1 for MPLA.

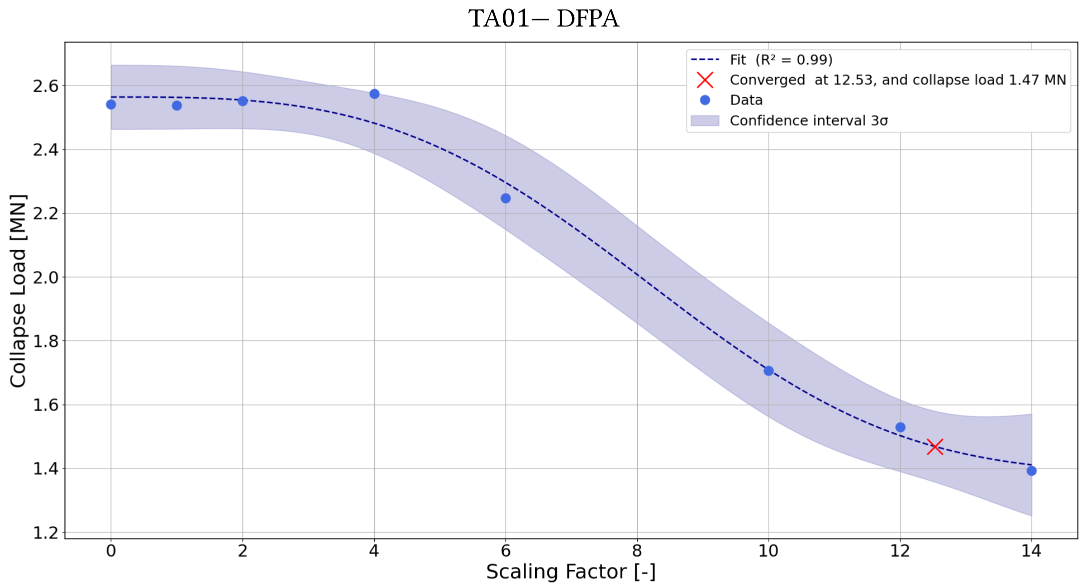

(a) 0 bar

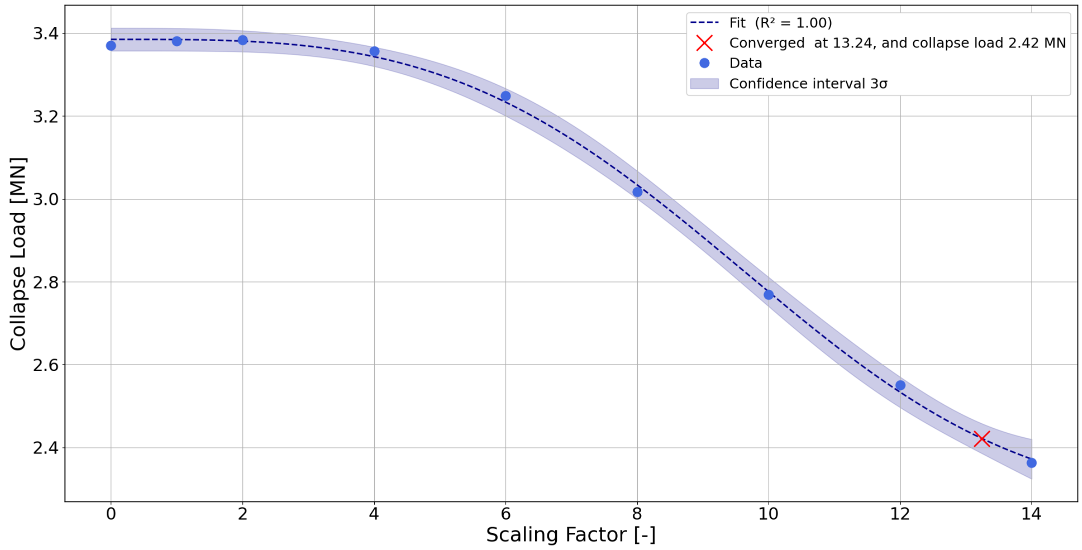

(b) 2 bar

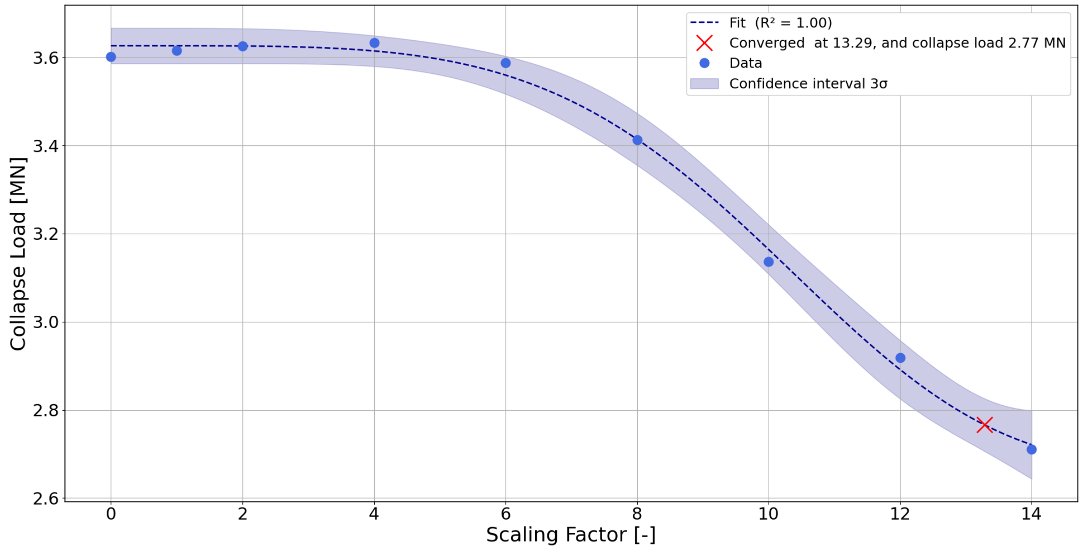

(c) 4 bar

Figure C.11: Convergence behavior of TA01 for DFPA.

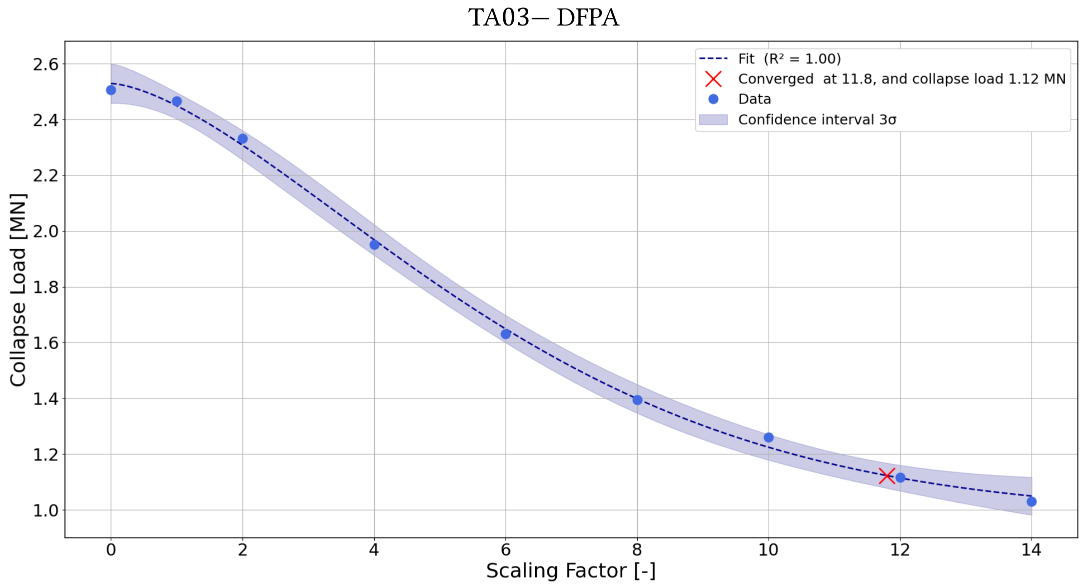

(a) 0 bar

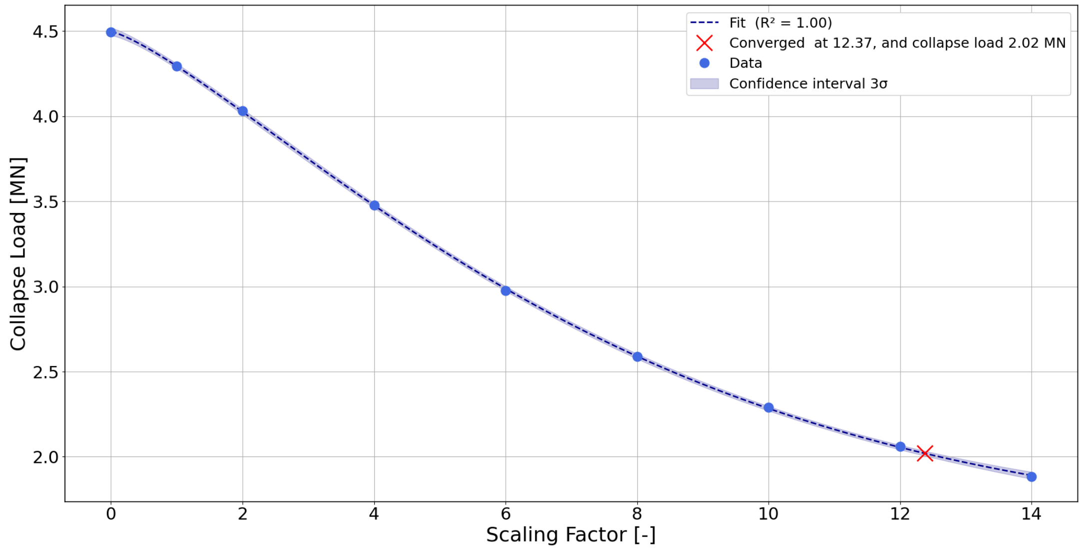

(b) 2 bar

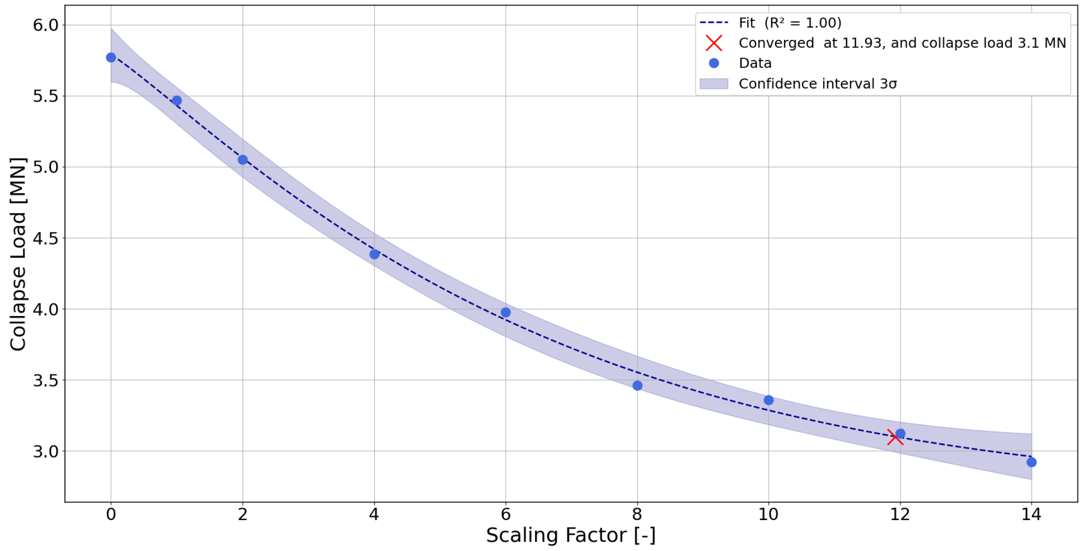

(c) 4 bar

Figure C.12: Convergence behavior of TA03 for DFPA.

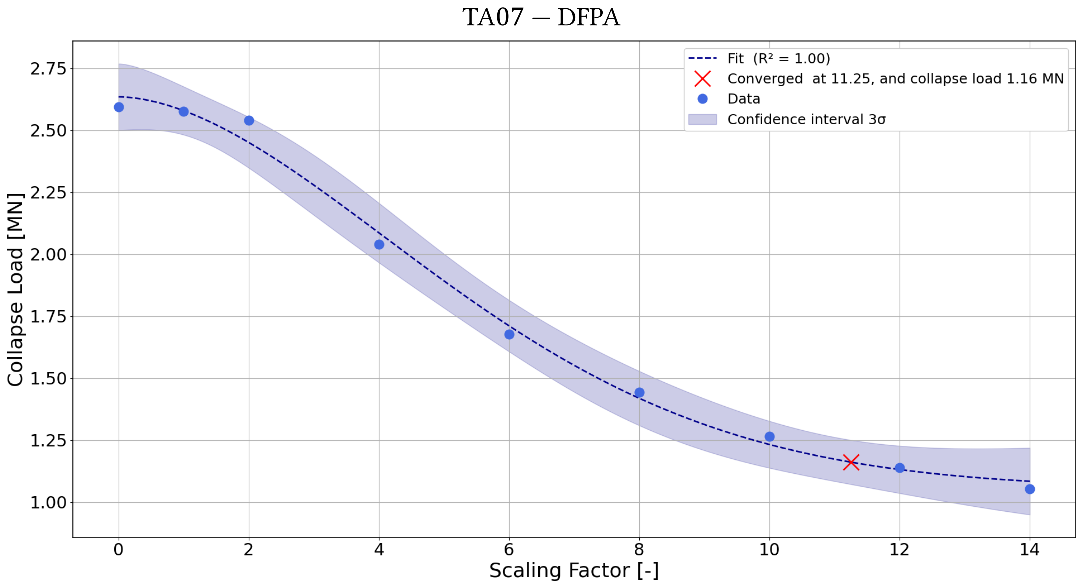

(a) 0 bar

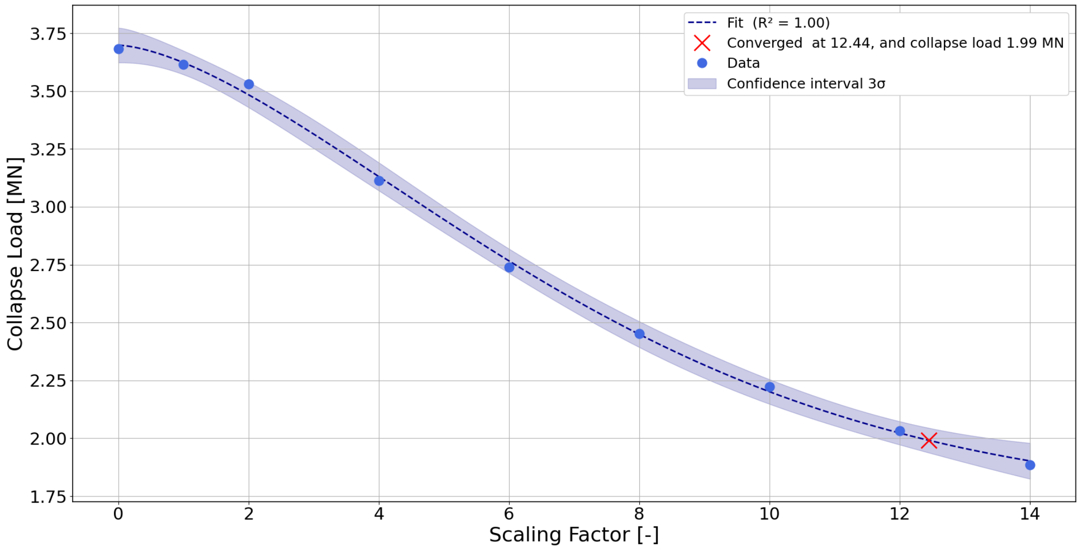

(b) 2 bar

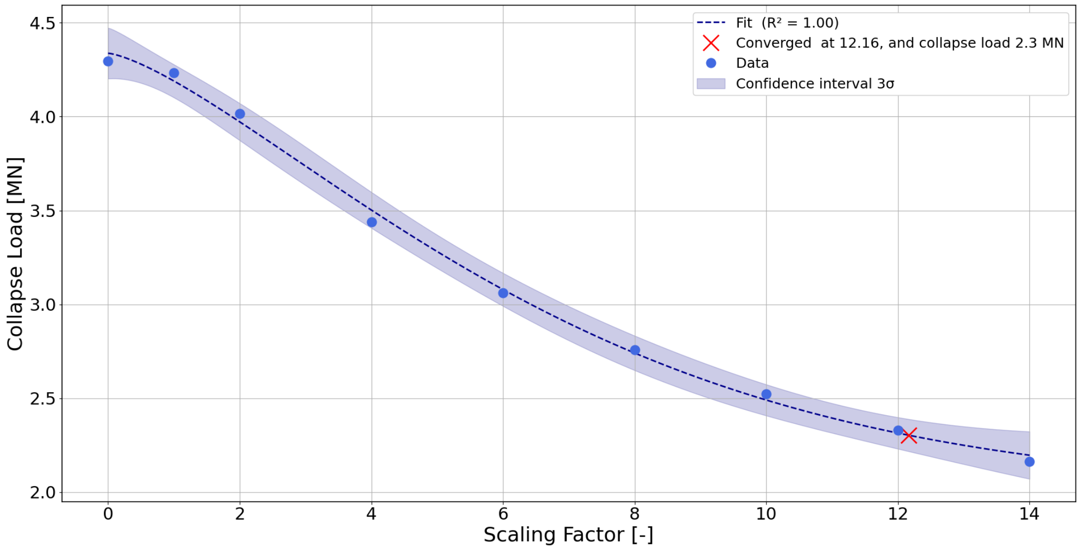

(c) 4 bar

Figure C.13: Convergence behavior of TA07 for DFPA.

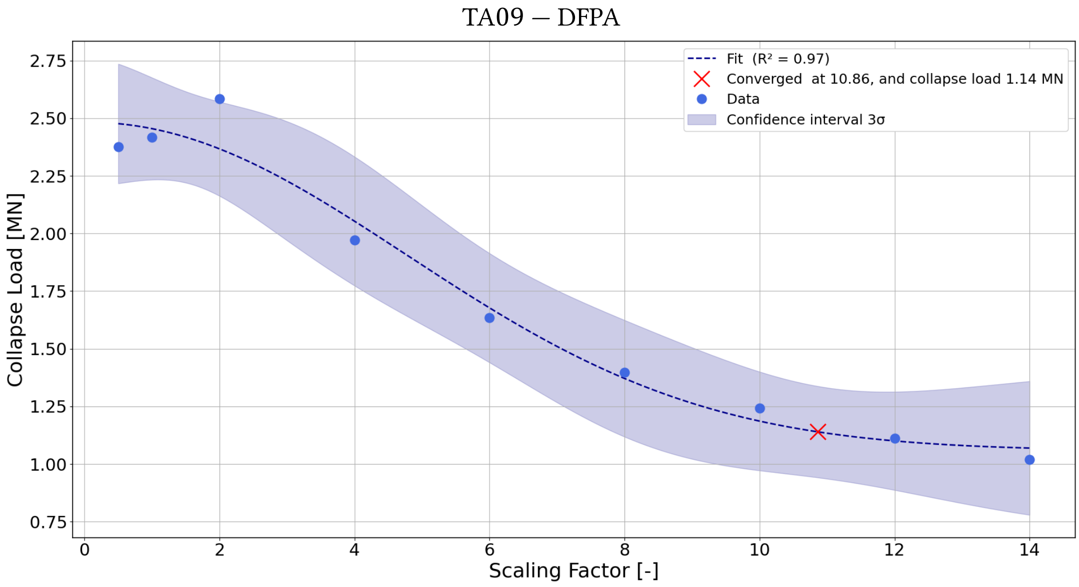

(a) 0 bar

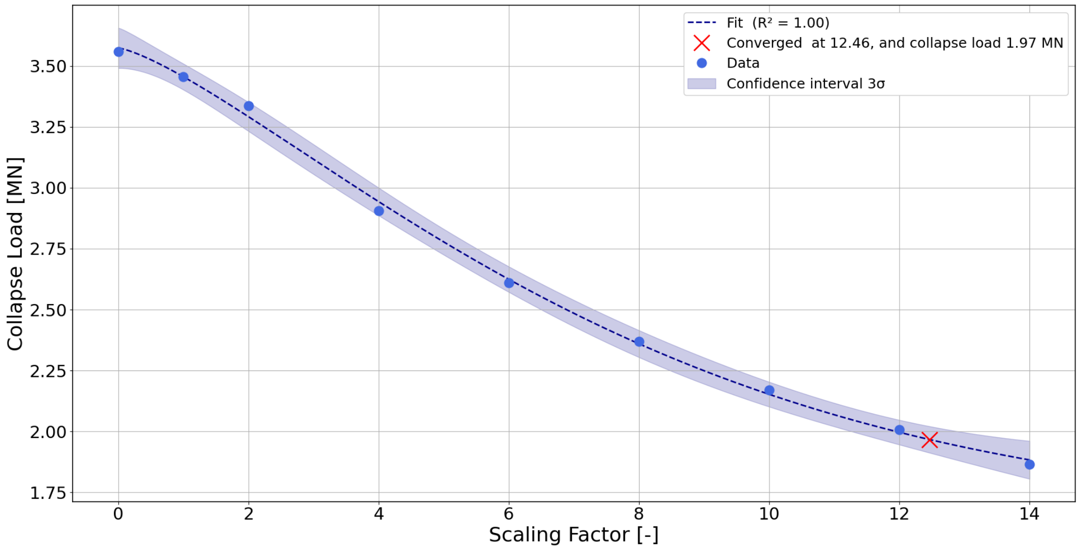

(b) 2 bar

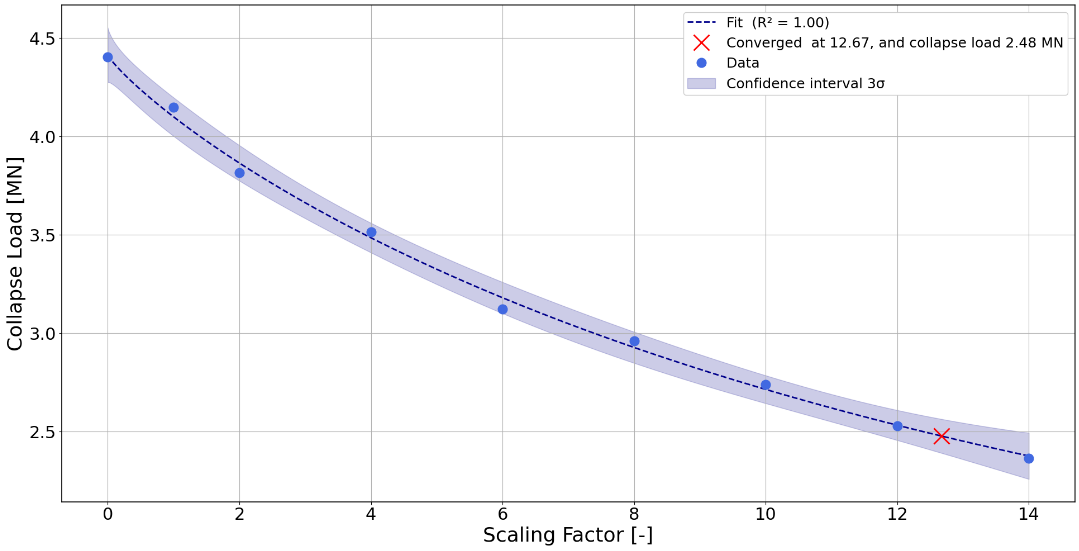

(c) 4 bar

Figure C.14: Convergence behavior of TA09 for DFPA.

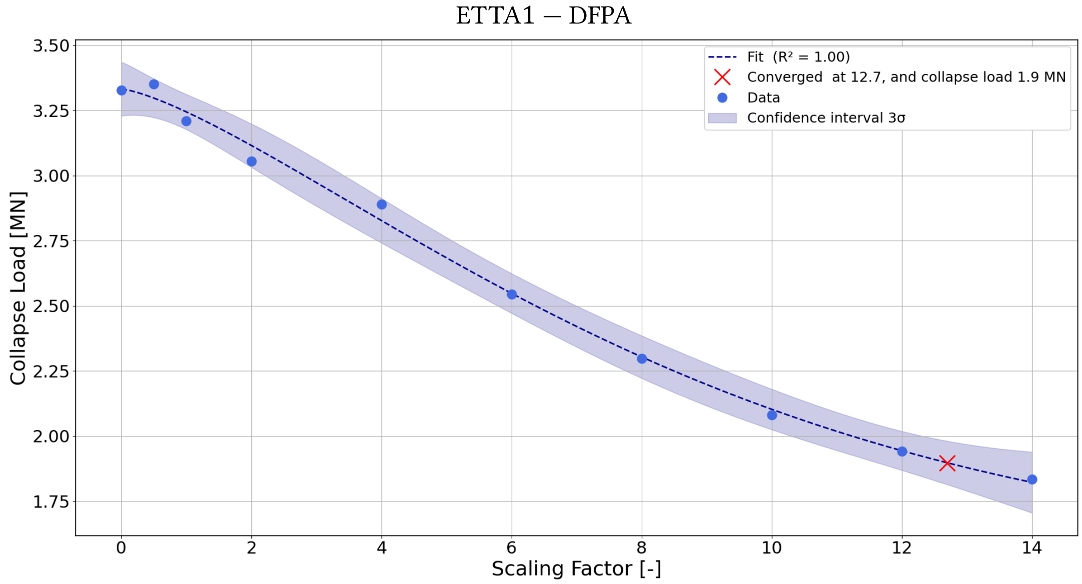

(a) 0 bar

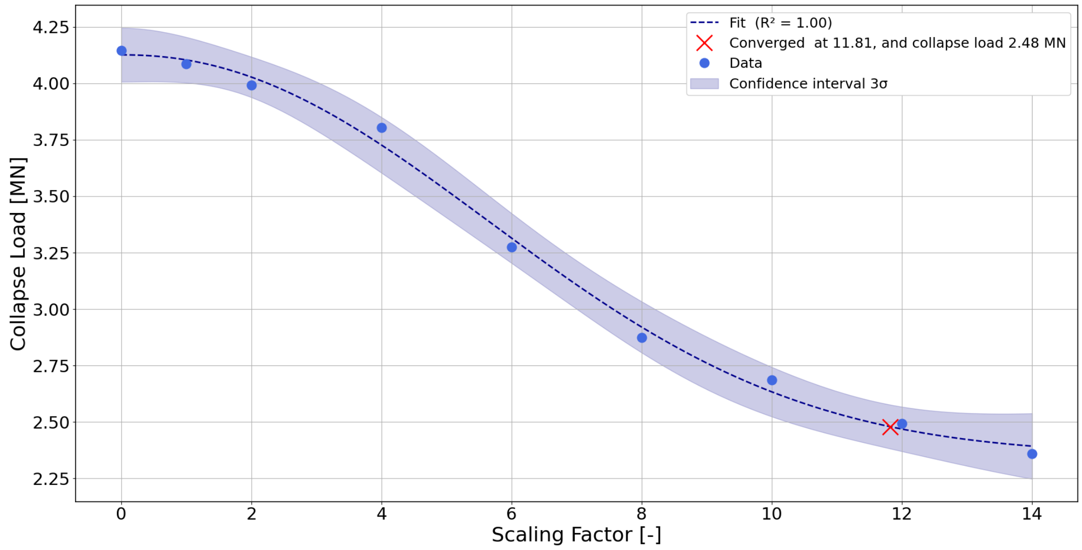

(b) 0.06895 bar

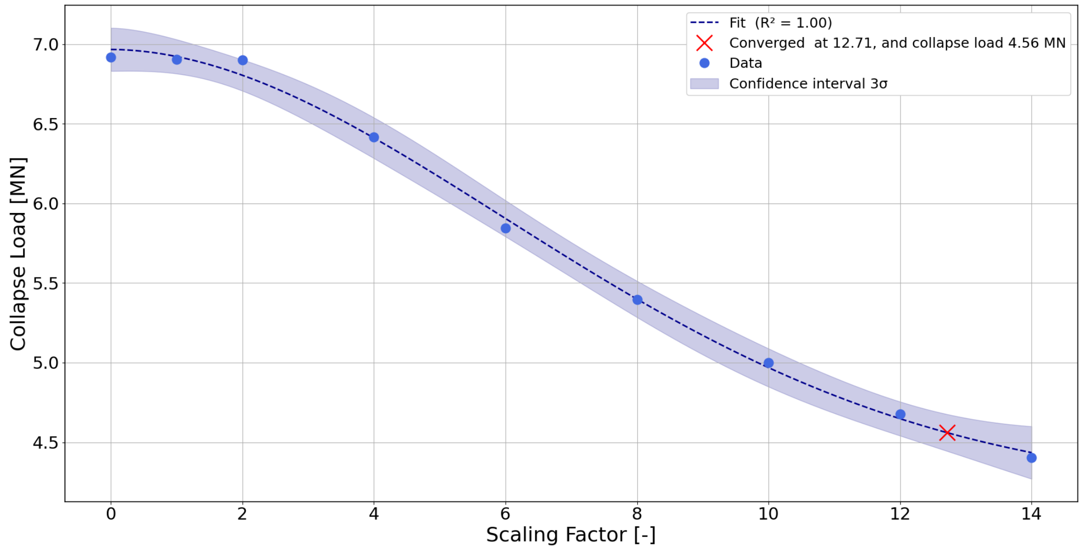

(c) 2 bar

Figure C.15: Convergence behavior of ETTA1 for DFPA.

D

Shell Knockdown Factor Calculations

In this work, two different knockdown-factor formulations were employed. The first is the original knockdown approach from the revised NASA SP-8007 buckling monograph [87]. In this formulation, the knockdown factor consists of two components: a baseline term for the unpressurized case, computed using Equation D.1, and an additional pressure-dependent increment, obtained from Figure D.1.

For the baseline knockdown factor, the parameter ϕ is evaluated for an orthotropic cylinder using Equation D.2. The corresponding bending and membrane stiffness calculations are detailed in Appendix B.

$$\gamma = 1 - 0.901\left(1 - e^{-\phi}\right) \tag{D.1}$$

$$\phi = \frac{1}{29.8}\left[\frac{r}{\sqrt[4]{\frac{D_{11}D_{22}}{E_{11}E_{22}}}}\right]^{\frac{1}{2}} \tag{D.2}$$

The SP-8007 monograph does not provide pressurization-dependent knockdown data for orthotropic cylinders. Consequently, the isotropic-cylinder pressure correction curve shown in Figure D.1 was adopted. To account for the presence of internal stiffeners in the definition of the pressure parameter $\frac{pr^2}{Et^2}$, the skin thickness t was replaced by the effective skin thickness t_{eff}.

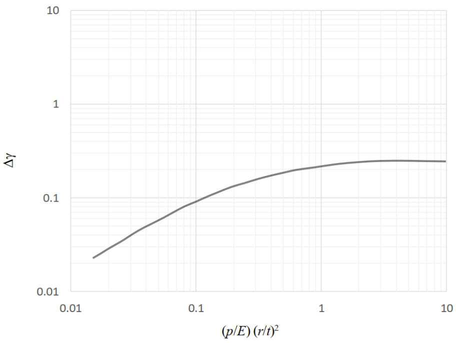

Figure D.1: Pressure-dependent knockdown increment $\Delta\gamma$ from SP-8007 [87].

The final knockdown factor is obtained by summation of the baseline and pressure-dependent components, as shown in Equation D.3. The buckling load is then calculated by multiplying the resulting knockdown factor by the linear eigenvalue buckling load for the unpressurized case, and by the geometrically nonlinear bifurcation load for pressurized cases, since LBA with internal pressure yields negative eigenvalues.

$$KDF_{\text{SP-8007}} = \gamma + \Delta\gamma \tag{D.3}$$

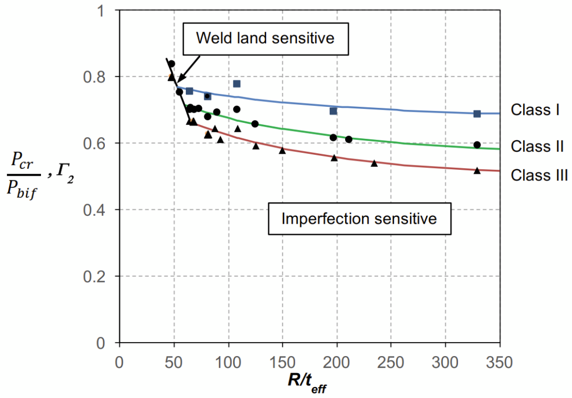

Figure D.2: Γ_2 values for different manufacturing classes [37].

The second approach is based on the SBKF project methodology, which is more elaborate, as both the baseline knockdown and the pressure increment are curve-dependent. In this study, Manufacturing Class 1 was selected, as the investigated shells are considered representative of state-of-the-art structures. The detailed-design formulation, based on the linear bifurcation buckling load, was adopted (Equation D.4).

$$P_{\text{detailed design}} = \Gamma_2 P_{\text{bif}} \tag{D.4}$$

The knockdown factor Γ_2 was obtained from the curves presented in [37], but was conveniently approximated using the analytical fit proposed by [94], given in Equation D.5.

$$\Gamma_{2_{\text{Class 1}}} = 0.867 - 0.0159\sqrt{\frac{R}{t_{\text{eff}}}} + 0.000340\frac{R}{t_{\text{eff}}} \tag{D.5}$$

For pressurized buckling, a pressure-dependent modifier $\Delta\Gamma$ is added to the knockdown factor, analogous to the $\Delta\gamma$ correction in SP-8007. This increment is estimated directly from Figure D.3, which provides data only up to 1 psi. The resulting pressurized buckling load is computed using Equation D.6, with the GNA load obtained in this study.

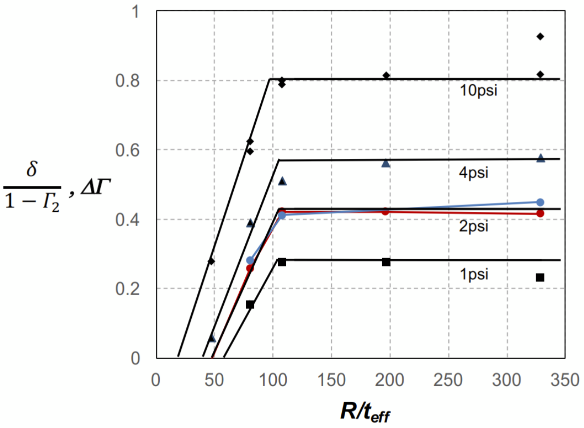

Figure D.3: $\Delta\Gamma$ values for different pressure levels [37].

$$P^{\text{press}}_{\text{detailed design}} = (\Gamma_2 + \Delta\Gamma)(1 - \Gamma_2)P^{\text{press}}_{\text{GNA}} \tag{D.6}$$

E

Buckling Loads

Table E.1: Buckling loads for TA01 across pressure levels.

	N_{GNA} [N]	N_{MGI} [N]	N_{SPLAOG} [N]	$N_{\mathrm{SPLA},P=2338}$ [N]	N_{MPLAOG} [N]	$N_{\mathrm{MPLA},P=3173}$ [N]	N_{DFPAOG} [N]	$N_{\mathrm{DFPA},P=12.53}$ [N]	N_{EIA} [N]
0 bar	2.999×10^{6}	2.531×10^{6}	2.020×10^{6}	2.020×10^{6}	1.521×10^{6}	1.521×10^{6}	1.470×10^{6}	1.470×10^{6}	1.633×10^{6}
2 bar	3.580×10^{6}	3.581×10^{6}	3.292×10^{6}	3.299×10^{6}	2.979×10^{6}	2.829×10^{6}	2.498×10^{6}	2.422×10^{6}	2.997×10^{6}
4 bar	3.864×10^{6}	3.891×10^{6}	3.728×10^{6}	3.669×10^{6}	3.496×10^{6}	3.343×10^{6}	2.858×10^{6}	2.766×10^{6}	3.693×10^{6}

Table E.2: Buckling loads for TA03 across pressure levels.

	N_{GNA} [N]	N_{MGI} [N]	N_{SPLAOG} [N]	$N_{\mathrm{SPLA},P=6065}$ [N]	N_{MPLAOG} [N]	$N_{\mathrm{MPLA},P=6415}$ [N]	N_{DFPAOG} [N]	$N_{\mathrm{DFPA},P=11.8}$ [N]	N_{EIA} [N]
0 bar	2.921×10^{6}	2.622×10^{6}	2.716×10^{6}	2.716×10^{6}	2.356×10^{6}	2.356×10^{6}	1.123×10^{6}	1.123×10^{6}	2.612×10^{6}
2 bar	4.605×10^{6}	4.654×10^{6}	4.607×10^{6}	4.612×10^{6}	4.488×10^{6}	4.481×10^{6}	2.057×10^{6}	2.020×10^{6}	4.633×10^{6}
4 bar	5.870×10^{6}	5.851×10^{6}	5.746×10^{6}	5.765×10^{6}	5.577×10^{6}	5.575×10^{6}	3.104×10^{6}	3.101×10^{6}	5.844×10^{6}

Table E.3: Buckling loads for TA07 across pressure levels.

	N_{GNA} [N]	N_{MGI} [N]	N_{SPLAOG} [N]	$N_{\mathrm{SPLA},P=2854}$ [N]	N_{MPLAOG} [N]	$N_{\mathrm{MPLA},P=3887}$ [N]	N_{DFPAOG} [N]	$N_{\mathrm{DFPA},P=11.25}$ [N]	N_{EIA} [N]
0 bar	2.832×10^{6}	2.320×10^{6}	2.113×10^{6}	2.113×10^{6}	1.594×10^{6}	1.594×10^{6}	1.161×10^{6}	1.161×10^{6}	1.847×10^{6}
2 bar	3.731×10^{6}	3.460×10^{6}	3.602×10^{6}	3.514×10^{6}	3.299×10^{6}	3.274×10^{6}	2.082×10^{6}	1.991×10^{6}	3.365×10^{6}
4 bar	4.394×10^{6}	4.184×10^{6}	4.227×10^{6}	4.229×10^{6}	3.960×10^{6}	3.939×10^{6}	2.369×10^{6}	2.303×10^{6}	4.098×10^{6}

Table E.4: Buckling loads for TA09 across pressure levels.

	N_{GNA} [N]	N_{MGI} [N]	N_{SPLAOG} [N]	$N_{\mathrm{SPLA},P=2854}$ [N]	N_{MPLAOG} [N]	$N_{\mathrm{MPLA},P=4545}$ [N]	N_{DFPAOG} [N]	$N_{\mathrm{DFPA},P=10.78}$ [N]	N_{EIA} [N]
0 bar	2.463×10^{6}	1.986×10^{6}	2.095×10^{6}	2.095	1.617×10^{6}	1.617×10^{6}	1.142×10^{6}	1.142×10^{6}	1.995×10^{6}
2 bar	3.931×10^{6}	3.717×10^{6}	3.630×10^{6}	3.710×10^{6}	3.569×10^{6}	3.525×10^{6}	2.073×10^{6}	1.967×10^{6}	3.647×10^{6}
4 bar	4.656×10^{6}	4.595×10^{6}	4.557×10^{6}	4.539×10^{6}	4.332×10^{6}	4.315×10^{6}	2.613×10^{6}	2.478×10^{6}	4.507×10^{6}

Table E.5: Buckling loads for ETTA1 across pressure levels.

	N_{GNA} [N]	N_{MGI} [N]	N_{SPLAOG} [N]	$N_{\mathrm{SPLA},P=4665}$ [N]	N_{MPLAOG} [N]	$N_{\mathrm{MPLA},P=4961}$ [N]	N_{DFPAOG} [N]	$N_{\mathrm{DFPA},P=12.7}$ [N]	N_{EIA} [N]
0 bar	3.427×10^{6}	2.114×10^{6}	3.105×10^{6}	3.105×10^{6}	1.458×10^{6}	1.458×10^{6}	1.898×10^{6}	1.898×10^{6}	3.513×10^{6}
1 psi	3.807×10^{6}	3.008×10^{6}	3.718×10^{6}	3.693×10^{6}	2.648×10^{6}	2.653×10^{6}	2.387×10^{6}	2.480×10^{6}	3.868×10^{6}
2 bar	6.921×10^{6}	6.850×10^{6}	6.877×10^{6}	6.876×10^{6}	6.880×10^{6}	6.882×10^{6}	4.577×10^{6}	4.561×10^{6}	6.879×10^{6}